

ACCEPTED MANUSCRIPT

# Wide-Bandgap, Low-Bandgap, and Tandem Perovskite Solar Cells

To cite this article before publication: Zhaoning Song *et al* 2019 *Semicond. Sci. Technol.* in press <https://doi.org/10.1088/1361-6641/ab27f7>

## Manuscript version: Accepted Manuscript

Accepted Manuscript is “the version of the article accepted for publication including all changes made as a result of the peer review process, and which may also include the addition to the article by IOP Publishing of a header, an article ID, a cover sheet and/or an ‘Accepted Manuscript’ watermark, but excluding any other editing, typesetting or other changes made by IOP Publishing and/or its licensors”

This Accepted Manuscript is © 2019 IOP Publishing Ltd.

During the embargo period (the 12 month period from the publication of the Version of Record of this article), the Accepted Manuscript is fully protected by copyright and cannot be reused or reposted elsewhere.

As the Version of Record of this article is going to be / has been published on a subscription basis, this Accepted Manuscript is available for reuse under a CC BY-NC-ND 3.0 licence after the 12 month embargo period.

After the embargo period, everyone is permitted to use copy and redistribute this article for non-commercial purposes only, provided that they adhere to all the terms of the licence <https://creativecommons.org/licenses/by-nc-nd/3.0>

Although reasonable endeavours have been taken to obtain all necessary permissions from third parties to include their copyrighted content within this article, their full citation and copyright line may not be present in this Accepted Manuscript version. Before using any content from this article, please refer to the Version of Record on IOPscience once published for full citation and copyright details, as permissions will likely be required. All third party content is fully copyright protected, unless specifically stated otherwise in the figure caption in the Version of Record.

View the [article online](#) for updates and enhancements.

# Wide-Bandgap, Low-Bandgap, and Tandem Perovskite Solar Cells

Zhaoning Song<sup>1</sup>, Cong Chen<sup>1,2</sup>, Chongwen Li<sup>1</sup>, Rasha A. Awni<sup>1,3</sup>, Dewei Zhao<sup>1,4</sup> and Yanfa Yan<sup>1</sup>

<sup>1</sup> Department of Physics and Astronomy, Wright Center for Photovoltaics Innovation and Commercialization, The University of Toledo, Toledo, OH 43606, U.S.A.

<sup>2</sup> Key Lab of Artificial Micro- and Nano-Structures of Ministry of Education, School of Physics and Technology, Wuhan University, Wuhan 430072, China

<sup>3</sup> Department of Physics, College of Education for Pure Sciences, University of Tikrit, Tikrit 34001, Iraq.

<sup>4</sup> Ordered Matter Science Research Center and College of Chemistry, Nanchang University, Nanchang 330031, China

E-mail: [zhaoning.song@utoledo.edu](mailto:zhaoning.song@utoledo.edu) and [yanfa.yan@utoledo.edu](mailto:yanfa.yan@utoledo.edu)

## Abstract

Organic-inorganic metal halide perovskite single-junction solar cells have attracted great attention in the past few years due to a high record power conversion efficiency (PCE) of 23.7% and low-cost fabrication processes. Beyond single-junction devices, low-temperature solution processability, and bandgap tunability make the metal halide perovskites ideal candidates for fabricating tandem solar cells. Tandem solar cells combining a wide-bandgap perovskite top cell and a low-bandgap bottom cell based on mixed tin (Sn)-lead (Pb) perovskite or a dissimilar material such as silicon (Si) or copper indium gallium selenide (CIGS) offer an extraordinary opportunity to achieve PCEs higher than Shockley-Queisser (SQ) radiative efficiency limits (~33%) for single-junction cells. In this review, we will summarize recent research progress on the fabrication of wide- (1.7 to 1.9 eV) and low-bandgap (1.1 to 1.3 eV) perovskite single-junction cells and their applications in tandem cells. Key challenges and issues in wide- and low-bandgap single-junction cells will be discussed. We will survey current state-of-the-art perovskite tandem cells and discuss the limitations and challenges for perovskite tandem cells. Lastly, we conclude with an outlook for the future development of perovskite tandem solar cells.

Keywords: perovskite solar cells, wide bandgap, low bandgap, tandem solar cells

## 1. Introduction

Metal halide perovskite solar cells (PSCs) have become a hot photovoltaic (PV) research area in recent years because they hold the promise to achieve high power conversion efficiencies (PCEs) and low manufacturing costs [1-6]. The combination of the high performance of PSCs that enabled by the excellent optoelectronic properties of the materials, ease of material and device processing, and low fabrication costs has attracted continually increasing research efforts to study PSCs, accelerating the learning curve of this emerging PV technology. As a result of intense research efforts all over the world, the certified record PCE of single-junction PSCs has soared in the past five years, climbing from less than 14% in 2013 to 23.7% in 2018 [7]. Despite the constant improvement in the performance of PSCs, the PCE of single-junction solar cells is curtailed by the Shockley-Queisser (SQ) radiative efficiency limits of 31-33% [8]. Research effort is now being directed toward developing tandem solar cells, which promise PCEs of more than 42% under AM1.5 solar irradiance [9].

So far, high performance monolithically integrated multijunction solar cells have been only demonstrated using single crystalline III-V materials (e.g., SpectroLab's 38.8% 5-junction GaAs-InP tandem [10, 11] and 40.7% GaInP/GaAs/Ge concentrator cell [12] and LG electronics' 32.8% GaInP/GaAs [13]). These multijunction devices, consisting of subcells with tunable bandgaps connected in series by p+/n+ tunnel junction (also called recombination contact), demonstrate a boost in performance relative to their single-junction counterparts. However, the complex epitaxial growth process and the use of expensive single-crystal substrates have prevented III-V tandem solar cells from being low-cost and thus limited the III-V tandem cells for space applications. As an low-cost alternative, tandem solar cells have also been demonstrated using amorphous (a), microcrystalline ( $\mu$ c), and nanocrystalline (nc) Group IV thin films (e.g., Unisolar's a-Si:H/a-SiGe:H/ $\mu$ c-Si:H device [14] and AIST's a-Si/nc-Si/nc-Si device [15]). However, the PCEs of ~14% of Group IV tandem cells are still much inferior to other single-junction thin film PV technologies (>22%). Additionally, polycrystalline thin film tandem solar cells are predicted to outperform single-junction cells in the energy yield [16], it was unclear what material combination could fulfill the promise of high efficiency and low cost tandem solar cells.

The progress of PSCs provides a unique opportunity to achieve high efficiency and low-cost thin film tandem solar cells. The combination of excellent PV properties of perovskite materials, tunable bandgap in a wide range, and low-temperature deposition techniques makes perovskite materials especially attractive for multijunction tandem solar cells. The advent of PSCs makes it possible to fabricate tandem solar cells consisting of wide-bandgap (wide- $E_g$ )

perovskite top cells and low-bandgap (low- $E_g$ ) bottom cells, including another perovskite (i.e., mixed Sn-Pb perovskites) or a dissimilar material, such as crystalline silicon (c-Si) or copper indium gallium selenide (CIGS), to realize the goal of ultrahigh efficiency and low-cost tandem cells. As a result, substantial efforts are now directed at fabrication of high-efficiency low-cost tandem PSCs.

Many previous progress review articles have summarized the perovskite material properties and early developments of single-junction and tandem PSCs [3, 4, 17-24]. In this topical review article, we aim to provide an overview of recent research advances on single-junction wide- $E_g$  (Section 2) and low- $E_g$  PSCs (Section 3) as well as their applications in tandem solar cells (Section 4). For each section, notable devices and technical evolution paths toward record efficiencies are highlighted and followed by discussions on major challenges and issues that limit the PSCs. Possible strategies to mitigate these current limitations are also discussed. Finally, a brief outlook of future development of single-junction and tandem PSCs is provided (Section 5).

Here, we start with a brief introduction of metal halide perovskite materials and the terminology used for describing PSC architectures. Metal halides with the perovskite crystal structure (**figure 1(a)**) are generally denoted by a formula of  $AMX_3$ , where A is a monovalent cation, such as methylammonium (MA), formamidinium (FA), cesium (Cs), and rubidium (Rb), M is a divalent metal cation, including lead (Pb), tin (Sn), and germanium (Ge), and X is a halide anion, such as iodine (I), bromine (Br), and chlorine (Cl) [25]. The application of PSCs was initiated with the benchmarked methylammonium lead iodide ( $MAPbI_3$ ) with a bandgap of 1.55 eV [26-28], and rapidly expanded to other perovskite compositions by substituting cations and anions. Different perovskite compositions are typically intermixable if the atomic size differences are permitted by the tolerance factor to form the perovskite crystal structure [29]. The homogeneous alloying of mixed cations and/or mixed anions perovskite films allows the bandgap of perovskite materials to be continuously tuned in a wide spectral range from infrared (1.15 eV) to ultraviolet (up to ~ 3 eV), as shown in **figure 1(b)** [30]. For instance, varying the halide ratios in the  $AM(Br_{1-x}Cl_x)_3$  and  $AM(I_{1-x}Br_x)_3$  allows bandgap tailoring from 2.3 to ~3 eV (**figure 1(c)**) [31, 32] and from ~1.4 to 2.3 eV (**figure 1(d)**) [33, 34], respectively. Additionally, mixing Sn perovskites with Pb perovskites to form mixed Sn-Pb perovskite alloys of  $A(Sn_xPb_{1-x})I_3$  can tune the perovskite bandgap to ~1.2 eV [35, 36], which is lower than that of pure Sn or Pb perovskites (**figure 1(e)**).

Single-junction PSCs are commonly fabricated in two major architectures, the regular (n-i-p) structure and so-called inverted (p-i-n) structure, as shown in **figure 2**. For the n-i-p structure (**figure 2(a)**), the fabrication (and the

light incident) sequence is glass substrate, transparent conductive oxide (TCO) front electrode, n-type electron selective layer (ESL), perovskite absorber layer, p-type hole selective layer (HSL), and back electrode (opaque or transparent). For the p-i-n structure, the positions of ESL and HSL are reversed (**figure 2(b)**). Based on the bandgap of the perovskite absorber layer, single-junction PSCs are categorized as wide- $E_g$  ( $> 1.7$  eV), medium- $E_g$  (1.5 to 1.65 eV), and low- $E_g$  ( $< 1.4$  eV) PSCs. Wide- and medium- $E_g$  PSCs with a transparent back electrode are typically used for the top subcell of all types of tandem PSCs. Low- $E_g$  PSCs are particularly used for the bottom subcell of all-perovskite tandem solar cells. Device structures for tandem solar cells will be discussed in Section 4.

## 2. Wide-bandgap perovskite solar cells

Wide- $E_g$  PSCs with bandgaps between 1.7 and 1.9 eV are ideal for tandem applications with Si, CIGS, and low- $E_g$  PSCs. This bandgap range is typically realized by partially substituting Br for I in iodide-based perovskites, with higher Br content resulting in a wider bandgap. A small proportion ( $\sim 15\%$ ) of Br incorporation is found to be beneficial for achieving high-quality perovskite films that are used to fabricate the state-of-the-art PSCs [37, 38]. However, for perovskites with a bandgap exceeding 1.7 eV, achieving a high open-circuit voltage ( $V_{OC}$ ) that is close to the theoretical limit is a great challenge. Unlike their lower bandgap ( $E_g < 1.6$  eV) perovskite counterparts, wide- $E_g$  ( $> 1.7$  eV) perovskite solar cells typically exhibit high  $V_{OC}$ -deficits, defined as  $E_g/e - V_{OC}$ , where  $e$  is the unit charge. Such high  $V_{OC}$ -deficits are attributed to photoinduced phase segregation, defects in the bulk and at grain boundaries of perovskite films, and energy level mismatch between wide- $E_g$  perovskite and the ESL/HSL. A summary of wide- $E_g$  PSCs reported in the past three years is provided in Table 1. Details will be discussed later in this section.

### 2.1 Recent research advances in wide-bandgap perovskite cells

The research on wide- $E_g$  perovskite solar cells was initiated in 2013 by Noh et al. and Eperon et al. who investigated the bandgap tunability of  $\text{MAPb}(\text{I}_{1-x}\text{Br}_x)_3$  [39] and  $\text{FAPb}(\text{I}_{1-x}\text{Br}_x)_3$  [40], respectively. While the proven bandgap tunability from 1.5 to 2.3 eV is very attractive for tandem cell applications, the progress on wide- $E_g$  PSCs has lagged far behind the medium- $E_g$  ( $\sim 1.6$  eV) PSCs due to the intrinsic photo-instability of the materials [34]. Many efforts have been devoted to overcoming the instability of the mixed I-Br perovskites, but significant progress was not made until later 2015 to 2016. The breakthrough was made by Snaith and coworkers who demonstrated a series of efficient wide- $E_g$  PSCs with FA/Cs based perovskites, which are more phase stable than the MA-based perovskites under the

photo and thermal stresses [41]. **Figure 3(a)** compares a series of  $\text{FAPb}(\text{I}_{1-x}\text{Br}_x)_3$  and  $\text{FA}_{0.83}\text{Cs}_{0.17}\text{Pb}(\text{I}_{1-x}\text{Br}_x)_3$  films with various Br concentrations. It is clear that  $\text{FAPb}(\text{I}_{1-x}\text{Br}_x)_3$  films exhibit the “yellow phase” for  $x$  ranging from 0.3 to 0.6 due to phase transition from the perovskite phase to a hexagonal non-perovskite phase [42]. In contrast,  $\text{FA}_{0.83}\text{Cs}_{0.17}\text{Pb}(\text{I}_{1-x}\text{Br}_x)_3$  films show a continuous change of color as Br content is increased. More importantly, FA/Cs mixed-cation perovskites exhibited better structural stability than MA-based perovskites after longtime light exposure, as evidenced by the PL spectra in **figure 3(b)**. The champion device with 1.74-eV  $\text{Cs}_{0.17}\text{FA}_{0.83}\text{Pb}(\text{I}_{0.6}\text{Br}_{0.4})_3$  in the n-i-p structure (**figure 3(c)**) delivered a PCE of 17.1%, with a  $V_{\text{OC}}$  of 1.2 V, a short-circuit current density ( $J_{\text{SC}}$ ) of 19.4  $\text{mA cm}^{-2}$ , and a fill factor (FF) of 75.1%. Since this work, the  $\text{Cs}_y\text{FA}_{1-y}\text{Pb}(\text{I}_{1-x}\text{Br}_x)_3$  compositions have become one of the most popular choices for the wide- $E_g$  PSCs.

Another significant contribution was made by Huang group who synthesized  $\text{MAPbBr}_x\text{I}_{3-x}$  films with a bandgap of 1.7 to 1.75 eV via a low-temperature sequential deposition method [43, 44]. For this method, a  $\text{PbI}_2$  film was first spin-coated onto an ITO/HSL substrate and followed by spin-coating of MAI/MABr in an isopropanol solution and solvent annealing (**figure 3(d)**). PCEs up to 13.1% and 16.6% were demonstrated for p-i-n wide- $E_g$  PSCs (**figure 3(e)**) employing poly(3,4-ethylenedioxythiophene) polystyrene sulfonate (PEDOT:PSS) and poly[bis(4-phenyl)(2,4,6-trimethylphenyl)amine] (PTAA) as the HSL, respectively [43, 44]. It is worth noting the non-wettability of PTAA to the perovskite precursor solution promotes high-aspect-ratio crystalline grain growth, leading to a flat surface with large grain sizes (**figure 3(f)**), which is beneficial for reducing recombination and improving  $V_{\text{OC}}$  [45]. As a result, PSCs with the 1.75-eV  $\text{MAPb}(\text{Br}_{0.27}\text{I}_{0.73})_3$  perovskite absorber layers and PTAA HSLs yielded a PCE of 14.9% with a high  $V_{\text{OC}}$  of 1.21 V.

After that, many processing strategies, including the incorporation of additives and post-deposition annealing, which aim to improve the electronic quality of wide- $E_g$  perovskite films have been used to improve the device performance. Duong et al. incorporated RbI to  $\text{FA}_{0.75}\text{MA}_{0.15}\text{Cs}_{0.1}\text{Pb}(\text{I}_{0.67}\text{Br}_{0.33})_3$  perovskite and achieved 1.73-eV n-i-p type PSCs with a PCE of 17.4% but an unsatisfactory  $V_{\text{OC}}$  of ~1.15 V [46]. Yu et al. used synergistic effects of lead thiocyanate additive ( $\text{Pb}(\text{SCN})_2$ ) and solvent annealing to enlarge grain size of  $\text{FA}_{0.8}\text{Cs}_{0.2}\text{Pb}(\text{I}_{0.7}\text{Br}_{0.3})_3$  perovskite films, which led to n-i-p type wide- $E_g$  PSCs with a stabilized efficiency of 17.18% and a high  $V_{\text{OC}}$  of 1.25 V (**figure 4(a)**) [47]. The effect of  $\text{Pb}(\text{SCN})_2$  additives was later confirmed by Zhou et al. who added a proper amount of  $\text{Pb}(\text{SCN})_2$  to  $\text{FA}_{0.8}\text{Cs}_{0.2}\text{Pb}(\text{I}_{0.73}\text{Br}_{0.27})_3$  to obtain a PCE of 18.6% with a high  $V_{\text{OC}}$  of 1.244 V [48].

Interface modification is an important strategy to enhance efficiency and stability of PSCs. Ionic defects at the surfaces and grain boundaries of perovskite films cause recombination of photoexcited charge carriers, limiting photovoltage of solar cells. The further PCE enhancement in wide- $E_g$  PSCs has been realized by surface modification and defect passivation. Zhou et al. used benzylamine (BA) to treat the surface of 1.72-eV wide- $E_g$   $\text{FA}_{0.15}\text{Cs}_{0.85}\text{Pb}(\text{I}_{0.73}\text{Br}_{0.27})_3$  perovskite films to passivate grain boundaries. The BA-modified devices with the n-i-p structure exhibited a PCE of 18.1% with a  $V_{OC}$  of 1.24 V but a significant J-V hysteresis under the forward scans (**figure 4(b)**) [49]. In 2017, Huang and coworkers demonstrated an approach to enhance the performance of wide- $E_g$  PSCs by adding a layer of quaternary ammonium halides on the surface of the perovskite absorber to passivate ionic defects on the surface and grain boundaries [50]. The defect passivation reduced the  $V_{OC}$ -deficit of 1.72-eV wide- $E_g$   $\text{FA}_{0.83}\text{MA}_{0.17}\text{Pb}(\text{I}_{0.6}\text{Br}_{0.4})_3$  cells with the p-i-n structure to 0.57 V and boosted PCEs to 17.2%. In the follow-up study, they fabricated 1.71-eV wide- $E_g$  PSCs with the  $(\text{FA}_{0.83}\text{MA}_{0.17})_{0.95}\text{Cs}_{0.05}\text{Pb}(\text{I}_{0.6}\text{Br}_{0.4})_3$  absorber, PTAA HSL and isolating isomer of indene-C60 bisadduct (ICBA-trans3) ESL [51]. ICBA-trans3 provides better energy level alignment with wide- $E_g$  perovskites than conventional ICBA and thus leads to a PCE enhancement from 14.6% to 18.5% (**figure 4(c)**). The best device has a  $V_{OC}$  of 1.21 V, corresponding to a  $V_{OC}$ -deficit of 0.5 V.

Sargent group reported that incorporating a formamide co-solvent induces the direct formation of black perovskite phase, realizing reduced density of defects through bypassing the formation of the intermediate phase [52]. Using this method, they demonstrated wide- $E_g$  PSCs with a PCE of 17.8% and a  $V_{OC}$  of 1.23 V. They also developed a strategy to heal the deep traps in wide- $E_g$  perovskite by introducing dipolar cations (MA) in FA/Cs-based mixed-cation perovskites [53]. They achieved a PCE of 20.7% and a high  $V_{OC}$  of 1.22 V for 1.65-eV PSCs based on  $\text{Cs}_{0.05}\text{MA}_{0.15}\text{FA}_{0.8}\text{Pb}(\text{I}_{0.75}\text{Br}_{0.25})_3$  absorbers. For 1.74-eV  $\text{Cs}_{0.12}\text{MA}_{0.05}\text{FA}_{0.83}\text{Pb}(\text{I}_{0.6}\text{Br}_{0.4})_3$  absorbers, a PCE of 19.1% and a  $V_{OC}$  of 1.25 V was obtained (**figure 4(d)**), which is so far the highest PCE for wide- $E_g$  PSCs with the n-i-p structure reported in the literature. The  $V_{OC}$ -deficit of less than 0.5 V is among the best  $V_{OC}$ -deficits reported in the literature but still inferior to their lower bandgap counterparts.

## 2.2 Challenges and issues of wide-bandgap perovskite cells

**Figure 5** shows the  $V_{OC}$  and PCE values of notable wide- $E_g$  PSCs reported in the literature in the past three years. Despite the rapid progress as described above, the  $V_{OC}$ -deficits of wide- $E_g$  PSCs are still much higher than their lower bandgap ( $< 1.6$  eV) counterparts which typically have  $V_{OC}$ -deficits less than 0.4 V (**figure 5(a)**). For the optimal

bandgaps (1.7 to 1.9 eV) that are desired for tandem solar cells, there is a bottleneck to deliver a higher  $V_{OC}$  with increasing the perovskite bandgap. Consequently, PCE of wide- $E_g$  PSCs decreases with an increasing bandgap, as shown in **figure 5(b)**. Such high  $V_{OC}$ -deficits (~0.5 V) that are higher than the state-of-the-art medium- $E_g$  PSCs (< 0.3 eV) [54] are currently the most significant limitations for wide- $E_g$  (~1.7 to 1.9 eV) PSCs based on the mixed I-Br perovskites. The  $V_{OC}$  limitation presents a critical hurdle that needs to be overcome to fulfill the promise of ultrahigh efficiency tandem PSCs.

Mixed I-Br perovskites usually suffer from intrinsic photoinduced phase segregation, i.e., mixed I-Br perovskites segregate into I-rich and Br-rich domains under illumination and electrical bias [55-58]. Hoke et al. first reported the photo-induced trap state formation in  $MAPb(I_{1-x}Br_x)_3$  perovskites [34]. They observed that the initial photoluminescent peaks from the mixed I-Br perovskites disappeared after a short time of light exposure, which was accompanied by appearance of red-shifted peaks. Although this phase segregation effect is reversible upon storage in the dark, it is detrimental to the  $V_{OC}$  of wide- $E_g$  PSCs because photoexcited charge carriers will be trapped in the I-rich domains, limiting the Fermi energy splitting, and consequently the photovoltage in the mixed I-Br perovskites. Additionally, phase segregation and halide migration under electrical bias have been proposed as an origin of the degraded device performance. The mechanisms of photoinduced halide segregation are currently an ongoing research topic [59-64].

Remedies to mitigate the phase segregation in mixed I-Br wide- $E_g$  perovskite films are urgently needed. Many attempts have been made to find viable routes to suppress or inhibit halide phase segregation, including compositional engineering (e.g., via incorporating  $Cs^+$  [65] and  $Sn^{2+}$  [66]), incorporating potassium ( $K^+$ ) to passivate grain boundaries [67], post-deposition surface treatment [68], improving crystallinity and grain sizes of perovskite films [44], synthesis through size-tuned nanocrystals [69], and formation of 2D/3D perovskites alloying [70-72]. Particularly for the perovskite alloying with low dimensional perovskites, Stoddard et al. demonstrated enhanced phase stability of 1.84-eV wide- $E_g$  perovskite films via guanidinium (GA) alloying [70]. Xiao et al. used n-butylammonium iodide (BAI) incorporation to form a self-assembled capping layer to prevent halide redistribution [71]. Rajagopal et al. incorporated small amounts of phenylethylammonium (PEA) in  $MAPb(I_{0.6}Br_{0.4})$  perovskite to overcome the  $V_{OC}$  plateau issue in the wide- $E_g$  perovskite solar cells, achieving  $V_{OC}$  values of 1.30 to 1.35 V and PCEs up to 12.2% [72]. These examples show possible approaches to potentially retard or eliminate phase segregation in wide- $E_g$  mixed I-Br perovskite materials. Clearly, a much wider stoichiometric space needs to be systematically explored. Machine learning [73] and



automatic high-throughput robots [74] to synthesize and evaluate the stability of novel wide- $E_g$  perovskite compositions may help accelerate the discovery of more efficient and stable PSCs.

### 3. Low-bandgap perovskite solar cells

Partial substitution of Sn into Pb perovskites to form the mixed Sn-Pb perovskites can tune the bandgap to near infrared region ( $\sim 1.2$  to  $1.4$  eV), which can be used for ideal-bandgap single-junction PSCs or be paired with wide- $E_g$  PSCs to make all-perovskite tandem solar cells. The mixed Sn-Pb perovskites possess some unique optoelectronic properties such as the bandgap bowing effect (figure 1(e)) [36] and high conductivity, likely due to high background carrier concentrations [42]. Additionally, the low- $E_g$  perovskites suffer from the instability issue due to the ease of oxidation of  $\text{Sn}^{2+}$  to  $\text{Sn}^{4+}$ , resulting in much-shortened device durability and poor operational stability compared with their wider bandgap ( $> \sim 1.5$  eV) counterparts. Dedicated reviews on low- $E_g$  mixed Sn-Pb PSCs were recently published elsewhere [75, 76]. In this section, we will briefly review recent advances and discuss the remaining challenges and issues of low- $E_g$  PSCs.

#### 3.1 Recent research advances in low-bandgap perovskite cells

##### 3.1.1 Pure Sn-based perovskite solar cells.

The evolution of low- $E_g$  mixed Sn-Pb PSCs started with the research on lead-free pure Sn-based low- $E_g$  PSCs [77]. In 2014, Kanatzidis and Snaith groups independently fabricated lead-free  $\text{MASnI}_3$  solar cells, featuring a redshifted bandgap (below  $1.3$  eV) compared with the benchmark  $1.55$ -eV  $\text{MAPbI}_3$  [78, 79]. Further bandgap engineering by incorporating Br to adjust the chemical composition of  $\text{MASnI}_{1-x}\text{Br}_x$  enabled the n-i-p mesoporous PSCs with a PCE of  $5.73\%$ . It was later found that  $\text{FASnI}_3$  exhibited better performance and stability than  $\text{MASnI}_3$ . Seok group and our group demonstrated  $\text{FASnI}_3$  solar cells with PCEs of  $4.8\%$  and  $6.22\%$ , respectively, by adding  $\text{SnF}_2$  additive as a reducing agent to inhibit the oxidation of  $\text{Sn}^{2+}$  to  $\text{Sn}^{4+}$  [80, 81].

Research efforts then directed toward improving perovskite film crystallinity and morphology, passivating grain boundaries, and tuning perovskite composition to realize more stable and efficient pure-Sn perovskite films and devices. Ke et al. developed hollow-structured  $\text{MASnI}_3$  and  $\text{FASnI}_3$  using ethylenediammonium (EDA) additive, achieving PCEs of  $\sim 7\%$  for n-i-p PSCs (figure 6(a)) [82, 83]. Liu et al. optimized anti-solvent processing and achieved PCEs over  $9\%$  for p-i-n PSCs based on  $\text{FA}_{0.75}\text{MA}_{0.25}\text{SnI}_3$  (figure 6(b)) [84]. Shao et al. recently achieved a PCE of

9.0% for PSCs based on  $\text{FASnI}_3$  by incorporating layered (2D) PEA-Sn perovskite into  $\text{FASnI}_3$  (**figure 6(c)**) [85]. The low- $E_g$  perovskite films with PEA also demonstrated improved crystallinity and stability. Ning and coworkers developed a method to manipulate the growth of 2D-quasi-2D-3D hierarchical structure comprised of  $\text{PEA}_2\text{SnI}_4$  and  $\text{FASnI}_3$  [86] by adding  $\text{NH}_4\text{SCN}$  additive to the perovskite absorber, resulting in PSCs with a PCE up to 9.41% [87]. More importantly, the device exhibited decent stability, retaining 90% of its initial PCE after 600 hours of storage in  $\text{N}_2$  glovebox. Jokar et al. investigated the doping impacts of organic cations, such as EDA, BA, and GA on  $\text{FASnI}_3$  [88, 89]. They found that incorporating these large organic cations helped improve the performance and stability of pure Sn-based PSCs. PCEs of  $\sim 10\%$  (**figure 6(d)**) were obtained for the devices after storage in  $\text{N}_2$  glove box for more than 1000 hours, and the device showed robust stability under continuous illumination for one hour. Despite the attempts to continue to push up efficiencies of Pb-free PSCs, the performance of pure Sn-based PSCs is intrinsically limited by the high doping density and ease of oxidation. Consequently, pure Sn-based PSCs are not the optimal option for efficient and stable low- $E_g$  PSCs. Nonetheless, high-performance pure Sn-based PSCs still play a crucial role in developing high-efficiency low- $E_g$  PSCs.

### 3.1.2 Mixed Sn-Pb perovskite solar cells.

The lessons learned from the progress of pure Sn-based PSCs have benefited the development of mixed Sn-Pb PSCs. The research on mixed Sn-Pb PSCs started with MA-based perovskite compositions. In 2014, Hayase and coworkers demonstrated n-i-p mixed Sn-Pb PSCs based on  $\text{MASn}_{0.5}\text{Pb}_{0.5}\text{I}_3$  with a bandgap of  $\sim 1.17$  eV, lower than that of both  $\text{MASnI}_3$  ( $\sim 1.35$  eV) and  $\text{MAPbI}_3$  (1.55 eV) [90]. Although these low- $E_g$  PSCs exhibited mediocre PCEs of  $\sim 4\%$ , which were much inferior to typical PCEs obtained from  $\text{MAPbI}_3$  counterparts, the extended photoresponse to the longer wavelength range demonstrated the potential to utilize the mixed Sn-Pb perovskites to harvest more infrared photons. The PCEs of PSCs based on  $\text{MASn}_x\text{Pb}_{1-x}\text{I}_3$  were then rapidly raised to 7.4% [35] and over 10% [91] by Kanatzidis and Jen groups, respectively. In 2016, Li et al. used a two-step method to fabricate  $\text{MASn}_{0.5}\text{Pb}_{0.5}\text{I}_3$  PSCs, achieving a PCE of 13.6% [92]. Recently, Rajagopal et al. further improved the PCE of  $\text{MASn}_{0.5}\text{Pb}_{0.5}\text{I}_3$  PSCs to 15.6% via formation of a graded fullerene heterojunction [93]. Yang et al. utilized Br-incorporation to form  $\text{MAPb}_{0.5}\text{Sn}_{0.5}(\text{I}_{0.8}\text{Br}_{0.2})_3$  with an ideal bandgap of 1.35 eV for single-junction solar cells and demonstrated a PCE of 17.63% [94].

Benefited from the success in  $\text{FASnI}_3$  perovskites, efforts have been made to develop low- $E_g$  mixed Sn-Pb perovskites with mixed organic cations (MA/FA). In 2016, Yang et al. fabricated  $\text{MA}_{1-y}\text{FA}_y\text{Pb}_{0.75}\text{Sn}_{0.25}\text{I}_3$  solar cells, among which the 1.33-eV  $\text{MA}_{0.5}\text{FA}_{0.5}\text{Pb}_{0.75}\text{Sn}_{0.25}\text{I}_3$  PSCs deliver a PCE of 14.2% with decent stability after storage in  $\text{N}_2$  [95]. By combining  $\text{FASnI}_3$  and  $\text{MAPbI}_3$  precursor solutions (**figure 7(a)**), our group demonstrated a series of low- $E_g$  mixed Sn-Pb PSCs with a device structure of  $\text{ITO/PEDOT:SS}/(\text{FASnI}_3)_{1-x}(\text{MAPbI}_3)_x/\text{perovskite}/\text{C}_{60}/\text{BCP}/\text{Ag}$ , as shown in **figure 7(b)** [96]. The best-performing device based on  $(\text{FASnI}_3)_{0.6}(\text{MAPbI}_3)_{0.4}$  perovskite absorber with a bandgap of 1.25 eV delivered PCEs of up to 15%. We then further increased the mixed Sn-Pb absorber thickness to more than 600 nm by increasing the concentration of the precursor solution [97]. The thicker perovskite films exhibit large grain sizes and longer carrier lifetimes of up to  $\sim 250$  ns (**figure 7(c)**), leading to enhanced external quantum efficiencies (EQE), particularly in the long wavelength region (750 to 1000 nm) (**figure 7(d)**). The champion cell yielded a PCE of 17.5%, with  $V_{OC}$  of 0.854 V,  $J_{SC}$  of  $28.7 \text{ mA cm}^{-2}$ , and FF of 71.4% (**figure 7(e)**). It is worth noting that the PCE of  $\sim 17\%$  was first certified efficiency for 1.25 eV low- $E_g$  Sn-Pb PSCs. The desirable optoelectronic characteristics of  $(\text{FASnI}_3)_{0.6}(\text{MAPbI}_3)_{0.4}$  were later confirmed by many groups. For instance, Prasanna et al. demonstrated a low- $E_g$  PSC with a PCE of 17.8% using this perovskite composition [98].

Recently, Hayase and coworkers demonstrated  $\text{MA}_{0.5}\text{FA}_{0.5}\text{Sn}_{0.5}\text{Pb}_{0.5}\text{I}_3$  PSCs with a PCE of 17.6%, realized by a conduction band spike structure via incorporating a thin layer of phenyl-C61-butyric acid methyl ester (PCBM) between the perovskite absorber and the  $\text{C}_{60}$  ETL [99]. The insertion of PCBM layer decreased recombination rate at the perovskite/ESL interface and thus increased carrier lifetime from 91.4 to 142.8 ns (**figure 8(a)**), determined by nanosecond transient absorption measurements. As a result, PCE of low- $E_g$  PSCs was increased from 14.2% to 17.6%, with significant enhancements in  $V_{OC}$ ,  $J_{SC}$ , and FF, as shown in **figure 8(b)**. The  $J_{SC}$  of up to  $30.56 \text{ mA cm}^{-2}$  is so far the highest reported value for low- $E_g$  PSCs, however, is likely to be overestimated by  $\sim 8\%$  since  $J_{SC}$  calculated from integrating the EQE curves (**figure 8(c)**) is only  $28.40 \text{ mA cm}^{-2}$ . Similar interface modification has been demonstrated by Xu et al. on the perovskite/HSL interface. Through inserting an ultrathin bulk-heterojunction organic semiconductor layer (PBDB-T:ITIC) between the PEDOT:PSS HSL and the perovskite absorber, they fabricated  $(\text{FASnI}_3)_{0.6}(\text{MAPbI}_3)_{0.4}$  PSCs with a PCE of 18% and a  $V_{OC}$  of 0.86 V [100].

More recently, our group identified that the performance of the low- $E_g$  PSCs is limited by the high carrier density in the mixed Sn-Pb perovskites, which causes higher dark reverse saturation currents in the devices. We demonstrated that bulk and grain boundary passivation via halide (Cl and Br) incorporation led to improved electronic properties

and reduced recombination in the mixed Sn-Pb PSCs, enabling high PCEs exceeding 19% [101, 102]. Particularly for the proper Br-incorporation (6%), the dark current density was reduced by two to three orders of magnitude, as shown in **figure 8(d)** [102]. The best-performing device exhibits a PCE of 19.03% and a high  $V_{OC}$  of 0.888 V, with negligible J-V hysteresis (**figure 8(e)**). The low  $V_{OC}$ -deficit of  $\sim 0.37$  V is comparable to the state-of-the-art medium- $E_g$  PSCs. The steady-state efficiency (SSE) of the device is 18.5%, determined by the maximum output power measurement (**figure 8(f)**). The integrated  $J_{SC}$  from EQE curve (inset of **figure 8(f)**) is  $28.11 \text{ mA cm}^{-2}$ , in good agreement (2% deviation) with  $J_{SC}$  of  $28.72 \text{ mA cm}^{-2}$  derived from the J-V curve.

Besides the popular FA/MA-based mixed Sn-Pb perovskites, high PCEs have also been demonstrated in low- $E_g$  PSCs based on FA/Cs based compositions, i.e.,  $\text{FA}_{1-y}\text{Cs}_y\text{Sn}_x\text{Pb}_{1-x}\text{I}_3$ . Compared with FA/MA-based perovskites, FA/Cs-based low- $E_g$  perovskites show better thermal- and photo-stability, resulting in stable operation under maximum power point tracking (MPPT), as shown in **figure 8(g)**. In 2016, Eperon et al. demonstrated 1.2-eV  $\text{FA}_{0.75}\text{Cs}_{0.25}\text{Sn}_{0.5}\text{Pb}_{0.5}\text{I}_3$  solar cells with a PCE of 14.8% (**figure 8(h)**) with a  $J_{SC}$  of  $26.7 \text{ mA cm}^{-2}$ , confirmed by the EQE measurements (**figure 8(i)**) [103], which is significantly improved compared with the control device based on  $\text{FASn}_{0.5}\text{Pb}_{0.5}\text{I}_3$ . Recently, Leijtens et al. raised the PCE to 15.6% after incorporating MACl and formic acid into the precursor solution [104]. In the meantime, Padture and coworkers systematically investigated the compositional space of  $(\text{FAPbI}_3)_{1-x}(\text{CsSnI}_3)_x$  [105]. The ideal bandgap of  $\sim 1.3$  eV for a single junction solar cell was achieved with an absorber composition of  $(\text{FAPbI}_3)_{0.7}(\text{CsSnI}_3)_{0.3}$ , realizing a PCE of up to 14.6%. They recently improved the PCE to 15.8% through incorporating Lewis-adduct additive  $\text{SnF}_2\cdot 3\text{FACl}$  to the precursor solution [106].

### 3.2 Challenges and issues of low-bandgap perovskite cells

The unsatisfactory performance of mixed Sn-Pb PSCs is one of the key shortcomings that limit the applications of single-junction low- $E_g$  PSCs and all-perovskite tandem solar cells. The relatively poor performance is mainly attributed to inferior film quality of mixed Sn-Pb perovskites than their pure Pb perovskite counterparts, which leads to non-radiative recombination losses in bulk and at the interfaces of the mixed Sn-Pb perovskite films. Due to the high carrier and defect densities, the mixed Sn-Pb perovskites typically suffer from low minority carrier lifetimes, with the highest reported lifetime being  $\sim 250$  ns [97], much inferior to the pure Pb perovskite thin films with carrier lifetimes of a few  $\mu\text{s}$  [107, 108].

**Figure 9** shows  $J_{SC}$  and PCE values versus the bandgap value of low- $E_g$  PSCs reported in the literature. A summary of PV parameters of these low- $E_g$  PSCs can be found in Table 2. Photocurrents in low- $E_g$  PSCs are still much inferior to the expected values. The reported  $J_{SC}$  values of the state-of-the-art low- $E_g$  PSCs that are confirmed by the EQE measurements are still below 30 mA/cm<sup>2</sup>, realizing ~80% of their theoretical potentials. In agreement with the relatively low  $J_{SC}$  values, the average EQE values of ~80% over the visible light range (400 - 800 nm) show insufficient photons-to-charges conversion rates. Moreover, the photocurrent collection drops significantly in the long wavelength range due to insufficient light absorption. Therefore, achieving an adequate conversion at the long wavelengths requires the use of thick low- $E_g$  perovskite absorber layers. However, when the thickness is increased to certain values, other photovoltaic parameters such as  $V_{OC}$  and FF start to decrease due to the presence of a significant number of defects in the mixed Sn-Pb perovskites, which lead to short carrier lifetimes and diffusion lengths. Therefore, strategies to passivate bulk and grain boundaries defects and improve the lifetimes and diffusion lengths in the mixed Sn-Pb perovskites are emergently needed. For instance, we recently demonstrated approaches of incorporating halide doping (Cl and Br) for bulk and grain boundaries passivation in low- $E_g$  mixed Sn-Pb PSCs, leading to high PCEs of up to 19% [101, 102]. With more efforts devoted to the development of highly efficient low- $E_g$  PSCs, higher PCEs exceeding 20% would be expected in the coming years.

Another serious issue for low- $E_g$  PSCs is the lack of material stability and device reliability under operation conditions. The oxidation of  $Sn^{2+}$  to  $Sn^{4+}$  rapidly degraded the optoelectronic properties of mixed Sn-Pb perovskite films, leading to too high hole density and too short carrier lifetime in the films. Additionally, due to the photoinstability of MA-based perovskites [109, 110], the mixed Sn-Pb perovskite films containing MA-cations experience more severe photoinduced decay than FA/Cs-based devices under MPPT measurements [104]. The ease of material degradation also limits the fabrication route and the design of low- $E_g$  mixed Sn-Pb PSCs. Currently, most high-efficiency low- $E_g$  PSCs have been fabricated in the p-i-n device architectures with PEDOT:PSS as the HSL. The metal oxide ESLs (e.g.,  $SnO_2$  and  $TiO_2$ ) and the doped HSLs (e.g., spiro-OMeTAD) are likely to induce the degradation of the mixed Sn-Pb perovskites, deteriorating the device performance. The almost fixed device architecture limits the capability of tailoring interfacial energy level alignment between the mixed Sn-Pb perovskites and the HSL/ESL, which may result in electrical losses at the contacts.

Efforts to improve the stability of low- $E_g$  mixed Sn-Pb PSCs have attracted increasing attention in recent years. Strategies including the use of more stable HSL/ESL or encapsulating layers, incorporation of antioxidant additives,

and the synthesis of more stable perovskite materials have been demonstrated. For instance,  $\text{NiO}_x$  was recently employed by Chi et al. to replace the PEDOT:PSS HSL [111]. A PCE of 17.25% was obtained for low- $E_g$  PSCs based on  $\text{FAPb}_{0.75}\text{Sn}_{0.25}\text{I}_3$ , with an excellent thermal- and photo-stability. Leijtens et al. demonstrated that mixed Sn-Pb PSCs with an ITO capping electrode could survive under an aging condition of 85 °C in the air for more than 300 hours [104]. Jen and coworkers incorporated ascorbic acid as an antioxidant agent in the mixed Sn/Pb PSCs, demonstrating enhanced device stability compared with the devices processed with regular reducing additive  $\text{SnF}_2$  [112]. Most recently, they demonstrated another approach of forming stable mixed Sn-Pb perovskite by using a galvanic displacement reaction [113]. Through adding elemental Sn to the Pb-based perovskite precursor solution, they prepared  $(\text{FAPb}_{0.6}\text{Sn}_{0.4}\text{I}_3)_{0.85}(\text{MAPb}_{0.6}\text{Sn}_{0.4}\text{Br}_3)_{0.15}$  based PSCs and achieved a PCE of 18.21%. More importantly, the encapsulated cells retained more than 90% of their initial efficiencies after the storage in ambient air at room temperature or 80 °C for 1000 or 120 hours, respectively.

#### 4. Perovskite tandem solar cells

##### 4.1 Tandem architectures and working principles

The design of multijunction tandem solar cells aims at mitigating energy losses from thermalization of photoexcited carriers by combining a stack of semiconductor absorber layers with different bandgaps. As depicted in **figure 10(a)**, high-energy photons are absorbed in the top cell to minimize the thermal relaxation loss while the low-energy photons are absorbed in the bottom cell, allowing the maximum harvest of the solar spectrum. The most common multijunction tandem cells are double-junction tandem configurations consisting of a wide- $E_g$  top cell to harvest high energy photons and a low- $E_g$  bottom cell to utilize low energy photons that are transparent to the top cell. Double-junction tandem solar cells are typically fabricated in two main configurations, i.e., four-terminal (4-T) and two-terminal (2-T) tandem architectures, as illustrated in **figure 10(b)-(d)**.

For a 4-T tandem architecture, the two separately fabricated subcells are assembled into a system by either mechanically stacked together (**figure 10(b)**) or coupled with an optical splitter (**figure 10(c)**), with the former being the mainstream configuration whereas the latter being rarely used in practice due to extra costs of optics and supporting units. The subcells can have their different active areas and operate individually at their maximum power points because they are not electronically connected but just optically coupled together. Despite the processing and operational simplicity, the 4-T tandem structure has some inherent drawbacks. Obviously, this configuration possesses

four electrodes since each subcell has its own electrodes. The additional parasitic optical losses and manufacturing costs due to these electrodes are hurdles to minimize energy costs of 4-T tandem technologies. Moreover, the individual operation of the two subcells may raise the balance of system costs due to additional units, such as inverters, wirings, and connections to maintain stable power output from individual cells.

For a 2-T tandem cell, two subcells are fabricated sequentially on the same substrate and are monolithically integrated (**figure 10(d)**). The whole tandem device shares two common electrodes, including a transparent front electrode and an opaque back electrode. The 2-T configuration requires an interconnecting layer (IL) that can either be a heavily doped tunnel junction or a transparent conductive oxide (TCO) recombination layer to provide optical and electrical connection of the two subcells. In contrast to the 4-T tandem configuration, monolithic tandem integration presents a challenge on device fabrication. The processing of IL and the second cell is limited by cell polarity, substrate roughness, deposition temperature, and solvent compatibility.

**Figure 11** shows the theoretical PCEs of double-junction solar cells in both 2-T and 4-T configurations, and the dashed lines label the bandgaps of typical bottom cells, including Si, CIGS, and low- $E_g$  perovskite. Both tandem configurations hold the potential to achieve high PCEs exceeding 42% [9]. For 4-T tandem cells, the overall power output is just a sum of PCEs of the top and bottom cells. Therefore, they have fewer constraints on the choices of bandgaps for both subcells (**figure 11(a)**) and are less sensitive to spectral variations at different locations and over a period of time [114-116]. For monolithic 2-T tandem cells, the two subcells are electrically connected in series, and thus, the voltage of the tandem is the sum of the two subcells while and the current is limited by the lower value of the two. Therefore, maximizing the power output requires the two subcells to generate similar photocurrents under operation conditions, which adds constraints on optical optimization of absorber bandgap and thickness as well as reflection and interference from the whole film stack. Particularly, the current matching prerequisite limits the optimal bandgap of the top perovskite solar cells to ~1.7 to 1.8 eV to match with typical bottom cells (e.g., Si, CIGS, and low- $E_g$  perovskite) with bandgaps of 1.1 to 1.3 eV (**figure 11(b)**) [16, 117, 118]. In practical use, the current mismatch caused by the spectral and temperature differences between constantly varying operating conditions and the standard test conditions may result in energy loss for 2-T tandem cells in the field [114-116].

**Figure 12** plots the evolution of PCEs of notable single-junction and tandem PSCs reported in the literature, summarizing the major developments in recent years. Detailed PV parameters of these perovskite tandem cells are tabulated in **Tables 3 and 4**. Thanks to the advances in the wide- $E_g$  and low- $E_g$  PSCs, all types of tandem solar cells

have rapidly progressed in the past 3-4 years, showing significant increases in reported device efficiencies and the number of the related publications. It is worth noting that there are many tandem devices reported in late 2018, including 2-T and 4-T perovskite/Si and 4-T perovskite/CIGS tandem cells, showing higher PCE than the current world-record (23.7%) of single-junction PSCs. With continually increasing PCEs that are approaching the S-Q limits for single-junction solar cells, perovskite tandem solar cells will become very promising in the near future. The remaining of this section will briefly summarize the developments of various perovskite tandem technologies and discuss the challenges and issues of tandem PSCs.

#### 4.2 Perovskite/Si tandem solar cells

The dominant role of c-Si-based technologies in the current PV market due to high power output, field-proven durability, well-developed supply chains, and rapidly reducing manufacturing costs makes c-Si an ideal candidate to make tandem solar cells with wide- $E_g$  perovskites. Pairing PSCs with c-Si provides a promising path to increase the power output of c-Si solar panels without a significant change in manufacturing costs [119, 120]. To achieve high PCEs exceeding 30%,  $\sim 1.1$ -eV c-Si needs to be paired with wide- $E_g$  perovskites with a bandgap of 1.6 to 1.75 eV (**figure 11**). Thus far, the best-certified efficiency of monolithic perovskite/c-Si tandem solar cells has reached 28.0% by Oxford PV [7], which has already surpassed the PCE of 26.6% for the best single-junction Si cells [7].

##### 4.2.1 Four-terminal perovskite/Si tandem solar cells.

Pioneering attempts to fabricate perovskite/Si tandem cells started in late 2014 when Ballif and McGehee groups individually reported 4-T MAPbI<sub>3</sub>/Si tandem cells with a PCE of 13.4% [121] and 4-T MAPbI<sub>3</sub>/multicrystalline (TI) Si tandem cells with a PCE of 17% [122]. For the latter, limited by the then immature perovskite processing techniques and low-quality Si cells prepared using cast TI-Si wafers, the top and bottom cells delivered PCEs of only 12.7% and 4.3%, respectively, resulting in a total efficiency of 17.0% (**figure 13(a)**) [122]. After that, many efforts have been made to fabricate high-efficiency 4-T perovskite/Si tandem cells. In early 2016, Snaith group fabricated perovskite solar cells with a more photo- and thermal- stable perovskite composition, FA<sub>0.83</sub>Cs<sub>0.17</sub>Pb(I<sub>0.6</sub>Br<sub>0.4</sub>)<sub>3</sub>, with a bandgap of  $\sim 1.74$  eV, realizing a  $V_{OC}$  of 1.2 V for single-junction PSCs [41]. Combining a semitransparent wide- $E_g$  PSC with a Si heterojunction (SHJ) cell enabled a 4-T perovskite/Si tandem configuration with PCEs of 15.1% and 7.3% for the top and filtered bottom cells, respectively, yielding a tandem PCE of 22.4% (**figure 13(b)**). Photocurrent enhancement has been demonstrated in both top and bottom cells compared with the earlier works. However, due to the significant



J-V hysteresis presented in the perovskite top cell, the SSE of the tandem device is ~19.2%. It is worth noting that the FA/Cs based perovskite compositions since then have become the most popular choice for the top cell of perovskite tandem configurations.

Later, Chen et al. fabricate semi-transparent MAPbI<sub>3</sub> perovskite solar cells with ultrathin Cu (1 nm)/Au (7 nm) metal back electrode, allowing near-infrared light to reach Si bottom cell and resulting in 4-T perovskite/Si tandem cells with a PCE of 23.0% [123]. Werner et al. fabricated 4-T perovskite/SHJ tandem cells using a near-infrared-transparent 1.55-eV MAPbI<sub>3</sub> perovskite top cell and a double-sided textured SHJ bottom cell, featuring PCEs of 16.4% and 8.8% for the top and filtered bottom cells, respectively, and a total PCE of 25.2% (**figure 13(c)**) [124]. More recently, Duong et al. reported 4-T perovskite/Si tandem cells consisting of a 1.63-eV quadruple-cation Rb-FA<sub>0.75</sub>MA<sub>0.15</sub>CS<sub>0.1</sub>Pb(I<sub>0.67</sub>Br<sub>0.33</sub>)<sub>3</sub> (with 5% RbI) perovskite top cell and an interdigitated back contact (IBC) Si bottom cell with a PCE of 26.4% [46]. The IBC-Si bottom cells allow improved absorption of near-infrared photons, leading to a high PCE of 10.4% and a high J<sub>SC</sub> of 18.7 mA cm<sup>-2</sup> for a filtered bottom cell (**figure 13(d)**). Jaysankar et al. reported a perovskite/IBC-Si 4-T tandem solar cell with a PCE of 27.1% [125]. The excellent tandem performance was enabled by 1.72-eV semitransparent Cs<sub>0.15</sub>FA<sub>0.85</sub>Pb(I<sub>0.71</sub>Br<sub>0.29</sub>)<sub>3</sub> PSCs with a high V<sub>OC</sub> of 1.22 V and a PCE of 13.8% as well as efficient IBC-Si bottom cells delivering a PCE of 13.3% after filtering with the top PSC.

#### 4.2.2 Two-terminal monolithic perovskite/Si tandem solar cells.

In 2015, McGehee and Buonassisi groups demonstrated the first 2-T monolithic perovskite/Si tandem solar cell [126]. The tandem device, which is comprised of a MAPbI<sub>3</sub> top cell connected to a homojunction Si bottom cell by a n<sup>++</sup>/p<sup>++</sup> Si tunnel recombination junction (**figure 14(a)**), resulted in a modest PCE of 13.7% and a V<sub>OC</sub> of 1.65 V. Thereafter, Albrecht et al. fabricated monolithic perovskite/Si tandem cells consisting of a FA<sub>0.83</sub>MA<sub>0.17</sub>PbI<sub>0.85</sub>Br<sub>0.15</sub> perovskite top cell, a SnO<sub>2</sub>/ITO IL, and a SHJ bottom cell (**figure 14(b)**) [127]. They achieved a PCE of 19.9%, with a high V<sub>OC</sub> of 1.785 V, J<sub>SC</sub> of 14.0 mA cm<sup>-2</sup>, FF of 79.5%. Due to the J-V hysteresis, a slightly lower SSE of 18.1% was obtained.

In late 2015, Ballif group demonstrated monolithic perovskite/Si tandem cells with PCEs of up to 21.2% [128]. The tandem devices employ a semitransparent MAPbI<sub>3</sub> perovskite top cell and a double-side polished Si heterojunction bottom cell (**figure 14(c)**). The tandem devices exhibit significant wavelength-dependent spatial nonuniformities in the photocurrent generation in the subcells due to processing defects of perovskite solar cells and optical loss due to interference introduced by the two parallel Si surfaces [129]. Later, by employing bottom-side

textured Si wafers, a nanocrystalline Si recombination layer, and  $\text{Cs}_{0.19}\text{FA}_{0.81}\text{Pb}(\text{I}_{0.78}\text{Br}_{0.22})_3$  wide-bandgap perovskite films, they improved the PCEs for small size perovskite/Si tandem cells to 22.8%, with a  $V_{\text{OC}}$  of 1.75 V,  $J_{\text{SC}}$  of 16.8  $\text{mA cm}^{-2}$ , and FF of 77.5% [130]. McGehee group reported on the fabrication of efficient monolithic 2-T perovskite/Si tandem solar cells consisting of a 1.63 eV  $\text{FA}_{0.83}\text{Cs}_{0.17}\text{Pb}(\text{I}_{0.83}\text{Br}_{0.17})_3$  perovskite top cell and a single-side textured SHJ bottom cell (**figure 14(d)**) [131]. The champion tandem cells show a PCE of 23.6%, with a  $V_{\text{OC}}$  of 1.65 V, a  $J_{\text{SC}}$  of 18.1  $\text{mA cm}^{-2}$ , and a FF of 79.0%. This tandem design has the light entering the perovskite top subcell from the n-type ESLs ( $\text{LiF/PCBM/SnO}_2/(\text{Zn,Sn})\text{O}_2$ ), differing from the previously reported 2-T tandem cells. More importantly, the combination of more stable FA/Cs-based perovskite composition, a robust ITO IL, and a  $\text{SnO}_2/(\text{Zn,Sn})\text{O}_2$  buffer layer prepared by atomic layer deposition [132] enables a decent device stability that withstands a damp heat test at 85 °C and 85% relative humidity for more than 1000 hours. Using a similar device architecture, Chen et al. recently reported an advanced engineering technique by incorporating  $\text{MACl}$  and  $\text{MAH}_2\text{PO}_2$  into perovskite precursor to reduce the  $V_{\text{OC}}$ -deficit of 1.64 eV perovskite top cell to less than 0.5 V, which enables 2-T perovskite/SHJ tandem cells with a high  $V_{\text{OC}}$  of 1.80 V, a  $J_{\text{SC}}$  of 17.8  $\text{mA cm}^{-2}$ , and a FF of 79.4%, resulting in a PCE of 25.4% [133].

Most state-of-the-art 2-T monolithic perovskite/Si tandem solar cells are based on silicon bottom cells with a polished front surface due to the difficulty of solution-processing the perovskite subcells on an uneven surface. Recently, Sahli et al. demonstrated the fabrication of monolithic 2-T perovskite/Si tandem solar cells on the double-side textured monocrystalline silicon wafers (**figure 14(e)**) [134]. The tandem devices based on double-textured Si wafer yield a certified SSE of 25.2%, featuring a high  $J_{\text{SC}}$  of 19.5  $\text{mA cm}^{-2}$  [134], which is 3  $\text{mA cm}^{-2}$  higher than perovskite/Si tandem cells fabricated on single-side polished Si wafers [130]. The successful fabrication of perovskite/Si tandem devices on pyramid textured Si wafers was enabled by thermally evaporated organic hole selective layer, i.e., 2,2',7,7'-tetra(N,N-di-tolyl)amino-9,9-spiro-bifluorene (Spiro-TTB) and a vapor-solution hybrid sequential deposition approach [135] to prepare conformal perovskite films. Although the demonstration of processing 2-T perovskite/Si solar cells on fully textured Si wafers shows promising results, the devices still suffer from relatively low FF of 69-73% [134].

More recently, optical designs of 2-T monolithic perovskite/Si tandem cells to reduce parasitic optical losses have been taking into consideration. McGehee group demonstrated PCEs up to 25% for perovskite/Si tandem cells with a 1  $\text{cm}^2$  active area through minimizing current and voltage losses by combining a thin top transparent electrode, metal fingers, and a polydimethylsiloxane (PDMS) antireflection foil [136]. The champion tandem cell delivers a  $V_{\text{OC}}$  of

1.77 V, a  $J_{SC}$  of 18.4 mA cm<sup>-2</sup>, a FF of 77%, and a PCE of 25%. Albrecht group fabricated 2-T monolithic 1.66-eV perovskite/SHJ tandem cells with light-management (LM) foils on the illumination side (**figure 14(f)**) and demonstrated a PCE of 25.5%, with a  $V_{OC}$  of 1.76 V, a  $J_{SC}$  of 18.5 mA cm<sup>-2</sup>, and a FF of 78.5% [137].

Besides the tandem cells based on SJH-based c-Si solar cells, the homojunction c-Si technologies, which have the market dominance with a global market share of around 93%, are considered as an ideal candidate for the marketization of perovskite/Si tandem solar cells. Recently, Weber group demonstrated an SSE of 22.5% and a  $V_{OC}$  of 1.75 V on a 1 cm<sup>2</sup> perovskite/homojunction c-Si tandem cells [138]. In the meantime, Ho-Baillie group demonstrated efficient large-area MAPbI<sub>3</sub>/homojunction silicon tandem solar cells [139]. The champion device with an area of 4 cm<sup>2</sup> achieved a PCE of 21.0% while the 16 cm<sup>2</sup> large area device yielded an SSE of 17.1%. More recently, they combined (FAPbI<sub>3</sub>)<sub>0.83</sub>(MAPbBr<sub>3</sub>)<sub>0.17</sub> perovskite and rear-side-textured homojunction Si cells into 2-T monolithic tandem configuration and demonstrated an SSE of 21.8% on 16 cm<sup>2</sup> [140]. Their work provides a direction for commercially relevant and low-cost perovskite/homojunction Si tandem cells, paving the way toward the commercialization of perovskite/Si tandem technologies.

#### 4.3 Perovskite/chalcogenide thin film tandem solar cells

The marriage between emerging perovskite and commercially available CIGS PV technologies makes it possible to realize ultra-high efficient and low-cost thin-film tandem solar cells. Both thin-film technologies possess excellent photovoltaic properties, such as tunable bandgaps, high absorption coefficients, and defect tolerance, and can be prepared via solution-based methods, making them the ideal partners for fabricating tandem solar cells. Thanks to the advances in fabricating high-efficiency wide-E<sub>g</sub> PSCs, the PCEs of 4-T perovskite/CIGS solar cells has rapidly increased in recent year, achieving ~25% in 2018 [141] (**figure 12**). The performance of 4-T perovskite/CIGS tandem cells is inferior to that of 4-T perovskite/Si tandem cells, mainly due to the lower efficiencies of CIGS cells compared with cells based on c-Si. The fabrication of 2-T perovskite/CIGS tandem cells is very challenging due to the delicate processing requirements for both subcells and the IL. Thus far, only Yang group reported on the fabrication of high-efficiency 2-T monolithic perovskite/CIGS tandem cells with a PCE exceeding 22% [142]. There are expected to be more works on 2-T perovskite/CIGS tandem solar cells in the future.

##### 4.3.1 Four-terminal perovskite/chalcogenide tandem solar cells.

In late 2014, Bailie et al. fabricated the first 4-T perovskite/CIGS tandem solar cells, achieving a total PCE of 18.6% by summing up 12.7% efficiency for a MAPbI<sub>3</sub> top cell and a 5.9% efficiency for a filtered CIGS bottom cell [122]. Soon after that, Yang et al. fabricated the semitransparent perovskite cells with multilayer transparent electrode and demonstrated 4-T perovskite/CIGS tandem cells with a PCE of 15.5% [143]. In the meantime, Kranz et al. demonstrated 4-T polycrystalline thin film tandem cells with a combination of a regular structure MAPbI<sub>3</sub> perovskite top cell and a CIGS bottom cell, resulting in a PCE of 19.5%, with PCEs of 12.1% and 7.4% for the perovskite and filtered CIGS cells [144]. Fu et al. fabricated semitransparent MAPbI<sub>3</sub> perovskite solar cells in the n-i-p structure of FTO/ZnO/PCBM/perovskite/Spiro-OMeTAD/MoO<sub>3</sub>/In<sub>2</sub>O<sub>3</sub>:H and demonstrated 4-T perovskite/CIGS tandem cells with a PCE of 20.5% [145]. Later, they improved the performance of the perovskite top cell by employing the substrate configuration, which allows light to enter the devices from the film side [146]. Using these substrate-type perovskite solar cells constructed by a film stack of glass/In<sub>2</sub>O<sub>3</sub>:H/PTAA/MAPbI<sub>3</sub>/PCBM/ZnO/ZnO:Al/metal grid (**figure 15(a)**), they demonstrated 4-T thin film perovskite/chalcogenide tandem cells with PCEs of 22.1% and 20.9% for CIGS and CIS bottom cells. For the 4-T perovskite/CIGS tandem cells, the top and bottom subcells yielded PCEs of 16.1% and 6.0% and high J<sub>SC</sub> values of 19.1 and 12.1 mA cm<sup>-2</sup>, respectively (**figure 15(b)**) [146].

More recently, wide-E<sub>g</sub> perovskites have been used to replace medium-E<sub>g</sub> MAPbI<sub>3</sub>, allowing more infrared photons to enter the bottom CIGS cells. Shen et al. fabricated semitransparent perovskite solar cells with Cs<sub>0.05</sub>Rb<sub>0.05</sub>FA<sub>0.765</sub>MA<sub>0.135</sub>Pb(I<sub>1-x</sub>Br<sub>x</sub>)<sub>3</sub> absorbers at bandgap of 1.62 (x = 0.15) and 1.75 eV (x = 0.4) in the n-i-p structure (**figure 15(c)**), achieving semitransparent single-junction device PCEs of 18.1% and 16.0% [147]. Combining these PSCs with a 16.5% CIGS bottom cell resulted in 4-T perovskite/CIGS tandem efficiencies of 23.9% (**figure 15(d)**) and 23.4%, respectively. At the 2018 EU PVSEC conference, Imec and ZSW researchers announced a record efficiency of 24.6% for 4-T perovskite/CIGS tandem cells [141], showing the potential adoption of this 4-T perovskite/CIGS technique by industry in the future.

#### 4.3.2 Two-terminal perovskite/chalcogenide tandem solar cells.

As a proof of concept, Todorov et al. first fabricated monolithic perovskite/Cu<sub>2</sub>ZnSn(S,Se)<sub>4</sub> (CZTSSe) [148] and perovskite/CIGS (**figure 16(a)**) [149] tandem solar cells using solution-processed chalcopyrite bottom cells. The resulting tandem devices with CZTSSe and CIGS subcells exhibited PCEs of 4.6% and 10.9%, respectively. Though the tandem efficiencies are much inferior to the PCEs of single-junction cells, the attempts for integrating perovskite

and chalcogenide thin film solar cells into the 2-T tandem configuration motivated subsequent studies on monolithic perovskite/chalcogenide tandem solar cells.

Due to the difficulty of processing interconnecting layer and perovskite top cells on the completed CIGS thin film solar cells, there are only a few reports that focus on the fabrication of 2-T perovskite/CIGS tandem. In 2018, Uhl et al. fabricated monolithically interconnected perovskite/chalcogenide tandem solar cells using a solution-processed semitransparent MAPbI<sub>3</sub> top cell and a CuIn(Se,S)<sub>2</sub> ( $E_g = 1.03$  eV) bottom cell prepared by a molecular ink deposition method (**figure 16(b)**), yielding a tandem efficiency of 8.55% [150]. No one has reported high efficiency 2-T perovskite/CIGS tandem solar cells until a breakthrough that was made recently by Yang and coworkers. Through chemical and mechanical polishing the top contact of CIGS solar cells and applying a heavily doped PTAA HSL, they achieved 2-T perovskite/CIGS tandem cells with 1.59-eV Cs<sub>0.09</sub>FA<sub>0.77</sub>MA<sub>0.14</sub>Pb(I<sub>0.86</sub>Br<sub>0.14</sub>)<sub>3</sub> perovskite and 1.0-eV CIGS subcells (**figure 16(c)**), which exhibited a PCE of 22.4% with a  $V_{OC}$  of 1.774 V, a  $J_{SC}$  of 17.3 mA cm<sup>-2</sup>, and a FF of 73.1% (**figure 16(d)**) [142]. The  $J_{SC}$  was confirmed by the EQE measurements, which show integrated  $J_{SC}$  values of 18.20 and 17.76 mA cm<sup>-2</sup> for the top and bottom cells, respectively (**figure 16(e)**), consistent with the results from the J-V measurements. The perovskite/CIGS tandem cells without encapsulation retained ~90% of their initial PCEs after 500 hours of continuous operation under ambient conditions, demonstrating decent device stability. During the revision of this paper, a 21.6%-efficient 2-T perovskite/CIGS tandem cell was reported by Albrecht et al. [151]

#### 4.4 All-perovskite tandem solar cells

Compared with other perovskite tandem technologies, all-perovskite tandem cells possess unique advantages, including low-temperature processes for all subcells, compatibility with flexible and lightweight applications, and potentially low fabrication and environmental costs [152, 153]. Though potentially promising, it is challenging to fabricate efficient all-perovskite tandem solar cells due to the lack of efficient low- $E_g$  perovskite bottom subcells and difficulty of monolithically integrating two perovskite subcells in the 2-T tandem configuration. The recent progress has propelled the PCEs of 4-T and 2-T all-perovskite tandem solar cells to 23.1% [154] and 21% [101], respectively (**figure 12**), approaching their perovskite/Si and perovskite/CIGS counterparts. Clearly, fabrication of high-efficiency low- $E_g$  PSCs is the key for realizing the potential of the all-perovskite tandem solar cells.

##### 4.4.1 Four-terminal all-perovskite tandem solar cells.

The studies on all-perovskite tandem solar cells were lagging behind the progress of other perovskite tandem technologies due to the challenges of fabricating efficient and stable low- $E_g$  PSCs. In 2016, Li et al. demonstrated the proof-of-concept 4-T all-perovskite tandem solar cells using MAPbBr<sub>3</sub> and MAPbI<sub>3</sub> as the top and bottom cells [155], achieving a PCE of ~9.5%. Yang et al. demonstrated the first 4-T all-perovskite tandem solar cell with a low- $E_g$  PSC by combining a 1.55-eV MAPbI<sub>3</sub> top cell and a 1.33-eV MA<sub>0.5</sub>FA<sub>0.5</sub>Pb<sub>0.75</sub>Sn<sub>0.25</sub>I<sub>3</sub> bottom cell, achieving a high PCE of 19.1% after adding up PCEs of 13.5% and 5.6% for the top and filtered bottom cells, respectively (**figure 17(a)**) [95]. A thin absorber layer thickness of the medium- $E_g$  MAPbI<sub>3</sub> was used to allow sufficient photons to enter the bottom cell. As a result,  $J_{SC}$ s of 16.7 and 9.1 mA cm<sup>-2</sup> were obtained for the top and filtered bottom cells.

Later, Eperon et al. constructed 4-T tandem cells with a better optically complementary absorber combination consisting of a 1.6-eV FA<sub>0.83</sub>CS<sub>0.17</sub>Pb(I<sub>0.83</sub>Br<sub>0.17</sub>)<sub>3</sub> top cell and a 1.2-eV FA<sub>0.75</sub>CS<sub>0.25</sub>Sn<sub>0.5</sub>Pb<sub>0.5</sub>I<sub>3</sub> bottom cell [103]. They achieved PCEs of 15.8% and 4.5% for the top and filtered bottom cells, respectively, resulting in a PCE of 20.3% for the 4-T tandem cells (**figure 17(b)**). Our group further enhanced the record 4-T tandem cell efficiencies to 21.2% by pairing the 1.58-eV FA<sub>0.3</sub>MA<sub>0.7</sub>PbI<sub>3</sub> and 1.25-eV (FASnI<sub>3</sub>)<sub>0.6</sub>(MAPbI<sub>3</sub>)<sub>0.4</sub> cells [97], and to 23.1% after replacing the top cell with a wide- $E_g$  FA<sub>0.8</sub>CS<sub>0.2</sub>Pb(I<sub>0.7</sub>Br<sub>0.3</sub>)<sub>3</sub> absorber (**figure 17(c)**) [154]. For the record efficiency device, the incorporation of paraffin oil as an optical coupling layer between the two subcells reduces the optical loss at the air/glass interfaces, enabling PCEs of 15.7% and 7.4% for the top and filtered bottom cells, respectively.

#### 4.4.2 Two-terminal all-perovskite tandem solar cells.

For 2-T all-perovskite tandem solar cells, the most critical component is the IL that not only connects two subcells but also protects the underlying subcell from any damages introduced by processing the second cell. The proof-of-concept monolithic 2-T all-perovskite tandem solar cells was first reported in 2015 by Zhou and coworkers [156]. The tandem device is comprised of two MAPbI<sub>3</sub> cells connected by organic ILs (**figure 18(a)**). Although the tandem cell yielded an unsatisfactory PCE of only 7%, it showed a high  $V_{OC}$  of up to 1.89 V, close to the sum of the two subcells, demonstrating the monolithic design of all-perovskite tandem cells. In the meantime, Heo and Im fabricated 2-T MAPbBr<sub>3</sub>-MAPbI<sub>3</sub> tandem solar cells by physically laminating two separated subcells together (**figure 18(b)**), achieving a PCE of 10.8% and a high  $V_{OC}$  of 2.25 V [157]. However, due to the relatively large bandgap of the MAPbI<sub>3</sub> (1.55 eV) bottom cell and the physically contacted interconnecting interface, a small  $J_{SC}$  of only 8.3 mA cm<sup>-2</sup> was obtained.

The first 2-T monolithic all-perovskite tandem cell employing a low- $E_g$  mixed Sn-Pb PSCs was reported by McGehee, Snaith, and co-workers in 2016 [103]. The 2-T tandem cells consist of a 1.8-eV  $\text{FA}_{0.83}\text{Cs}_{0.17}\text{Pb}(\text{I}_{0.5}\text{Br}_{0.5})_3$  top cell and a 1.2-eV  $\text{FA}_{0.75}\text{Cs}_{0.25}\text{Sn}_{0.5}\text{Pb}_{0.5}\text{I}_3$  bottom cell connected by zinc-tin oxide (ZTO)/ $\text{SnO}_2$ /ITO interconnecting layers (**figure 18(c)**). The sputtered ITO layer not only provides an optical and electrical connection to the subcells but also protects the first-deposited subcell from processing damages from solution-deposition of the second subcell. The use of two subcells with complementary bandgaps allows broad absorption of the solar spectrum. The best performing device achieved a PCE of 16.9%, with a  $V_{OC}$  of 1.66 V, a  $J_{SC}$  of 14.5  $\text{mA}/\text{cm}^2$ , and a FF of 70%. Later, after adjusting the top cell more photostable composition,  $\text{FA}_{0.83}\text{Cs}_{0.17}\text{Pb}(\text{I}_{0.7}\text{Br}_{0.3})_3$ , and incorporating MAI and formic acid to improve the quality of the  $\text{FA}_{0.75}\text{Cs}_{0.25}\text{Sn}_{0.5}\text{Pb}_{0.5}\text{I}_3$  bottom cells, they demonstrated a PCE of 19.1% for 2-T perovskite tandem cells (**figure 19(a)**) [104]. The best-performing device shows a  $V_{OC}$  of 1.81 V and a matched  $J_{SC}$  of 14.8  $\text{mA cm}^{-2}$ , significantly improved from their previous devices.

Jen and co-workers used  $\text{MA}_{0.9}\text{Cs}_{0.1}\text{Pb}(\text{I}_{0.6}\text{Br}_{0.4})_3$  ( $E_g = 1.82$  eV) and  $\text{MASn}_{0.5}\text{Pb}_{0.5}\text{I}_3$  ( $E_g = 1.22$  eV) subcells connected by a sputtered ITO recombination layer to construct 2-T all-perovskite tandem cells (**figure 18(d)**), achieving a PCE of 18.4% (**figure 19(b)**) [158]. It is worth noting that the high  $V_{OC}$  of 1.98 V is approaching 80% of the theoretical voltage limit for the absorber combination. However, the relatively low  $J_{SC}$  of  $\sim 12.5$   $\text{mA cm}^{-2}$  limits the PCE of the tandem devices. Most recently, our group demonstrated 2-T perovskite tandem cells consisting of 1.75-eV wide- $E_g$   $\text{FA}_{0.8}\text{Cs}_{0.2}\text{Pb}(\text{I}_{0.7}\text{Br}_{0.3})_3$  top cell and a 1.25-eV low- $E_g$   $(\text{FASnI}_3)_{0.6}(\text{MAPbI}_3)_{0.4}$  bottom cell connected by a simple vacuum-processed ILs of  $\text{MoO}_3/\text{Ag}/\text{ITO}$  (**figure 18(e)**) [101]. A bulk-passivation strategy was employed to enlarge the grain size, increase carrier mobilities, reduce electronic disorder, and suppress trap-assisted recombination in the low- $E_g$  mixed Sn-Pb perovskite films, leading to improved performance of low- $E_g$  PSCs with an absorber layer thickness of over 750 nm. This advance in high-quality low-bandgap perovskite layers enables the fabrication of efficient 2-T all-perovskite solar cells with a  $V_{OC}$  of 1.92 V,  $J_{SC}$  of 14.0  $\text{mA cm}^{-2}$ , FF of 78.1%, yielding a PCE of 21% (**figure 19(c)**). Our tandem devices show decent operational stability, retaining over 85% of initial PCEs after 80 hours of continuous operation under AM1.5G solar radiation. Besides commonly used ITO-based IL, Choy and coworkers recently demonstrated a PCE of 17.9% for 2-T all-perovskite tandem cells with an ultrathin Cu/Au metal thermionic emission based interconnecting layer [159], providing a new route to monolithically integrate two perovskite subcells.

Beyond the solution-processed all-perovskite solar cells, perovskite solar cells can also be prepared by the physical vapor deposition method. Bolink and co-workers combined solution-processed wide- $E_g$   $\text{FA}_{0.75}\text{Cs}_{0.15}\text{Pb}(\text{I}_{0.3}\text{Br}_{0.7})_3$

perovskite top cells with vacuum-deposited MAPbI<sub>3</sub> bottom cells to build 2-T all-perovskite tandem solar cells (**figure 18(f)**), achieving a champion PCE of 18.1%, with a high  $V_{OC}$  of 2.14 V,  $J_{SC}$  of 9.7 mA cm<sup>-2</sup>, FF of 75.6% (**figure 19(d)**) [160]. More recently, they demonstrated all-vacuum processed MAPbI<sub>3</sub>/MAPbI<sub>3</sub> tandem cells, which yield a PCE exceeding 18% and an unprecedentedly high  $V_{OC}$  of 2.30 V [161]. The low total  $V_{OC}$  deficit of ~900 mV for two subcells is attributed to high-quality vacuum-processed perovskite thin films and entirely evaporated organic interconnecting layers. This work demonstrates the promise of the vacuum-based process for fabricating all-perovskite tandem solar cells.

#### 4.5 Limitations and challenges of perovskite tandem solar cells

##### 4.5.1 Scaling up and commercialization.

To achieve commercial readiness of perovskite tandem technologies, the design and fabrication of large-area tandem cells and modules will become an important consideration. So far, most perovskite tandem solar cells reported in the literature have active areas on the order of 0.1 to 1 cm<sup>2</sup>. These small size designs allow the commonly used spin-coating methods for processing single-junction PSCs to be translated directly to the fabrication of tandem cells. However, for industrial production and application, large-area fabrication techniques and implementation of tandem cell designs and module integration are yet to be demonstrated.

Research work on single-junction and tandem PSCs has been moving forward toward large area devices. Several research groups have recently developed scalable deposition techniques for fabricating mini-modules with sizes of up to 100 cm<sup>2</sup> [162-166]. For instance, Han and coworkers fabricated printable perovskite solar modules with 10 cm by 10 cm area (**figure 20(a)**) and assembled a 7 m<sup>2</sup> prototype of perovskite solar panels (**figure 20(b)**) [166], demonstrating a viable route toward the realization of large-area perovskite solar modules. The perovskite solar modules can be used for constructing 4-T tandem PSCs if a TCO layer is used as the back electrode. Jaysankar et al. recently demonstrated a scalable design of 4-T perovskite/Si solar module employing a semi-transparent monolithically integrated perovskite solar module and an interdigitated back contact (IBC) c-Si cell (**figure 20(c)**) [167]. The tandem cell prototype was simply assembled by stacked 4 cm<sup>2</sup> perovskite and Si cells together, as illustrated in **figure 20(d)**, delivering a PCE of 23.9% [168].

For 2-T perovskite/Si tandem cells, the main challenge is to deposit uniform and smooth perovskite films on large area silicon wafers. Sahli et al. demonstrated 18%-efficient monolithic perovskite/SHJ tandem cells on large area



(12.96 cm<sup>2</sup>) (**figure 20(e)**) using a vapor-solution two-step method [130]. Zheng et al. fabricated 16 cm<sup>2</sup> 2-T perovskite/homojunction Si cells (**figure 20(f)**) using solution-based two-step methods and achieved PCEs of 17.1% [140]. Moreover, the leading company in the field of PSCs, Oxford PV, has already demonstrated the fabrication of 156 mm by 156 mm (243 cm<sup>2</sup>) perovskite silicon tandem solar cells at the industrial pilot production line [169]. This achievement shows the feasibility of driving the 2-T perovskite/Si tandem technologies from the lab demonstration toward high volume production.

Compared with wafer-based Si PV technologies, the designs and fabrication of 2-T perovskite/CIGS and all-perovskite thin-film tandem solar cells are much more challenging. In particular, the monolithic integration designs of thin-film tandem solar modules require careful considerations on the separation and interconnection of individual cells. Moreover, the performances of CIGS and low-E<sub>g</sub> perovskite bottom cells are still much inferior to c-Si solar cells and are prone to degradation during the processing of the second subcell and IL. The complexity of processing these tandem configurations makes it extremely difficult to fabricate large-area thin film tandem modules. Therefore, these thin-film perovskite tandem cells are still in the early stages of the development, with the focuses on investigating the basic science of the device operation and validating the technical approaches. There is still a long way to go before the commercialization of perovskite thin-film tandem technologies can be seriously considered.

#### 4.5.2 Device reliability of tandem perovskite solar cells.

While tandem PSCs hold the promise to deliver high PCEs, the requirement of reliability to match the 25-year lifetime of Si solar cells is currently one of the major obstacles on their path toward commercialization. Although some promising stability testing results have been reported in the literature in recent years, the long-term stability of PSCs is yet to be fully demonstrated. Especially for tandem PSCs, limited by the small numbers of publications, standardized stability testing results have rarely been reported. Recently, Bush et al. reported that using industry-standard glass/glass encapsulation packaging, semitransparent PSCs and 2-T perovskite/Si tandem cells can survive the damp heat test (85% relative humidity and 85 °C temperature) for more than 1000 hours [131]. Passing this test is an encouraging signal showing the feasibility to achieve long-term stability in perovskite/Si tandem solar cells. Han et al. reported 2-T perovskite/CIGS tandem cells without encapsulation maintained 88% of their initial PCEs after 500 hours of continuous one sun illumination [142]. The lifetime would be longer if proper encapsulation can be applied.

All-perovskite tandem solar cells have a critical concern on the stability of low-E<sub>g</sub> PSCs. Due to the vulnerability of

mixed Sn-Pb perovskites against oxygen and moisture, the low- $E_g$  PSCs require complete encapsulation to work in the ambient conditions for a long time. Our group recently demonstrated that the synthesis of high-quality mixed Sn-Pb perovskite films enabled all-perovskite tandem solar cell that retained 85% of its initial PCE after 80 hours of continuous operation under one sun illumination. Although such short lifetime is not comparable with the tandem cells based on c-Si and CIGS, these results are encouraging for further improvements of all-perovskite tandem solar cells. Nonetheless, stability issues of tandem PSCs need to be fully addressed before translating these promising PV technologies demonstrated in laboratories to real-world applications [170].

**5. Conclusion and outlook**

The past few years have witnessed the rapid progress of single-junction and tandem PSCs. Thanks to the research advances in wide- $E_g$  and low- $E_g$  single-junction PSCs, various high-efficiency tandem PSCs, including perovskite/Si, perovskite/CIGS, and all-perovskite tandem solar cells in 4-T and 2-T configurations have been demonstrated. With the record PCEs of laboratory-made tandem PSCs approaching and even surpassing commercially available solar cells based on single-junction PV technologies, it is important to start to consider strategies that can bridge the gap between laboratory-made devices and efficient and reliable commercially manufactured modules.

As the PCEs of various tandem PSCs are expected to continuously increase in the future, more commercially relevant questions should be asked such as whether the device architectures and deposition methods are applicable for large-area module fabrication and whether the newly developed approaches are technically and financially feasible. There needs to be an area of research focusing on developing processing techniques for specific PSCs based on tandem configurations. For instance, conformal coating of perovskite thin films on textured Si wafer has recently been demonstrated using the hybrid two-step method [134], while conventional spin-coating used for high-efficiency single-junction PSCs cannot deliver the same results. For delicate thin-film solar cells (CIGS and perovskite) which are sensitive to high temperatures and environment, depositing the second perovskite subcells on them to construct tandem cells may require special treatments and protective remedies to mitigate the possible processing damages. These require researchers to explore alternative tandem-specific deposition approaches. The ideal route would be vacuum-based deposition methods [160, 161], which are not limited by the nonuniform surface and solvent compatibility and can be adapted to the mild-vacuum, low-temperature, high-throughput industrial production. The

remaining challenges are how to achieve high-quality perovskite films with different perovskite compositions, which require more research efforts.

Future work also needs to focus on developing more stable perovskite tandem modules. The desired device stability requires not only the advanced engineering on perovskite compositions and cell structures to enhance the stability of PSCs but also the module frame and encapsulation designs that prevent water and oxygen ingress [171-175] as well as the leakage of water-soluble toxic Pb and Sn compounds [153, 176-178]. Once robust encapsulation can be implemented, tandem PSCs will have a chance to achieve sufficiently long-term stability, which will benefit the adaption of these promising tandem techniques in the market. This is particularly attractive for the already established c-Si PV industry. Pairing with PSCs will boost the power generation of current c-Si solar cells provided the stability issue can be addressed. While for the less mature CIGS technologies, the adaption will take longer time since difficult processing related engineering issues are still presented, and more devices need be demonstrated to ensure the feasibility to enter the production. In the long future, all-perovskite tandem solar cells hold the potential to become the leader in the perovskite PV field due to their ultrahigh efficiency and low-cost. However, the route toward this ultimate promising perovskite PV technology is the most challenging one because of the performance and stability issues of the low- $E_g$  PSCs. If these critical remaining issues can be resolved, all-perovskite tandem solar cells will fulfill their promise to deliver more electrical power at lower costs than today's PV technologies.

#### Acknowledgements

This work was financially supported by Air Force Research Laboratory, Space Vehicles Directorate (contract # FA9453-11-C-0253), the Office of Naval Research under Contract No. N00014-17-1-2223, National Science Foundation under contract no. DMR-1807818 and ECCS-1807818, the U.S. Department of Energy (DOE) SunShot Initiative under the Next Generation Photovoltaics 3 program (DE-FOA-0000990), and the Ohio Research Scholar Program.

## Figures

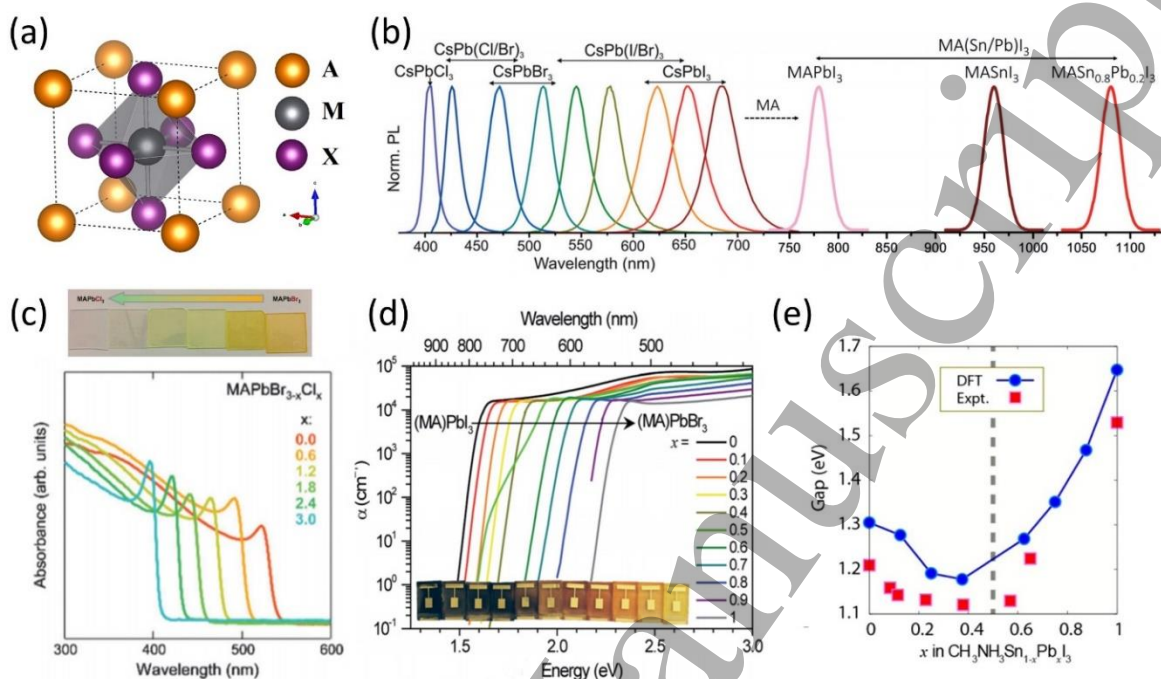


**Figure 1.** (a) Sketch of  $AMX_3$  perovskite crystal structure. Reprinted with permission from [25], copyright 2018 Elsevier. (b) Normalized PL emissions of various metal halide perovskites. Reprinted with permission from [30], copyright 2018 Wiley-VCH. (c) Photos and absorbance spectra of  $MAPbBr_{3-x}Cl_x$ . Reprinted with permission from [31], copyright 2015 Royal Society of Chemistry. (d) Photos and absorbance spectra of  $MAPbI_{3-x}Br_x$ . Reprinted with permission from [34], copyright 2015 Royal Society of Chemistry. (e) Calculated and measured bandgaps of  $MASn_{1-x}Pb_xI_3$ . Reprinted with permission from [36], copyright 2015 American Chemical Society.

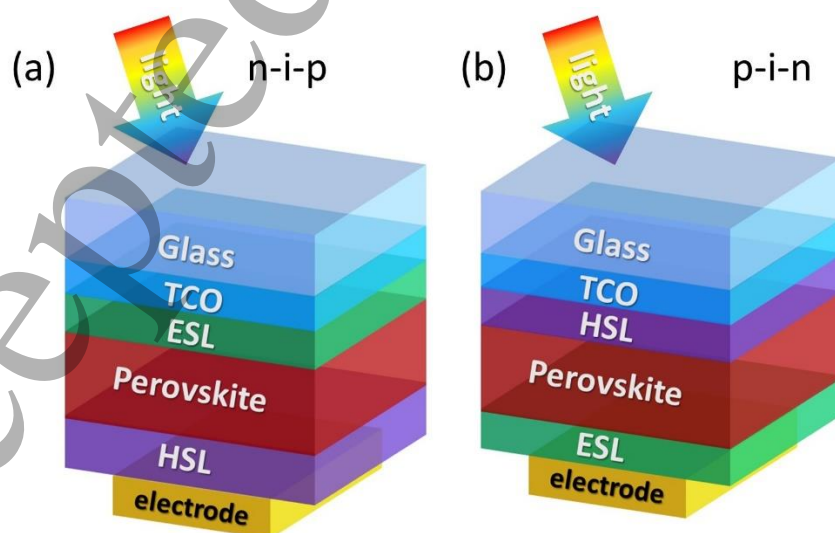


**Figure 2.** Schematics of two main PSC architectures, including (a) regular n-i-p and (b) inverted p-i-n structures.

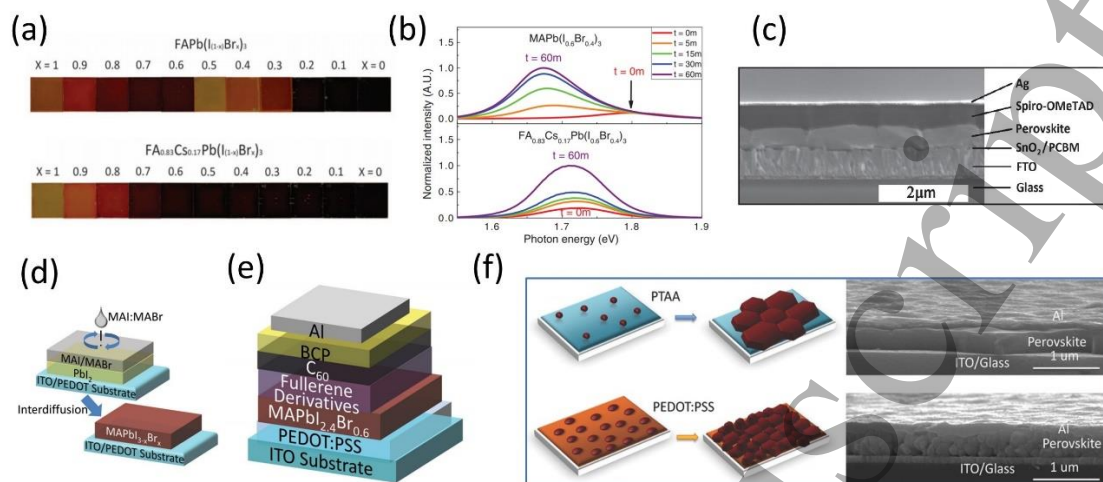


**Figure 3.** (a) Photos of  $\text{FAPb}(\text{I}_{1-x}\text{Br}_x)_3$  and  $\text{FA}_{0.83}\text{Cs}_{0.17}\text{Pb}(\text{I}_{1-x}\text{Br}_x)_3$  films. (b) PL spectra of  $\text{MAPb}(\text{I}_{0.6}\text{Br}_{0.4})_3$  and  $\text{FA}_{0.83}\text{Cs}_{0.17}\text{Pb}(\text{I}_{0.6}\text{Br}_{0.4})_3$  films after periods of light exposure. (c) Cross-sectional scanning electron (SEM) microscopic image of a wide- $E_g$  PSC with the n-i-p structure. Panels (a)-(c) are reprinted with permission from [41], copyright 2016 American Association for the Advancement of Science. Schematics of (d) the sequential deposition method and (e) a p-i-n PSC device structure. Reprinted with permission from [43], copyright 2015 WILEY-VCH. (f) Schematics and cross-sectional SEM images of  $\text{MAPb}(\text{Br}_{0.27}\text{I}_{0.73})_3$  films deposited on PTAA and PEDOT:PSS coated ITO substrates. Reprinted with permission from [44], copyright 2016 WILEY-VCH.

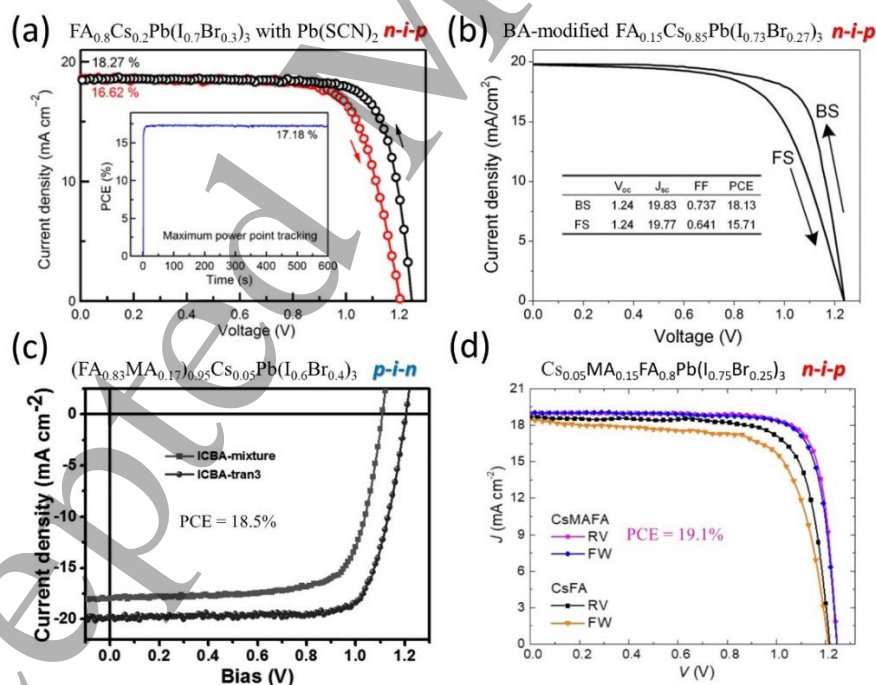


**Figure 4.** J-V curves of the-state-of-the-art wide- $E_g$  PSCs, including (a) n-i-p  $\text{FA}_{0.8}\text{Cs}_{0.2}\text{Pb}(\text{I}_{0.7}\text{Br}_{0.3})_3$ , (b) n-i-p BA- $\text{FA}_{0.15}\text{Cs}_{0.85}\text{Pb}(\text{I}_{0.73}\text{Br}_{0.27})_3$ , (c) p-i-n  $(\text{FA}_{0.83}\text{MA}_{0.17})_{0.95}\text{Cs}_{0.05}\text{Pb}(\text{I}_{0.6}\text{Br}_{0.4})_3$ , and n-i-p  $\text{Cs}_{0.05}\text{MA}_{0.15}\text{FA}_{0.8}\text{Pb}(\text{I}_{0.75}\text{Br}_{0.25})_3$ . Panel (a) is adapted with permission from [47], copyright 2017 American Chemical Society. Panel (b) is adapted with permission from [49], copyright 2017 WILEY-VCH. Panel (c) is adapted with permission from [51], copyright 2017 WILEY-VCH. Panel (d) is adapted with permission from [53], copyright 2018 Springer Nature.



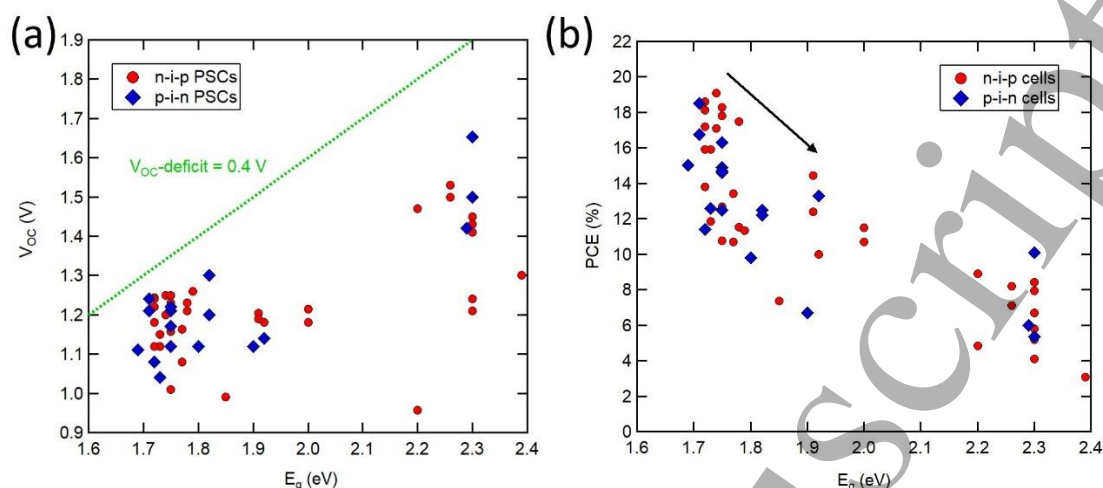


**Figure 5.** Plots of (a)  $V_{OC}$  and (b) PCE versus bandgap of wide- $E_g$  PSCs reported in the literature.

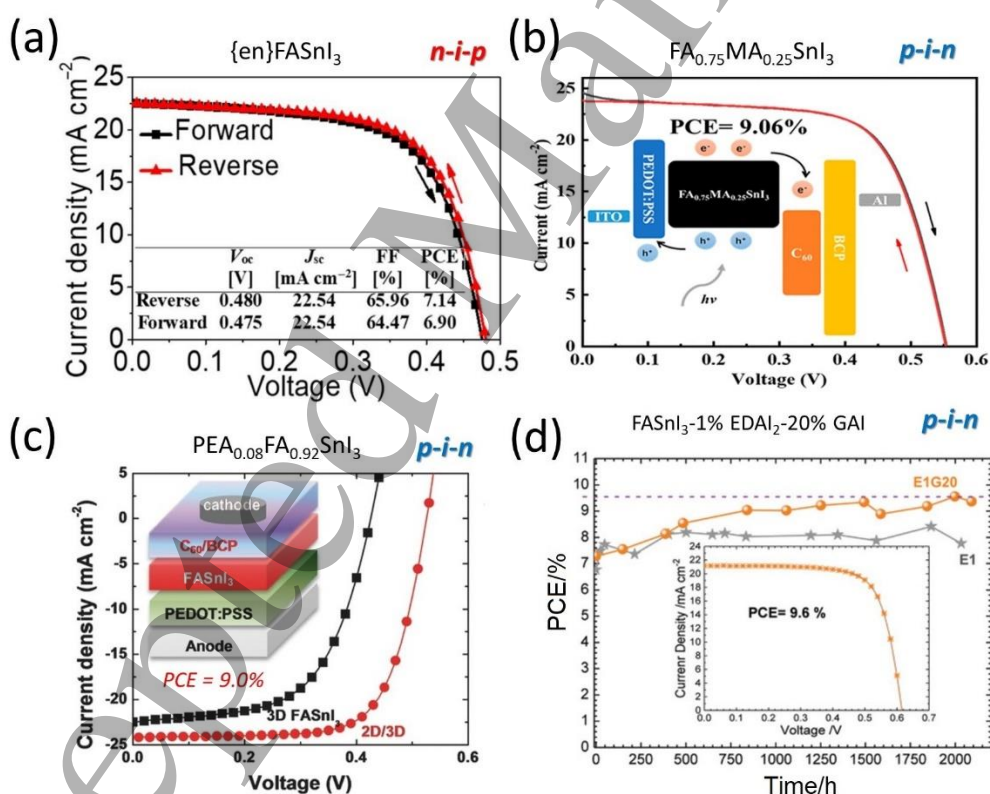


**Figure 6.** J-V curves of the-state-of-the-art pure Sn-base PSCs, including (a) n-i-p (en)FASnI<sub>3</sub>, (b) p-i-n FA<sub>0.75</sub>MA<sub>0.25</sub>SnI<sub>3</sub>, (c) p-i-n PEA<sub>0.08</sub>FA<sub>0.92</sub>SnI<sub>3</sub>, and (d) p-i-n FASnI<sub>3</sub>-1% EDAl<sub>2</sub>-20% GAI. Panel (a) is reprinted with permission from [83], copyright 2017 American Association for the Advancement of Science. Panel (b) is reprinted with permission from [84], copyright 2018 American Chemical Society. Panel (c) is reprinted with permission from [85], copyright 2018 WILEY-VCH. Panel (d) is reprinted with permission from [89], copyright 2018 WILEY-VCH.

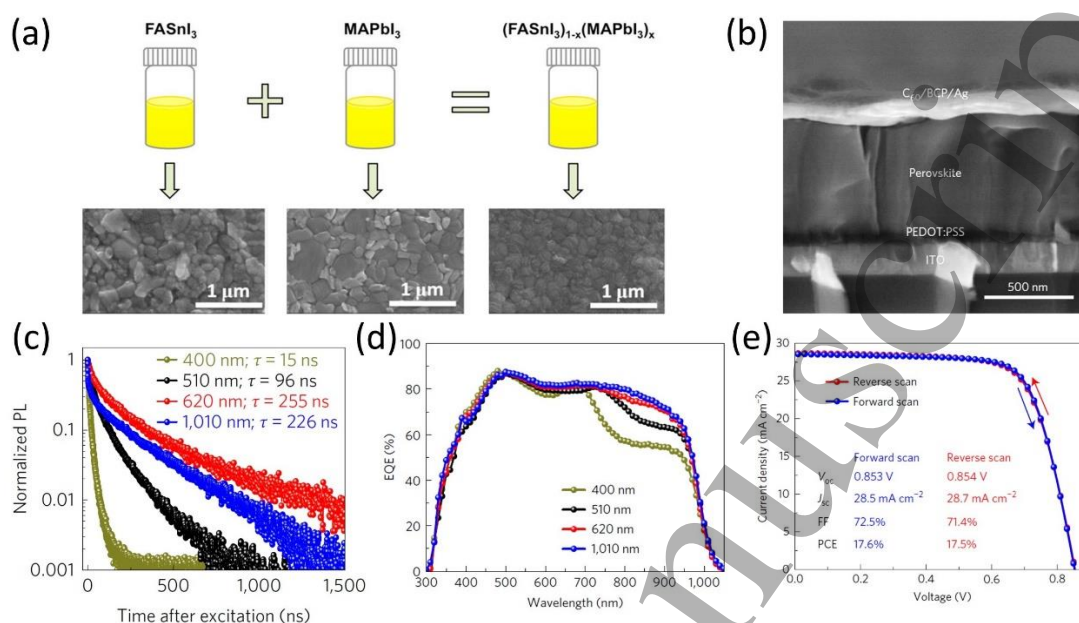


**Figure 7.** Low- $E_g$  PSCs based on  $(\text{FASnI}_3)_{0.6}(\text{MAPbI}_3)_{0.4}$ . (a) Schematics and SEM images of  $\text{FASnI}_3$ ,  $\text{MAPbI}_3$ , and the mixed  $(\text{FASnI}_3)_{1-x}(\text{MAPbI}_3)_x$ . Reprinted with permission from [96], copyright 2016 American Chemical Society. (b) SEM cross-sectional image of a  $(\text{FASnI}_3)_{0.6}(\text{MAPbI}_3)_{0.4}$  PSC. (c) PL decays of  $(\text{FASnI}_3)_{0.6}(\text{MAPbI}_3)_{0.4}$  films with various thicknesses. (d) EQE of  $(\text{FASnI}_3)_{0.6}(\text{MAPbI}_3)_{0.4}$  PSCs with various absorber layer thicknesses. (e) J-V curves of the best performing  $(\text{FASnI}_3)_{0.6}(\text{MAPbI}_3)_{0.4}$  PSC. Panel (b)-(e) are reprinted with permission from [97], copyright 2018 Springer Nature.

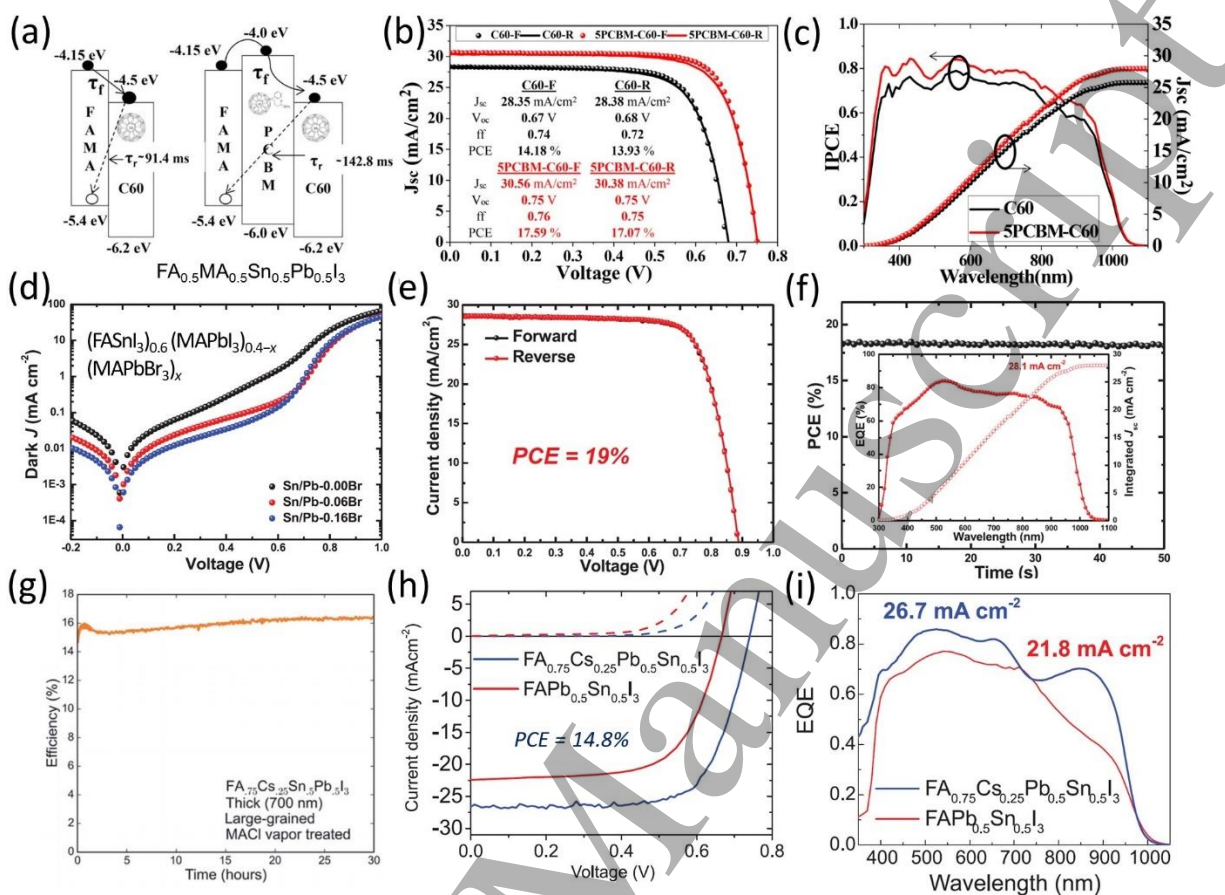


**Figure 8.** Low-E<sub>g</sub> PSCs based on (FASnI<sub>3</sub>)<sub>0.6</sub>(MAPbI<sub>3</sub>)<sub>0.4</sub>. (a) Schematics showing charge recombination at the perovskite/HSLs interfaces. (b) J-V curves and (c) EQE curves with integrated J<sub>sc</sub> of FA<sub>0.5</sub>MA<sub>0.5</sub>Sn<sub>0.5</sub>Pb<sub>0.5</sub>I<sub>3</sub> PSCs with C<sub>60</sub> and PCBM/C<sub>60</sub> HSLs. Panel (a)-(c) are reprinted with permission from [99], copyright 2018 American Chemical Society. (d) dark J-V curves of (FASnI<sub>3</sub>)<sub>0.6</sub>(MAPbI<sub>3</sub>)<sub>0.4-x</sub>(MAPbBr<sub>3</sub>)<sub>x</sub> PSCs with different Br contents. (e) J-V curves and (f) steady-state output with EQE curve in the inset of the best performing (FASnI<sub>3</sub>)<sub>0.6</sub>(MAPbI<sub>3</sub>)<sub>0.34</sub>(MAPbBr<sub>3</sub>)<sub>0.06</sub> PSC. Panel (d)-(f) are reprinted with permission from [102], copyright 2018 WILEY-VCH. (g) MPPT of a FA<sub>0.75</sub>Cs<sub>0.25</sub>Sn<sub>0.5</sub>Pb<sub>0.5</sub>I<sub>3</sub> PSC. Reprinted with permission from [104], copyright 2018 Royal Society of Chemistry. (h) J-V curves and (i) EQE of FAPb<sub>0.5</sub>Sn<sub>0.5</sub>I<sub>3</sub> and FA<sub>0.75</sub>Cs<sub>0.25</sub>Pb<sub>0.5</sub>Sn<sub>0.5</sub>I<sub>3</sub> PSCs. Panel (h) and (i) are reprinted with permission from [103], copyright 2016 American Association for the Advancement of Science.



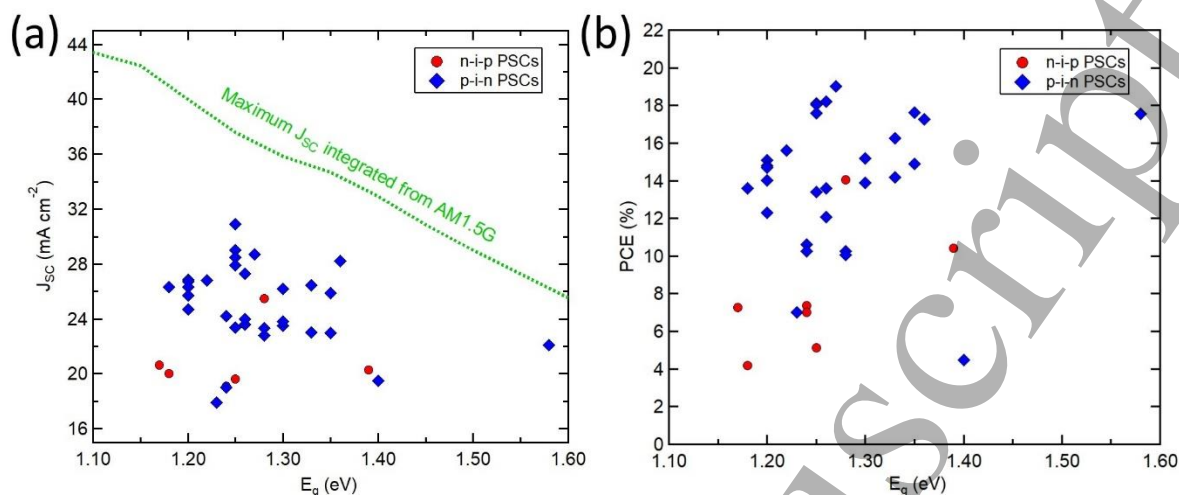


**Figure 9.** Plots of (a)  $J_{sc}$  and (b) PCE versus bandgap of low- $E_g$  PSCs reported in the literature.

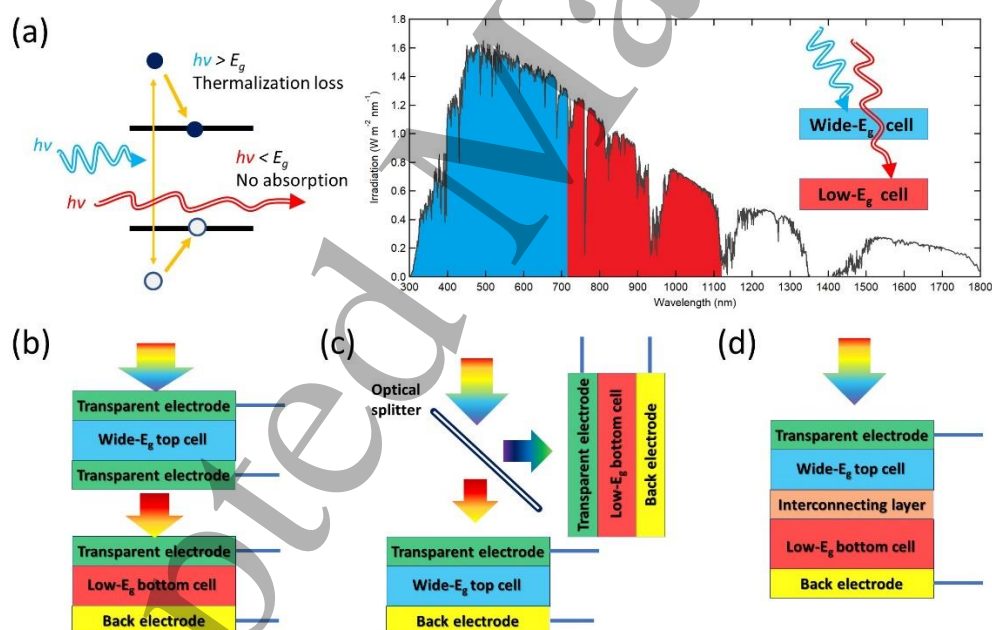


**Figure 10.** (a) Illustration of energy losses of a single-junction solar cells and tandem solar cells working principle.

Schematics of two main double-junction tandem solar cells architectures, including (b) 4-T mechanically stacked, (c) 4-T optical splitting, and (d) 2-T monolithically integrated configurations.

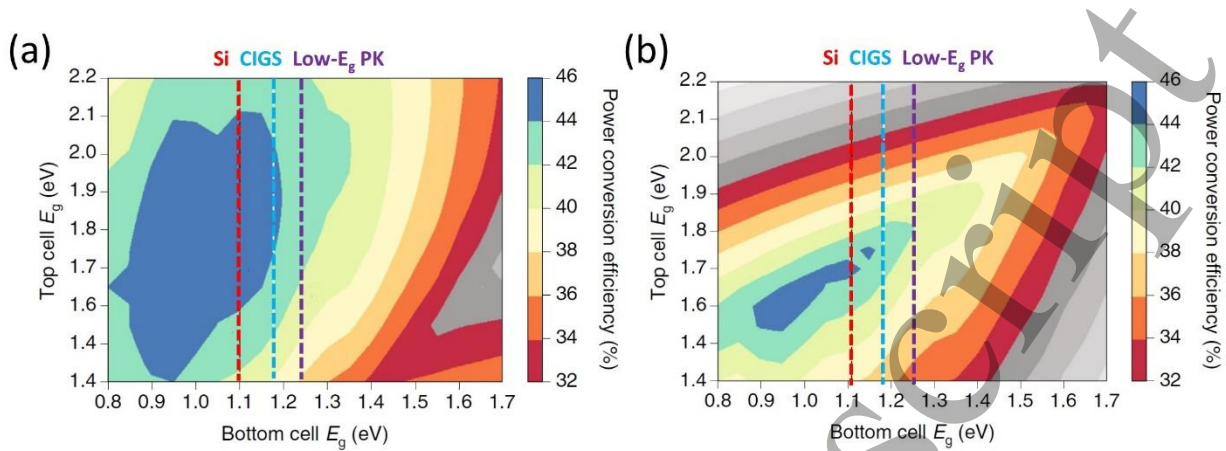


**Figure 11.** Theoretical efficiency limits of (a) 4-T and (b) 2-T tandem solar cells. The dash lines show the bandgaps of Si, CIGS, and low- $E_g$  perovskites. Reprinted with permission from [3], copyright 2018 Springer Nature.

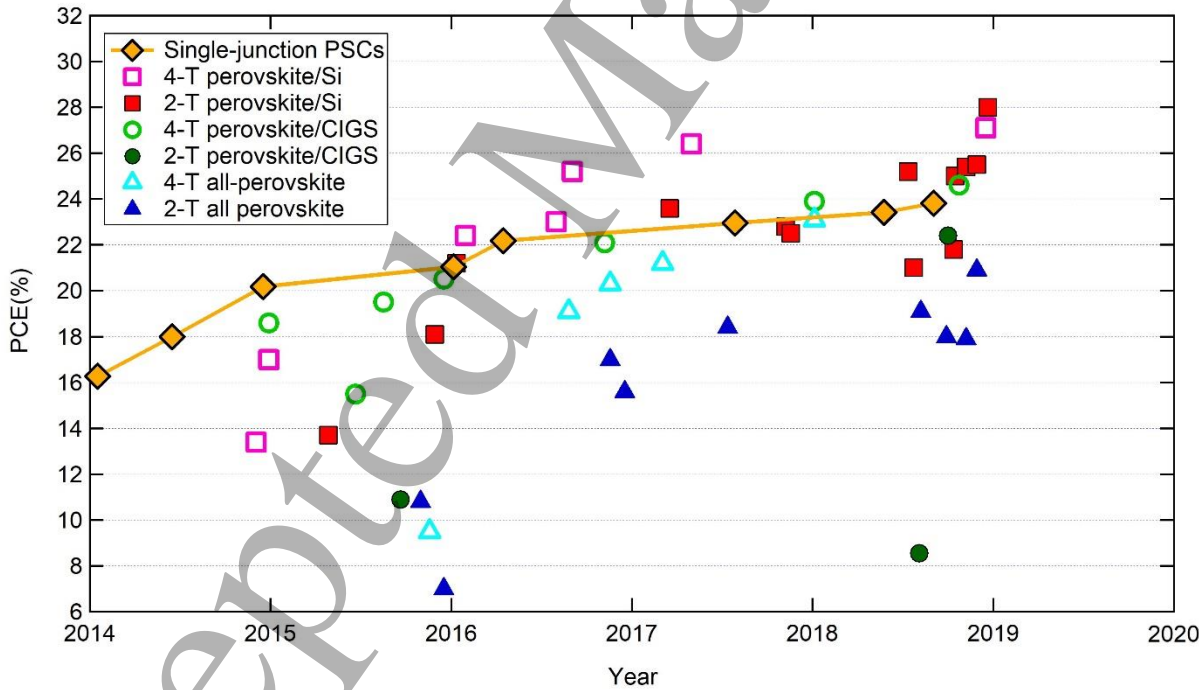


**Figure 12.** Evolution of PCEs of notable single-junction and tandem perovskite solar cells reported in the literature.

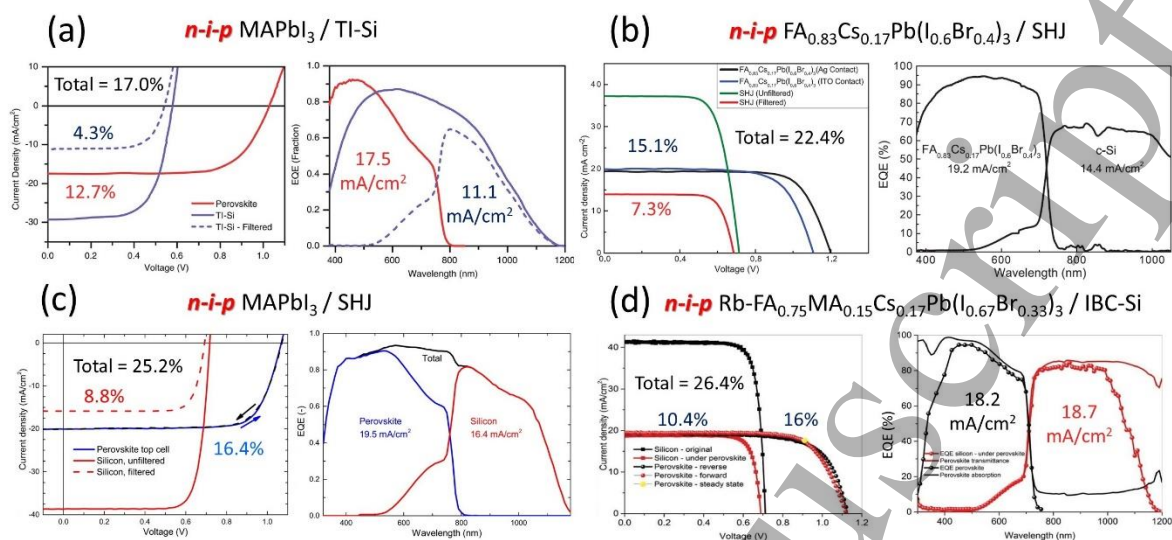


**Figure 13.** J-V and EQE curves of 4-T perovskite/Si tandem solar cells, including (a) MAPbI<sub>3</sub>/TI-Si, (b) FA<sub>0.83</sub>Cs<sub>0.17</sub>Pb(I<sub>0.6</sub>Br<sub>0.4</sub>)<sub>3</sub>/SHJ, (c) MAPbI<sub>3</sub>/SHJ, and (d) Rb-FA<sub>0.75</sub>MA<sub>0.15</sub>Cs<sub>0.1</sub>Pb(I<sub>0.67</sub>Br<sub>0.33</sub>)<sub>3</sub>/IBC-Si. Panel (a) is reprinted with permission from [122], copyright 2015 Royal Society of Chemistry. Panel (b) is reprinted with permission from [41], copyright 2016 American Association for the Advancement of Science. Panel (c) is reprinted with permission from [124], copyright 2016 American Chemical Society. Panel (d) is reprinted with permission from [46], copyright 2017 WILEY-VCH.

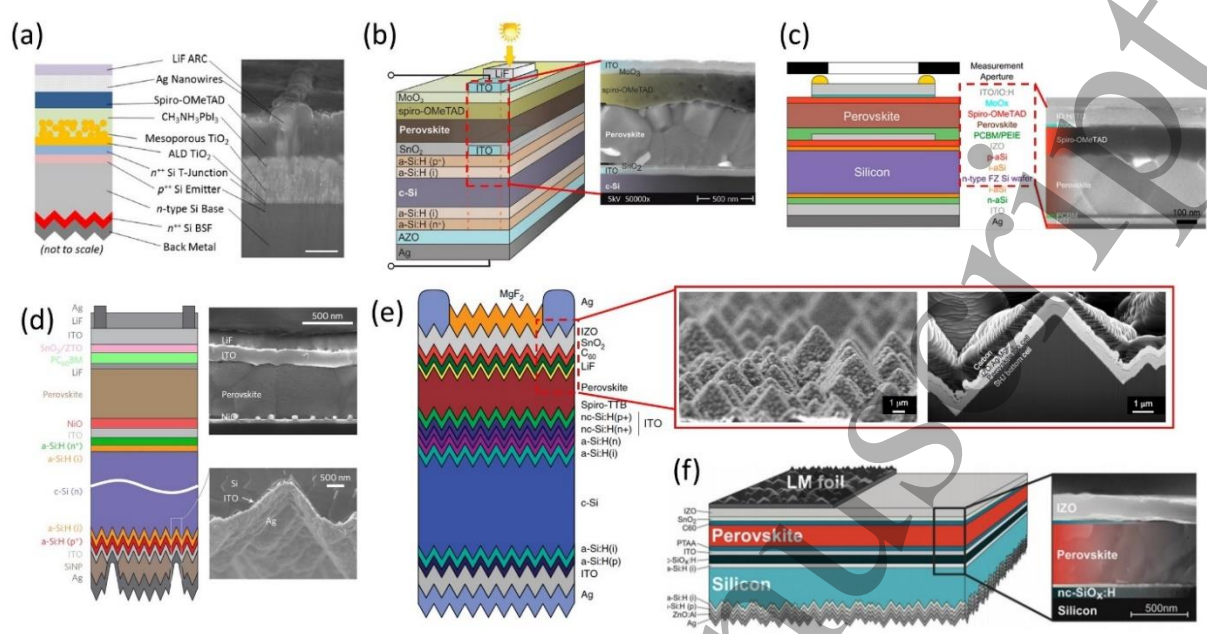


**Figure 14.** Designs and cross-sectional SEM images of 2-T monolithic perovskite/Si tandem solar cells, including (a) MAPbI<sub>3</sub>/c-Si, (b) FA<sub>0.83</sub>MA<sub>0.17</sub>PbI<sub>0.85</sub>Br<sub>0.15</sub>/SHJ (double-side polished), (c), MAPbI<sub>3</sub>/SHJ (double-side polished), (d) FA<sub>0.83</sub>Cs<sub>0.17</sub>Pb(I<sub>0.83</sub>Br<sub>0.17</sub>)<sub>3</sub>/SHJ (single-side textured), (e) (FA,Cs)Pb(I,Br)<sub>3</sub>/SHJ (fully textured) and (f) Cs<sub>0.05</sub>(MA<sub>0.17</sub>FA<sub>0.83</sub>)<sub>0.95</sub>Pb(I<sub>0.83</sub>Br<sub>0.17</sub>)<sub>3</sub>/SHJ (single-side textured). Panel (a) is reprinted with permission from [126], copyright 2015 American Institute of Physics. Panel (b) is reprinted with permission from [127], copyright 2016 Royal Society of Chemistry. Panel (c) is reprinted with permission from [128], copyright 2016 American Chemical Society. Panel (d) is reprinted with permission from [131], copyright 2017 Springer Nature. Panel (e) is reprinted with permission from [134], copyright 2018 Springer Nature. Panel (f) is reprinted with permission from [137], copyright 2018 Royal Society of Chemistry.



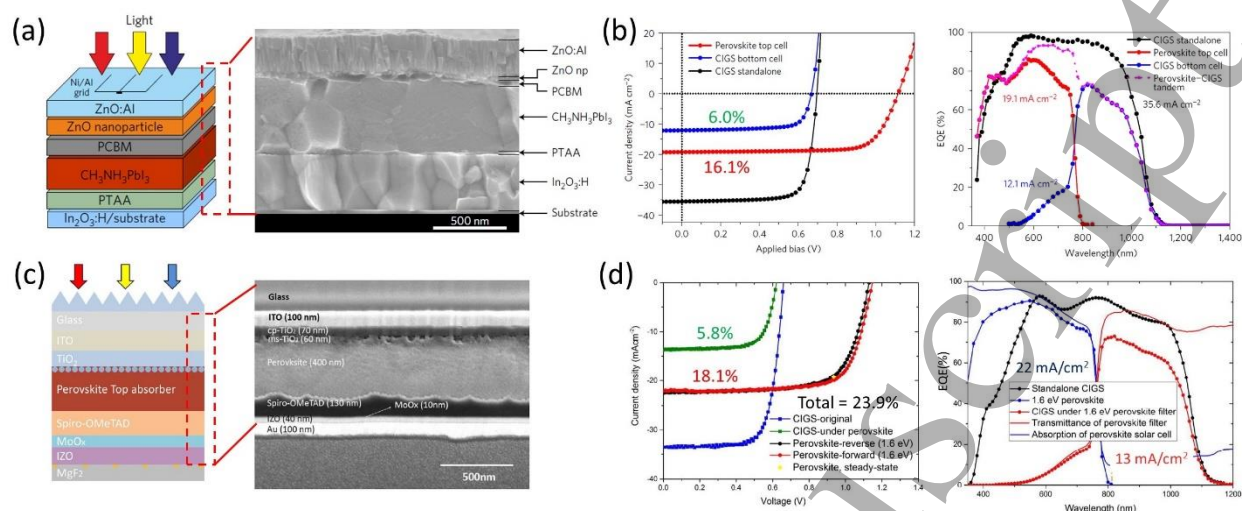


**Figure 15.** (a) Design and cross-sectional SEM image of a semitransparent substrate-type MAPbI<sub>3</sub> PSC. (b) J-V and EQE curves of 4-T MAPbI<sub>3</sub>/CIGS tandem solar cells. Panels (a) and (b) are reprinted with permission from [146], copyright 2016 Springer Nature. (c) Design and cross-sectional SEM image of a semitransparent n-i-p Cs<sub>0.05</sub>Rb<sub>0.05</sub>FA<sub>0.765</sub>MA<sub>0.135</sub>Pb(I<sub>0.85</sub>Br<sub>0.15</sub>)<sub>3</sub> PSC. (d) J-V and EQE curves of 4-T Cs<sub>0.05</sub>Rb<sub>0.05</sub>FA<sub>0.765</sub>MA<sub>0.135</sub>Pb(I<sub>0.85</sub>Br<sub>0.15</sub>)<sub>3</sub>/CIGS tandem solar cells. Panels (a) and (b) are reprinted with permission from [147], copyright 2018 Royal Society of Chemistry.

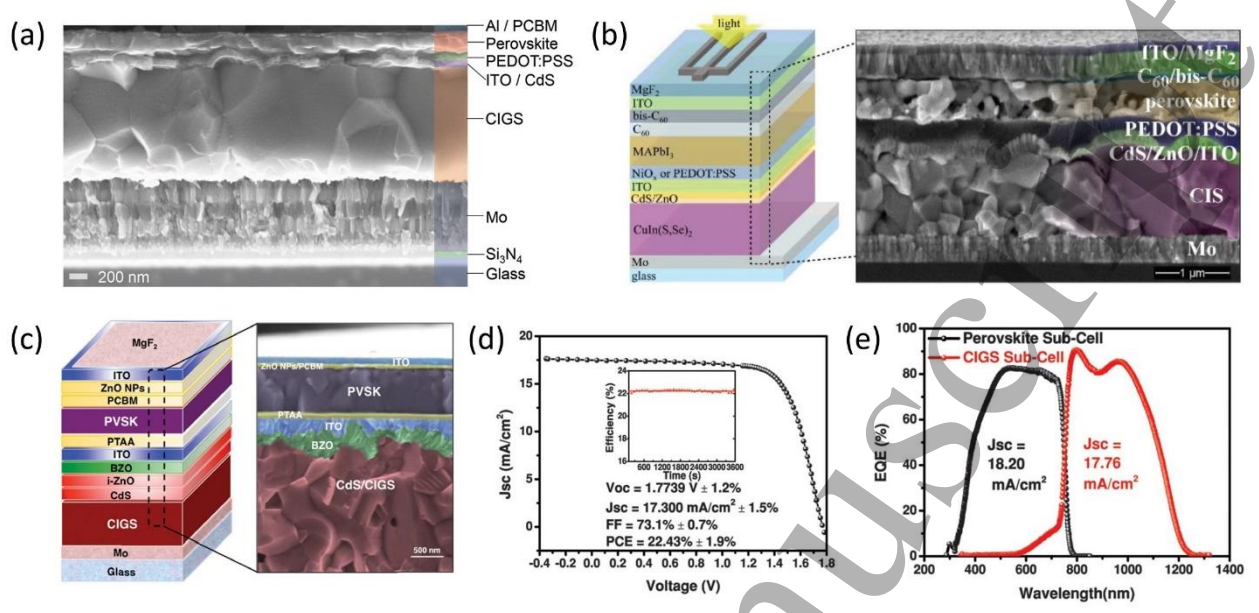


**Figure 16.** (a) Cross-sectional SEM image of a monolithic 2-T perovskite/CIGS tandem solar cell with CIGS layer being prepared by a hydrazine-based method. Reprinted with permission from [149], copyright 2015 WILEY-VCH. (b) Design and cross-sectional SEM image of a monolithic 2-T perovskite/CIGS tandem solar cell with CIGS layer being prepared by a molecular-ink deposition route. Reprinted with permission from [150], copyright 2018 WILEY-VCH. (c) Design and cross-sectional SEM image, (d) J-V and (e) EQE curves of a monolithic 2-T perovskite/CIGS tandem solar cell showing a PCE of 22.4%. Reprinted with permission from [142], copyright 2018 American Association for the Advancement of Science.

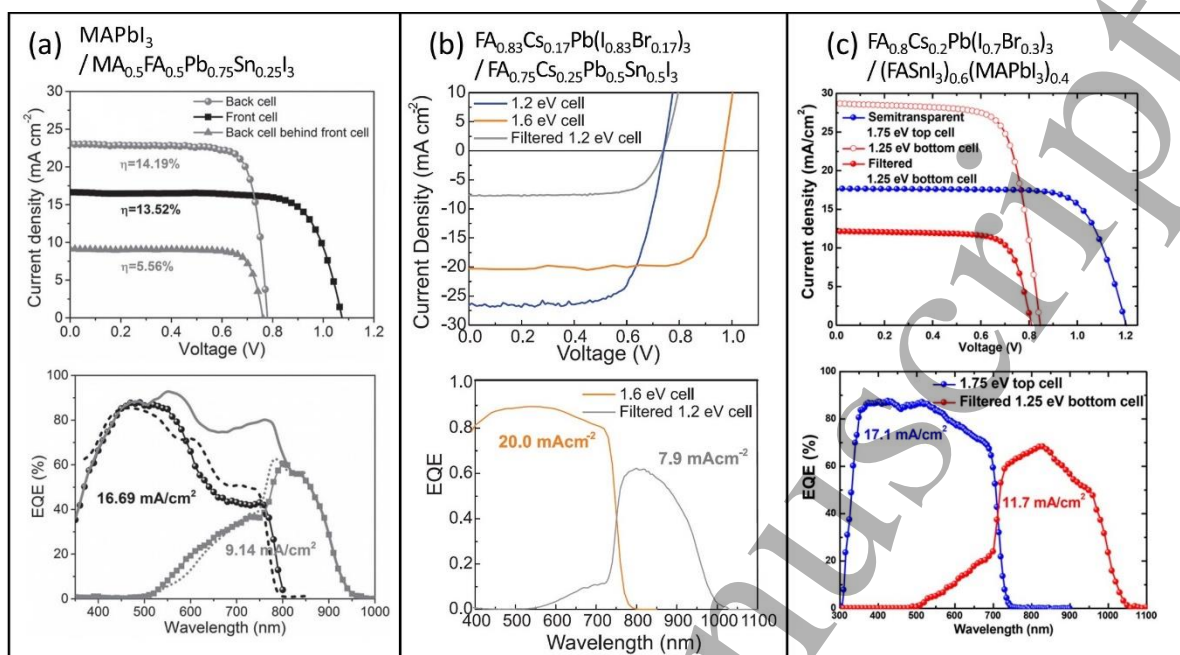


**Figure 17.** J-V and EQE curves of 4-T all-perovskite tandem solar cells, including (a) MAPbI<sub>3</sub>/MA<sub>0.5</sub>FA<sub>0.5</sub>Pb<sub>0.75</sub>Sn<sub>0.25</sub>I<sub>3</sub>, (b) FA<sub>0.83</sub>Cs<sub>0.17</sub>Pb(I<sub>0.83</sub>Br<sub>0.17</sub>)<sub>3</sub>/FA<sub>0.75</sub>Cs<sub>0.25</sub>Pb<sub>0.5</sub>Sn<sub>0.5</sub>I<sub>3</sub>, and (c) FA<sub>0.8</sub>Cs<sub>0.2</sub>Pb(I<sub>0.7</sub>Br<sub>0.3</sub>)<sub>3</sub>/(FASnI<sub>3</sub>)<sub>0.6</sub>(MAPbI<sub>3</sub>)<sub>0.4</sub>. Panel (a) is reprinted with permission from [95], copyright 2016 WILEY-VCH. Panel (b) is reprinted with permission from [103], copyright 2016 American Association for the Advancement of Science. Panel (c) is reprinted with permission from [154], copyright 2018 American Chemical Society.

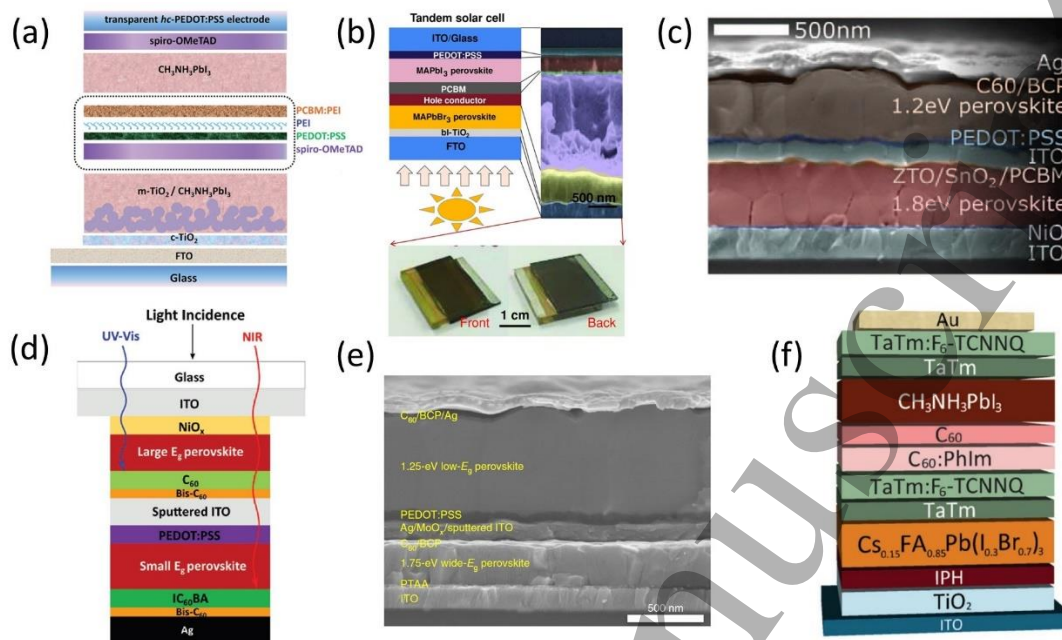


**Figure 18.** Device structure schematics and cross-sectional SEM images of all-perovskite tandem solar cells, including (a)  $\text{MAPbI}_3/\text{MAPbI}_3$ , (b)  $\text{MAPbBr}_3/\text{MAPbI}_3$ , (c)  $\text{FA}_{0.83}\text{Cs}_{0.17}\text{Pb}(\text{I}_{0.5}\text{Br}_{0.5})_3/\text{FA}_{0.75}\text{Cs}_{0.25}\text{Sn}_{0.5}\text{Pb}_{0.5}\text{I}_3$ , (d)  $\text{MA}_{0.9}\text{Cs}_{0.1}\text{Pb}(\text{I}_{0.6}\text{Br}_{0.4})_3/\text{MASn}_{0.5}\text{Pb}_{0.5}\text{I}_3$ , (e)  $\text{FA}_{0.8}\text{Cs}_{0.2}\text{Pb}(\text{I}_{0.7}\text{Br}_{0.3})_3/(\text{FASnI}_3)_{0.6}(\text{MAPbI}_3)_{0.4}$ , and (f)  $\text{FA}_{0.75}\text{Cs}_{0.15}\text{Pb}(\text{I}_{0.3}\text{Br}_{0.7})_3/\text{MAPbI}_3$ . Panel (a) is reprinted with permission from [156], copyright 2016 Royal Society of Chemistry. Panel (b) is reprinted with permission from [157], copyright 2015 WILEY-VCH. Panel (c) is reprinted with permission from [103], copyright 2016 American Association for the Advancement of Science. Panel (d) is reprinted with permission from [158], copyright 2017 WILEY-VCH. Panel (e) is reprinted with permission from [101], copyright 2018 Springer Nature. Panel (f) is reprinted with permission from [160], copyright 2017 WILEY-VCH.



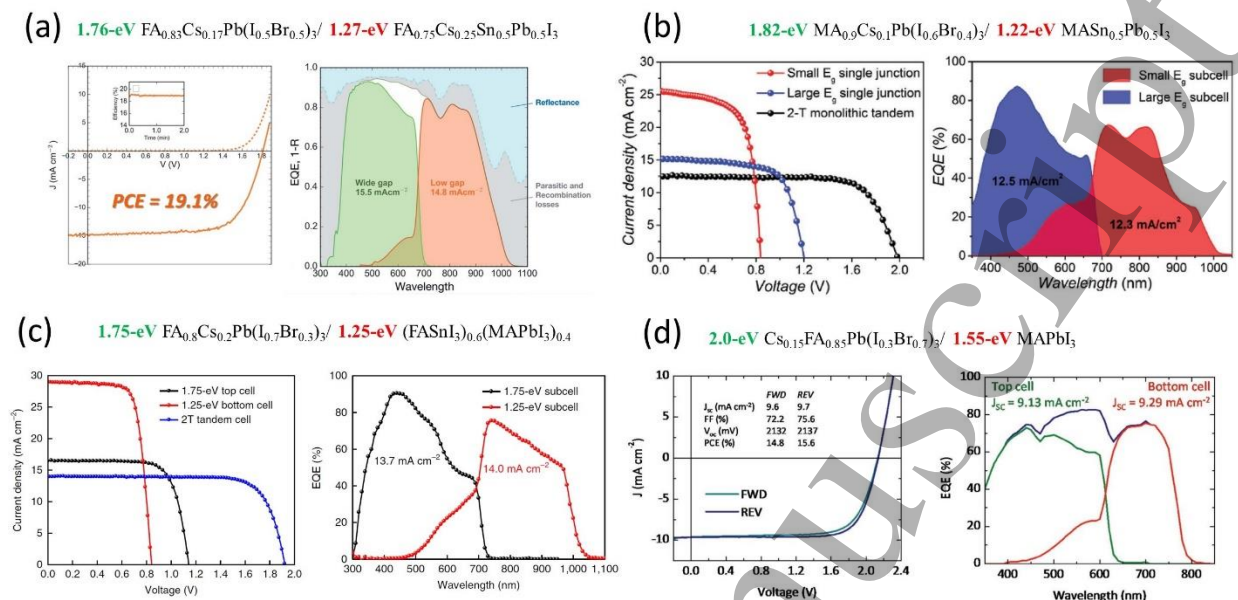


**Figure 19.** J-V and EQE curves of 2-T monolithic all-perovskite tandem solar cells, including (a)  $\text{FA}_{0.83}\text{Cs}_{0.17}\text{Pb}(\text{I}_{0.5}\text{Br}_{0.5})_3/\text{FA}_{0.75}\text{Cs}_{0.25}\text{Sn}_{0.5}\text{Pb}_{0.5}\text{I}_3$ , (b)  $\text{MA}_{0.9}\text{Cs}_{0.1}\text{Pb}(\text{I}_{0.6}\text{Br}_{0.4})_3/\text{MASn}_{0.5}\text{Pb}_{0.5}\text{I}_3$ , (c)  $\text{FA}_{0.8}\text{Cs}_{0.2}\text{Pb}(\text{I}_{0.7}\text{Br}_{0.3})_3/(\text{FASnI}_3)_{0.6}(\text{MAPbI}_3)_{0.4}$ , and (d)  $\text{FA}_{0.75}\text{Cs}_{0.15}\text{Pb}(\text{I}_{0.3}\text{Br}_{0.7})_3/\text{MAPbI}_3$ . Panel (a) is reprinted with permission from [104], copyright 2018 Royal Society of Chemistry. Panel (b) is reprinted with permission from [158], copyright 2017 WILEY-VCH. Panel (c) is reprinted with permission from [101], copyright 2018 Springer Nature. Panel (d) is reprinted with permission from [160], copyright 2017 WILEY-VCH.

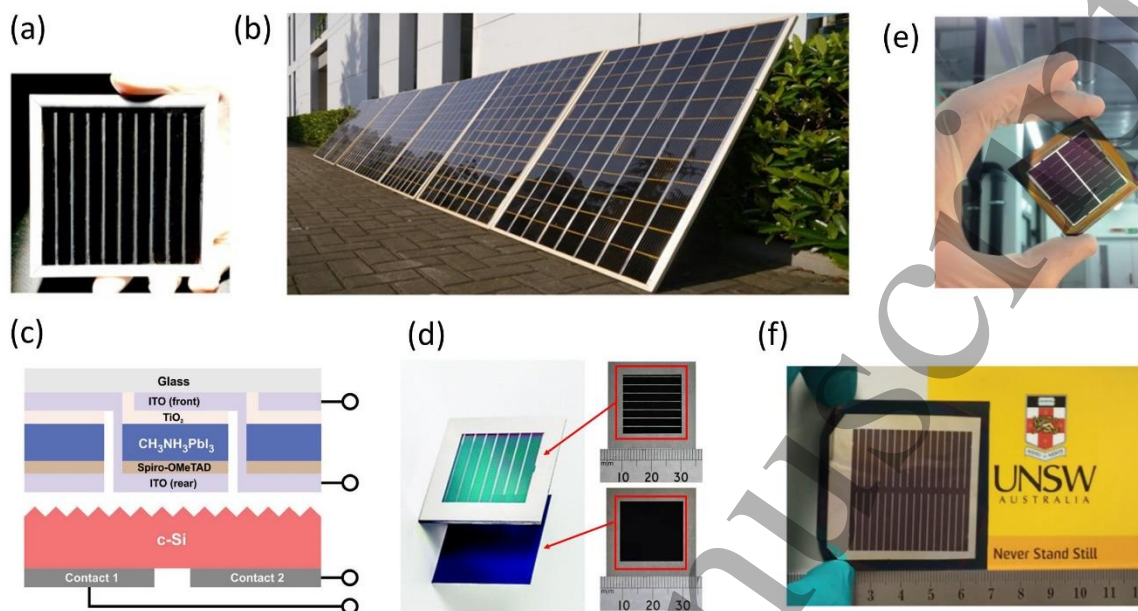


**Figure 20.** Photos of (a) 100 cm<sup>2</sup> printed single-junction perovskite solar modules and (b) 9 m<sup>2</sup> solar panels assembled using the printed perovskite modules. Reprinted with permission from [166], copyright 2017 WILEY-VCH. (c) Schematic design and (d) photos of 4-T perovskite/Si tandem solar cells with an area of 4 cm<sup>2</sup>. Panel (c) is reprinted with permission from [167], copyright 2017 WILEY-VCH. Panel (d) is reprinted with permission from [168], copyright 2018 Royal Society of Chemistry. (e) Photo of a 12.96 cm<sup>2</sup> 2-T perovskite/SHJ tandem solar cell. Reprinted with permission from [130], copyright 2017 WILEY-VCH. (f) Photo of a 16 cm<sup>2</sup> 2-T perovskite/homojunction Si tandem solar cell. Reprinted with permission from [140], copyright 2018 American Chemical Society.

**Table 1.** Summary of wide- $E_g$  single-junction perovskite solar cells reported in 2016-2018.

Year	Type	Absorber	$E_g$ (eV)	$V_{OC}$ (V)	$J_{sc}$ (mA/cm <sup>2</sup> )	FF (%)	PCE (%)	Ref.
2016	n-i-p	CsPbBr <sub>3</sub>	2.3	1.24	7.4	73	6.7	[179]
2016	n-i-p	FAPbBr <sub>3</sub>	2.26	1.53	7.3	71	8.2	[180]
2016	n-i-p	MAPbI <sub>2</sub> Br	1.77	1.08	15.3	64.7	10.7	[181]
2016	n-i-p	Cs <sub>0.15</sub> FA <sub>0.85</sub> Pb(I <sub>0.3</sub> Br <sub>0.7</sub> ) <sub>3</sub>	2	1.215	11.41	81.2	10.7	[160]
2016	n-i-p	CsPbI <sub>3</sub> QDs	1.75	1.23	13.47	65	10.77	[182]
2016	n-i-p	MAPbI <sub>2.1</sub> Br <sub>0.9</sub>	1.75	1.01	18.19	69	12.67	[183]
2016	n-i-p	FA <sub>0.83</sub> Cs <sub>0.17</sub> Pb(I <sub>0.6</sub> Br <sub>0.4</sub> ) <sub>3</sub>	1.74	1.2	19.4	75.1	17.1	[41]
2016	p-i-n	MAPbBr <sub>3</sub>	2.3	1.5	5.13	69.5	5.35	[184]
2016	p-i-n	CsPbBrI <sub>2</sub>	1.9	1.12	10.9	54.8	6.69	[185]
2016	p-i-n	FA <sub>0.83</sub> Cs <sub>0.17</sub> Pb(I <sub>0.5</sub> Br <sub>0.5</sub> ) <sub>3</sub>	1.8	1.12	15.1	58	9.8	[103]
2016	p-i-n	MAPb <sub>0.75</sub> Sn <sub>0.25</sub> (I <sub>0.4</sub> Br <sub>0.6</sub> ) <sub>3</sub>	1.73	1.04	15.83	77	12.59	[66]
2016	p-i-n	MAPbBr <sub>0.8</sub> I <sub>2.2</sub>	1.75	1.21	15.8	77.9	14.9	[44]
2016	p-i-n	MA <sub>0.7</sub> FA <sub>0.3</sub> Pb(I <sub>0.8</sub> Br <sub>0.2</sub> ) <sub>2</sub>	1.69	1.11	17.34	78	15.01	[186]
2017	n-i-p	MAPbBr <sub>3</sub>	2.3	1.41	6.16	64	5.2	[187]
2017	n-i-p	Cs <sub>0.925</sub> K <sub>0.075</sub> PbI <sub>2</sub> Br	1.92	1.18	11.6	73	10	[188]
2017	n-i-p	CsPb <sub>0.9</sub> Sn <sub>0.1</sub> I <sub>2</sub> Br	1.79	1.26	14.3	63	11.33	[189]
2017	n-i-p	Cs <sub>0.15</sub> FA <sub>0.85</sub> Pb(I <sub>0.3</sub> Br <sub>0.7</sub> ) <sub>3</sub>	2	1.18	12.32	79	11.5	[190]
2017	n-i-p	Rb <sub>0.05</sub> (FA <sub>0.75</sub> MA <sub>0.15</sub> Cs <sub>0.1</sub> ) <sub>0.95</sub> PbI <sub>2</sub> Br	1.73	1.12	19.4	73	15.9	[46]
2017	n-i-p	FA <sub>0.83</sub> Cs <sub>0.17</sub> Pb(I <sub>0.6</sub> Br <sub>0.4</sub> ) <sub>3</sub>	1.75	1.157	18.27	78.5	16.28	[191]
2017	n-i-p	BA <sub>0.09</sub> (FA <sub>0.83</sub> Cs <sub>0.17</sub> ) <sub>0.91</sub> Pb(I <sub>0.6</sub> Br <sub>0.4</sub> ) <sub>3</sub>	1.72	1.18	19.8	73	17.2	[192]
2017	n-i-p	FA <sub>0.85</sub> Cs <sub>0.15</sub> Pb(I <sub>0.73</sub> Br <sub>0.27</sub> ) <sub>3</sub>	1.72	1.24	19.83	73.7	18.13	[49]
2017	n-i-p	FA <sub>0.8</sub> Cs <sub>0.2</sub> Pb(I <sub>0.7</sub> Br <sub>0.3</sub> ) <sub>3</sub>	1.75	1.25	18.53	79	18.27	[47]
2017	p-i-n	CsPbI <sub>3</sub>	1.72	1.08	14.9	70	11.4	[193]
2017	p-i-n	MA <sub>0.9</sub> Cs <sub>0.1</sub> Pb(I <sub>0.6</sub> Br <sub>0.4</sub> ) <sub>3</sub>	1.82	1.2	15.1	69	12.5	[158]
2017	p-i-n	MA <sub>0.6</sub> FA <sub>0.4</sub> Pb(I <sub>0.6</sub> Br <sub>0.4</sub> ) <sub>3</sub>	1.75	1.17	16	78.6	14.7	[51]
2017	p-i-n	(FA <sub>0.83</sub> MA <sub>0.17</sub> ) <sub>0.95</sub> Cs <sub>0.05</sub> Pb(I <sub>0.6</sub> Br <sub>0.4</sub> ) <sub>3</sub>	1.71	1.21	19.7	77.5	18.5	[50]
2018	n-i-p	CsPbBr <sub>3</sub>	2.3	1.45	7.47	77.7	8.42	[194]

2018	n-i-p	MAPbBr <sub>3</sub>	2.3	1.47	8.1	76	8.9	[195]
2018	n-i-p	CsPb <sub>0.75</sub> Sn <sub>0.25</sub> IBr <sub>2</sub>	1.78	1.21	12.57	75.8	11.53	[196]
2018	n-i-p	CsPbBrI <sub>2</sub>	1.91	1.19	12.93	80.5	12.39	[197]
2018	n-i-p	Cs <sub>0.15</sub> FA <sub>0.85</sub> Pb(I <sub>0.71</sub> Br <sub>0.29</sub> ) <sub>3</sub>	1.72	1.22	15.4	73.4	13.8	[125]
2018	n-i-p	CsPbI <sub>2</sub> Br QDs	1.91	1.204	15.25	78.7	14.45	[198]
2018	n-i-p	MAPb(Br <sub>0.2</sub> I <sub>0.8</sub> ) <sub>3</sub>	1.72	1.119	17.3	82.3	15.9	[67]
2018	n-i-p	K <sub>0.1</sub> (Cs <sub>0.06</sub> FA <sub>0.79</sub> MA <sub>0.15</sub> ) <sub>0.9</sub> Pb(I <sub>0.4</sub> Br <sub>0.6</sub> ) <sub>3</sub>	1.78	1.23	17.9	79	17.5	[67]
2018	n-i-p	FA <sub>0.83</sub> Cs <sub>0.17</sub> Pb(I <sub>0.6</sub> Br <sub>0.4</sub> ) <sub>3</sub>	1.75	1.23	18.34	79	17.8	[52]
2018	n-i-p	Cs <sub>0.17</sub> FA <sub>0.83</sub> PbI <sub>2.2</sub> Br <sub>0.8</sub>	1.72	1.244	19.3	77.4	18.6	[48]
2018	n-i-p	Cs <sub>0.12</sub> MA <sub>0.05</sub> FA <sub>0.83</sub> Pb(I <sub>0.6</sub> Br <sub>0.4</sub> ) <sub>3</sub>	1.74	1.25	19	81.5	19.1	[53]
2018	p-i-n	PEA <sub>0.05</sub> MA <sub>0.95</sub> Pb(I <sub>0.6</sub> Br <sub>0.4</sub> ) <sub>3</sub>	1.82	1.3	14	67	12.2	[72]
2018	p-i-n	CsPbI <sub>2</sub> Br	1.92	1.14	15.2	77	13.3	[199]
2018	p-i-n	(FA <sub>0.58</sub> GA <sub>0.10</sub> Cs <sub>0.32</sub> )Pb(I <sub>0.73</sub> Br <sub>0.27</sub> ) <sub>3</sub>	1.75	1.22	16.3	73.2	14.6	[70]
2018	p-i-n	FA <sub>0.6</sub> Cs <sub>0.4</sub> Pb(I <sub>0.7</sub> Br <sub>0.3</sub> ) <sub>3</sub>	1.75	1.17	17.5	80	16.3	[65]
2018	p-i-n	MAPbI <sub>3-x</sub> Br <sub>x</sub>	1.71	1.24	17.45	77	16.74	[200]

**Table 2.** Summary of low- $E_g$  single-junction perovskite solar cells reported in 2016-2018.

Year	Type	Absorber	$E_g$ (eV)	$V_{OC}$ (V)	$J_{sc}$ (mA/cm <sup>2</sup> )	FF (%)	PCE (%)	Ref.
2016	n-i-p	$MA_{0.75}Pb_{0.25}I_{3-x}Cl_x$	1.25	0.457	19.63	57.2	5.13	[201]
2016	p-i-n	$MA_{0.9}Cs_{0.1}Pb_{0.5}Sn_{0.5}I_3$	1.28	0.7	23.32	61.7	10.07	[202]
2016	p-i-n	$MA_{0.5}Pb_{0.5}I_3$	1.28	0.69	22.8	65	10.24	[203]
2016	p-i-n	$MA_{0.1}Pb_{0.9}I_3$	1.31	0.78	19	67.1	10.25	[204]
2016	p-i-n	$MA_{0.5}Pb_{0.5}I_3$	1.18	0.75	26.3	68.8	13.6	[92]
2016	p-i-n	$MAPb_{0.75}Sn_{0.25}I_3$	1.3	0.745	23.8	78.6	13.9	[205]
2016	p-i-n	$MA_{0.5}FA_{0.5}Pb_{0.75}Sn_{0.25}I_3$	1.33	0.78	23.03	79	14.19	[95]
2016	p-i-n	$FA_{0.75}Cs_{0.25}Sn_{0.5}Pb_{0.5}I_3$	1.2	0.74	26.7	71	14.8	[103]
2016	p-i-n	$(FASnI_3)_{0.6}(MAPbI_3)_{0.4}$	1.24	0.795	26.86	70.6	15.08	[96]
2017	p-i-n	$MA_{0.25}Pb_{0.75}I_3$	1.26	0.77	24	66	12.08	[206]
2017	p-i-n	$MAPb_{0.75}Sn_{0.25}I_3$	1.3	0.736	23.5	79	13.9	[207]
2017	p-i-n	$MA_{0.5}FA_{0.5}Pb_{0.5}Sn_{0.5}I_3$	1.2	0.78	25.69	70	14.01	[112]
2017	p-i-n	$MA_{0.25}Pb_{0.75}I_3$	1.3	0.8	26.2	72.5	15.2	[208]
2017	p-i-n	$MAPb_{0.5}Sn_{0.5}I_3$	1.22	0.89	26.8	71	15.61	[93]
2017	p-i-n	$(FASnI_3)_{0.6}(MAPbI_3)_{0.4}$	1.25	0.853	28.5	72.5	17.6	[97]
2017	p-i-n	$MAPb_{0.5}Sn_{0.5}(I_{0.8}Br_{0.2})_3$	1.35	0.9	25.9	75	17.63	[94]
2017	p-i-n	$(FASnI_3)_{0.6}(MAPbI_3)_{0.4}$	1.24	0.83	27.3	78.5	17.8	[98]
2018	n-i-p	$MA_{0.74}Pb_{0.26}I_3$	1.28	0.796	25.5	69	14.04	[209]
2018	p-i-n	$(t-BA)_2(FA_{0.85}Cs_{0.15})_4(Pb_{0.6}Sn_{0.4})_nI_{16}$	1.24	0.7	24.2	63	10.6	[210]
2018	p-i-n	$MA_{0.5}Pb_{0.5}I_{3-x}Cl_x$	1.2	0.7	24.7	71	12.3	[211]
2018	p-i-n	$MAPb_{0.4}Sn_{0.6}I_{2.6}Br_{0.4}$	1.25	0.8	23.38	72	13.4	[212]
2018	p-i-n	$FA_{0.7}MA_{0.3}Sn_{0.3}Pb_{0.7}I_3$	1.26	0.782	23.6	78	13.6	[213]
2018	p-i-n	$(FAPbI_3)_{0.7}(CsSnI_3)_{0.3}$	1.3	0.7	26.3	79.7	14.7	[106]
2018	p-i-n	$FAPb_{0.7}Sn_{0.3}I_3/PEAI$	1.33	0.78	26.46	79	16.26	[214]
2018	p-i-n	$FAPb_{0.75}Sn_{0.25}I_3$	1.36	0.81	28.23	75	17.25	[111]
2018	p-i-n	$FA_{0.5}MA_{0.5}Sn_{0.5}Pb_{0.5}I_3$	1.25	0.75	30.29	0.74	17.6	[99]
2018	p-i-n	$(FASnI_3)_{0.6}(MAPbI_3)_{0.4}$	1.25	0.86	27.92	0.75	18.03	[100]

2018	p-i-n	$(\text{FASnI}_3)_{0.6}(\text{MAPbI}_3)_{0.4-x}(\text{MAPbCl}_3)_x$	1.25	0.84	29	74.5	18.1	[101]
2018	p-i-n	$(\text{FASnI}_3)_{0.6}(\text{MAPbI}_3)_{0.34}(\text{MAPbBr}_3)_{0.06}$	1.27	0.888	28.7	74.6	19.03	[102]
2018	p-i-n	$(\text{FAPb}_{0.6}\text{Sn}_{0.4}\text{I}_3)_{0.85}(\text{MAPb}_{0.6}\text{Sn}_{0.4}\text{Br}_3)_{0.15}$	1.28	0.87	26.45	79.1	18.2	[113]

**Table 3.** Summary of 4-T perovskite tandem solar cells reported in 2015-2018.

Year	Top/Bottom Cells	V <sub>oc</sub> (V)	J <sub>sc</sub> (mA/cm <sup>2</sup> )	FF (%)	PCE (%)	Total PCE (%)	Ref.
2015	MAPbI <sub>3</sub> /c-Si	0.82/0.69	14.5/13.7	51.9/76.7	6.2/7.2	13.4	[121]
2015	MAPbI <sub>3</sub> /TI-Si	1.025/0.547	17.5/11.1	71/70.4	12.7/4.3	17.0	[122]
2015	MAPbI <sub>3</sub> /CIGS	1.025/0.682	17.5/10.9	71/78.8	12.7/5.9	18.6	[122]
2015	MAPbI <sub>3-x</sub> CL <sub>x</sub> /CIGS	1.05/0.56	14.6/10.2	75.1/69.6	11.5/4.0	15.5	[143]
2015	MAPbI <sub>3</sub> /CIGS	1.034/0.661	16.7/14.4	70.3/77.4	12.1/7.4	19.5	[144]
2015	MAPbI <sub>3</sub> /CIGS	1.104/0.667	17.4/12.7	73.6/74.9	14.1/6.3	20.5	[145]
2015	MAPbBr <sub>3</sub> /MAPbI <sub>3</sub>	1.24/1.02	5.75/7.02	61/72	4.3/5.1	9.4	[155]
2016	FA <sub>0.83</sub> Cs <sub>0.17</sub> Pb(I <sub>0.6</sub> Br <sub>0.4</sub> ) <sub>3</sub> /SHJ	1.1/0.69	19.9/13.9	70.7/76.4	15.1/7.3	22.4	[41]
2016	MAPbI <sub>3</sub> /SHJ	1.08/0.679	20.6/12.3	74.1/77.9	16.5/6.5	23.0	[123]
2016	MAPbI <sub>3</sub> /MA <sub>0.5</sub> FA <sub>0.5</sub> Pb <sub>0.75</sub> Sn <sub>0.25</sub> I <sub>3</sub>	1.08/0.76	16.7/9.1	75/80	13.5/5.6	19.1	[95]
2016	MAPbI <sub>3</sub> /SHJ	1.07/0.69	20.1/16	75/79.5	16.4/8.8	25.2	[124]
2016	FA <sub>0.83</sub> Cs <sub>0.17</sub> Pb(I <sub>0.83</sub> Br <sub>0.17</sub> ) <sub>3</sub> /FA <sub>0.75</sub> Cs <sub>0.25</sub> Sn <sub>0.5</sub> Pb <sub>0.5</sub> I <sub>3</sub>	0.97/0.74	20.3/7.9	79/73	15.7/4.4	20.3	[103]
2016	MAPbI <sub>3</sub> /CIGS	1.116/0.669	19.1/12.1	75.4/73.6	16.1/6.0	22.1	[146]
2017	MA <sub>0.7</sub> FA <sub>0.3</sub> PbI <sub>3</sub> / (FASnI <sub>3</sub> ) <sub>0.6</sub> (MAPbI <sub>3</sub> ) <sub>0.4</sub>	1.14/0.8	20.1/4.8	80/76.3	18.3/2.9	21.2	[97]
2017	(RbFAMACs)PbI <sub>2</sub> Br/IBC-Si	1.12/0.69	19.4/18.8	73/80	15.9/10.4	26.4	[46]
2018	Cs <sub>0.05</sub> Rb <sub>0.05</sub> FA <sub>0.765</sub> MA <sub>0.135</sub> PbI <sub>2.55</sub> Br <sub>0.45</sub> /CIGS	1.14/0.62	21.8/13	74/72	18.4/5.6	23.9	[147]
2018	FA <sub>0.8</sub> Cs <sub>0.2</sub> Pb(I <sub>0.7</sub> Br <sub>0.3</sub> ) <sub>3</sub> / (FASnI <sub>3</sub> ) <sub>0.6</sub> (MAPbI <sub>3</sub> ) <sub>0.4</sub>	1.204/0.81	17.6/12.1	74.6/75.3	15.7/7.4	23.1	[154]

**Table 4.** Summary of 2-T perovskite tandem solar cells reported in 2015-2018.

Year	Top/Bottom Cells	V <sub>OC</sub> (V)	J <sub>SC</sub> (mA/cm <sup>2</sup> )	FF (%)	PCE (%)	Ref.
2015	MAPbI <sub>3</sub> /Si	1.58	11.5	75	13.7	[126]
2015	MAPbBr <sub>x</sub> I <sub>3-x</sub> /CIGS	1.45	12.7	56.6	10.9	[149]
2015	MA <sub>0.17</sub> FA <sub>0.83</sub> PbBr <sub>0.5</sub> I <sub>0.25</sub> /Si	1.759	14.0	77.3	19.1	[127]
2015	MAPbI <sub>3</sub> /MAPbI <sub>3</sub>	1.89	6.61	56	7.0	[156]
2015	MAPbBr <sub>3</sub> /MAPbI <sub>3</sub>	2.25	8.3	56	10.4	[157]
2016	MAPbI <sub>3</sub> /SHJ	1.692	15.8	79.9	21.4	[128]
2016	FA <sub>0.83</sub> CS <sub>0.17</sub> Pb(I <sub>0.5</sub> Br <sub>0.5</sub> ) <sub>3</sub> /FA <sub>0.75</sub> CS <sub>0.25</sub> Sn <sub>0.5</sub> Pb <sub>0.5</sub> I <sub>3</sub>	1.76	13.5	56	13.3	[103]
2016	CS <sub>0.15</sub> FA <sub>0.85</sub> Pb(I <sub>0.3</sub> Br <sub>0.7</sub> ) <sub>3</sub> /MAPbI <sub>3</sub>	2.137	9.7	75.6	15.6	[160]
2017	CS <sub>0.17</sub> FA <sub>0.83</sub> Pb(Br <sub>0.17</sub> I <sub>0.83</sub> ) <sub>3</sub> /SHJ	1.65	18.1	79	23.6	[131]
2017	MA <sub>0.9</sub> CS <sub>0.1</sub> Pb(I <sub>0.6</sub> Br <sub>0.4</sub> ) <sub>3</sub> /MAPb <sub>0.5</sub> Sn <sub>0.5</sub> I <sub>3</sub>	1.98	12.7	73	18.4	[158]
2017	CS <sub>0.19</sub> FA <sub>0.81</sub> PbI <sub>3</sub> /SHJ	1.751	16.8	77.5	22.8	[130]
2017	CS <sub>0.07</sub> Rb <sub>0.03</sub> FA <sub>0.765</sub> MA <sub>0.135</sub> PbI <sub>2.55</sub> Br <sub>0.45</sub> /Si	1.75	17.6	73.8	22.8	[138]
2018	Cs <sub>x</sub> FA <sub>1-x</sub> Pb(I,Br) <sub>3</sub> /textured Si	1.788	19.5	73.1	25.5	[134]
2018	MAPbI <sub>3</sub> /homo-junction Si	1.676	16.1	78	21.0	[139]
2018	MAPbI <sub>3</sub> /CuIn(S,Se) <sub>2</sub>	1.40	14.5	42.1	8.5	[150]
2018	FA <sub>0.6</sub> CS <sub>0.4</sub> Pb(I <sub>0.7</sub> Br <sub>0.3</sub> ) <sub>3</sub> /FA <sub>0.75</sub> CS <sub>0.25</sub> Sn <sub>0.5</sub> Pb <sub>0.5</sub> I <sub>3</sub>	1.81	14.8	71.3	19.1	[104]
2018	MAPbI <sub>3</sub> /MAPbI <sub>3</sub>	2.3	9.84	79.6	18.0	[161]
2018	FA <sub>0.75</sub> CS <sub>0.25</sub> Pb(I <sub>0.8</sub> Br <sub>0.2</sub> ) <sub>3</sub> /Si	1.77	18.4	77	25.0	[136]
2018	(FAPbI <sub>3</sub> ) <sub>0.83</sub> (MAPbBr <sub>3</sub> ) <sub>0.17</sub> /homo-junction Si	1.74	16.2	78	21.9	[140]
2018	CS <sub>0.09</sub> FA <sub>0.77</sub> MA <sub>0.14</sub> Pb(I <sub>0.86</sub> Br <sub>0.14</sub> ) <sub>3</sub> /CIGS	1.774	17.3	73.1	22.4	[142]
2018	CS <sub>0.15</sub> (FA <sub>0.83</sub> MA <sub>0.17</sub> ) <sub>0.85</sub> Pb(I <sub>0.8</sub> Br <sub>0.2</sub> ) <sub>3</sub> /Si	1.80	17.8	79.4	25.4	[133]
2018	FA <sub>0.83</sub> CS <sub>0.17</sub> Pb(Br <sub>0.5</sub> I <sub>0.5</sub> ) <sub>3</sub> /FA <sub>0.5</sub> MA <sub>0.5</sub> Pb <sub>0.5</sub> Sn <sub>0.5</sub> I <sub>3</sub>	1.72	12.8	73	16.1	[159]
2018	CS <sub>0.05</sub> (MA <sub>0.17</sub> FA <sub>0.83</sub> )Pb <sub>1.1</sub> (I <sub>0.83</sub> Br <sub>0.17</sub> ) <sub>3</sub> /Si	1.76	18.5	78.5	25.5	[137]
2018	FA <sub>0.8</sub> CS <sub>0.2</sub> Pb(I <sub>0.7</sub> Br <sub>0.3</sub> ) <sub>3</sub> /(FASnI <sub>3</sub> ) <sub>0.6</sub> (MAPbI <sub>3</sub> ) <sub>0.4</sub>	1.92	14.0	78.1	21.0	[101]



## References

- [1] Correa-Baena J-P, Saliba M, Buonassisi T, Grätzel M, Abate A, Tress W, Hagfeldt A 2017 Promises and challenges of perovskite solar cells *Science* **358** 739-744
- [2] Snaith H J 2018 Present status and future prospects of perovskite photovoltaics *Nat. Mater.* **17** 372-376
- [3] Leijtens T, Bush K A, Prasanna R, McGehee M D 2018 Opportunities and challenges for tandem solar cells using metal halide perovskite semiconductors *Nat. Energy* **3** 828-838
- [4] Eperon G E, Hörantner M T, Snaith H J 2017 Metal halide perovskite tandem and multiple-junction photovoltaics *Nat. Rev. Chem.* **1** 0095
- [5] Correa-Baena J-P, Abate A, Saliba M, Tress W, Jesper Jacobsson T, Gratzel M, Hagfeldt A 2017 The rapid evolution of highly efficient perovskite solar cells *Energy Environ. Sci.* **10** 710-727
- [6] Song Z, McElvany C L, Phillips A B, Celik I, Krantz P W, Wathage S C, Liyanage G K, Apul D, Heben M J 2017 A techno-economic analysis of perovskite solar module manufacturing with low-cost materials and techniques *Energy Environ. Sci.* **10** 1297-1305
- [7] NREL Solar Cell Efficiency Chart [Online]. Available: (<https://www.nrel.gov/pv/assets/images/efficiency-chart-20180716.jpg>) [Accessed: 14 February 2019]
- [8] Shockley W, Queisser H J 1961 Detailed Balance Limit of Efficiency of p-n Junction Solar Cells *J. Appl. Phys.* **32** 510-519
- [9] Vos A D 1980 Detailed balance limit of the efficiency of tandem solar cells *Journal of Physics D: Applied Physics* **13** 839
- [10] Chiu P T, Law D C, Woo R L, Singer S B, Bhusari D, Hong W D, Zakaria A, Boisvert J, Mesropian S, King R R, Karam N H 2014 35.8% space and 38.8% terrestrial 5J direct bonded cells, in: 2014 IEEE 40th Photovoltaic Specialist Conference (PVSC), 2014, pp. 0011-0013.
- [11] Chiu P T, Law D C, Woo R L, Singer S B, Bhusari D, Hong W D, Zakaria A, Boisvert J, Mesropian S, King R R, Karam N H 2014 Direct Semiconductor Bonded 5J Cell for Space and Terrestrial Applications *IEEE J. Photovol.* **4** 493-497
- [12] King R R, Law D C, Edmondson K M, Fetzer C M, Kinsey G S, Yoon H, Sherif R A, Karam N H 2007 40% efficient metamorphic GaInP / GaInAs / Ge multijunction solar cells *Appl. Phys. Lett.* **90** 183516
- [13] Green M A, Hishikawa Y, Dunlop E D, Levi D H, Hohl-Ebinger J, Yoshita M, Ho-Baillie A W Y 2019 Solar cell efficiency tables (Version 53) *Prog. Photovoltaics* **27** 3-12
- [14] Yang J, Banerjee A, Guha S 1997 Triple-junction amorphous silicon alloy solar cell with 14.6% initial and 13.0% stable conversion efficiencies *Applied Physics Letters* **70** 2975-2977
- [15] Sai H, Matsui T, Matsubara K 2016 Stabilized 14.0%-efficient triple-junction thin-film silicon solar cell *Appl. Phys. Lett.* **109** 183506
- [16] Mailoa J P, Lee M, Peters I M, Buonassisi T, Panchula A, Weiss D N 2016 Energy-yield prediction for II-VI-based thin-film tandem solar cells *Energy Environ. Sci.* **9** 2644-2653
- [17] Chen B, Zheng X, Bai Y, Padture N P, Huang J 2017 Progress in Tandem Solar Cells Based on Hybrid Organic-Inorganic Perovskites *Adv. Energy Mater.* **7** 1602400
- [18] Anaya M, Lozano G, Calvo M E, Míguez H 2017 ABX<sub>3</sub> Perovskites for Tandem Solar Cells *Joule* **1** 769-793
- [19] Werner J, Niesen B, Ballif C 2017 Perovskite/Silicon Tandem Solar Cells: Marriage of Convenience or True Love Story? – An Overview *Adv. Mater. Interfaces* **5** 1700731
- [20] Yang T C-J, Fiala P, Jeangros Q, Ballif C 2018 High-Bandgap Perovskite Materials for Multijunction Solar Cells *Joule* **2** 1421-1436
- [21] Lal N N, Dkhissi Y, Li W, Hou Q, Cheng Y-B, Bach U 2017 Perovskite Tandem Solar Cells *Adv. Energy Mater.* **7** 1602761
- [22] Song Z, Wathage S C, Phillips A B, Heben M J 2016 Pathways toward high-performance perovskite solar cells: review of recent advances in organo-metal halide perovskites for photovoltaic applications *J. Photonics Energy* **6** 022001
- [23] Unger E L, Kegelmann L, Suchan K, Sörell D, Korte L, Albrecht S 2017 Roadmap and roadblocks for the band gap tunability of metal halide perovskites *J. Mater. Chem. A* **5** 11401-11409
- [24] Wang Z, Song Z, Yan Y, Liu S, Yang D 2019 Perovskite—a Perfect Top Cell for Tandem Devices to Break the S-Q Limit *Adv. Sci.* **10**.1002/advs.201801704
- [25] Wathage S C, Song Z, Phillips A B, Heben M J, Chapter 3 - Evolution of Perovskite Solar Cells, in: S. Thomas, A. Thankappan (Eds.) *Perovskite Photovoltaics*, Academic Press, 2018, pp. 43-88.
- [26] Kojima A, Teshima K, Shirai Y, Miyasaka T 2009 Organometal Halide Perovskites as Visible-Light Sensitizers for Photovoltaic Cells *J. Am. Chem. Soc.* **131** 6050-6051
- [27] Kim H-S, Lee C-R, Im J-H, Lee K-B, Moehl T, Marchioro A, Moon S-J, Humphry-Baker R, Yum J-H, Moser J E, Graetzel M, Park N-G 2012 Lead Iodide Perovskite Sensitized All-Solid-State Submicron Thin Film Mesoscopic Solar Cell with Efficiency Exceeding 9% *Sci. Rep.* **2** 591
- [28] Lee M M, Teuscher J, Miyasaka T, Murakami T N, Snaith H J 2012 Efficient Hybrid Solar Cells Based on Meso-Structured Organometal Halide Perovskites *Science* **338** 643-647
- [29] Kieslich G, Sun S, Cheetham A K 2015 An extended Tolerance Factor approach for organic-inorganic perovskites *Chem. Sci.* **6** 3430-3433
- [30] Saliba M, Correa-Baena J-P, Grätzel M, Hagfeldt A, Abate A 2018 Perovskite Solar Cells: From the Atomic Level to Film Quality and Device Performance *Angew. Chem., Int. Ed.* **57** 2554-2569
- [31] Comin R, Walters G, Thibau E S, Voznyy O, Lu Z-H, Sargent E H 2015 Structural, optical, and electronic studies of wide-bandgap lead halide perovskites *J. Mater. Chem. C* **3** 8839-8843

- [32] Protesescu L, Yakunin S, Bodnarchuk M I, Krieg F, Caputo R, Hendon C H, Yang R X, Walsh A, Kovalenko M V 2015 Nanocrystals of Cesium Lead Halide Perovskites ( $\text{CsPbX}_3$ ,  $X = \text{Cl, Br, and I}$ ): Novel Optoelectronic Materials Showing Bright Emission with Wide Color Gamut *Nano Lett.* **15** 3692-3696
- [33] Jesper Jacobsson T, Correa-Baena J-P, Pazoki M, Saliba M, Schenk K, Gratzel M, Hagfeldt A 2016 Exploration of the compositional space for mixed lead halogen perovskites for high efficiency solar cells *Energy Environ. Sci.* **9** 1706-1724
- [34] Hoke E T, Slotcavage D J, Dohner E R, Bowring A R, Karunadasa H I, McGehee M D 2015 Reversible photo-induced trap formation in mixed-halide hybrid perovskites for photovoltaics *Chem. Sci.* **6** 613-617
- [35] Hao F, Stoumpos C C, Chang R P H, Kanatzidis M G 2014 Anomalous Band Gap Behavior in Mixed Sn and Pb Perovskites Enables Broadening of Absorption Spectrum in Solar Cells *J. Am. Chem. Soc.* **136** 8094-8099
- [36] Im J, Stoumpos C C, Jin H, Freeman A J, Kanatzidis M G 2015 Antagonism between Spin-Orbit Coupling and Steric Effects Causes Anomalous Band Gap Evolution in the Perovskite Photovoltaic Materials  $\text{CH}_3\text{NH}_3\text{Sn}_{1-x}\text{Pb}_x\text{I}_3$  *J. Phys. Chem. Lett.* **6** 3503-3509
- [37] Yang W S, Park B-W, Jung E H, Jeon N J, Kim Y C, Lee D U, Shin S S, Seo J, Kim E K, Noh J H, Seok S I 2017 Iodide management in formamidinium-lead-halide-based perovskite layers for efficient solar cells *Science* **356** 1376-1379
- [38] Saliba M, Correa-Baena J-P, Wolff C M, Stolterfoht M, Phung N, Albrecht S, Neher D, Abate A 2018 How to Make over 20% Efficient Perovskite Solar Cells in Regular (n-i-p) and Inverted (p-i-n) Architectures *Chem. Mater.* **30** 4193-4201
- [39] Noh J H, Im S H, Heo J H, Mandal T N, Seok S I 2013 Chemical Management for Colorful, Efficient, and Stable Inorganic-Organic Hybrid Nanostructured Solar Cells *Nano Lett.* **13** 1764-1769
- [40] Eperon G E, Stranks S D, Menelaou C, Johnston M B, Herz L M, Snaith H J 2014 Formamidinium lead trihalide: a broadly tunable perovskite for efficient planar heterojunction solar cells *Energy Environ. Sci.* **7** 982-988
- [41] McMeekin D P, Sadoughi G, Rehman W, Eperon G E, Saliba M, Hörantner M T, Haghighirad A, Sakai N, Korte L, Rech B, Johnston M B, Herz L M, Snaith H J 2016 A mixed-cation lead mixed-halide perovskite absorber for tandem solar cells *Science* **351** 151-155
- [42] Stoumpos C C, Malliakas C D, Kanatzidis M G 2013 Semiconducting Tin and Lead Iodide Perovskites with Organic Cations: Phase Transitions, High Mobilities, and Near-Infrared Photoluminescent Properties *Inorg. Chem.* **52** 9019-9038
- [43] Bi C, Yuan Y, Fang Y, Huang J 2015 Low-Temperature Fabrication of Efficient Wide-Bandgap Organolead Trihalide Perovskite Solar Cells *Adv. Energy Mater.* **5** 1401616
- [44] Hu M, Bi C, Yuan Y, Bai Y, Huang J 2016 Stabilized Wide Bandgap  $\text{MAPbBr}_{1-x}\text{I}_x$  Perovskite by Enhanced Grain Size and Improved Crystallinity *Adv. Sci.* **3** 1500301
- [45] Bi C, Wang Q, Shao Y, Yuan Y, Xiao Z, Huang J 2015 Non-wetting surface-driven high-aspect-ratio crystalline grain growth for efficient hybrid perovskite solar cells *Nat. Commun.* **6** 7747
- [46] Duong T, Wu Y, Shen H, Peng J, Fu X, Jacobs D, Wang E-C, Kho T C, Fong K C, Stocks M, Franklin E, Blakers A, Zin N, McIntosh K, Li W, Cheng Y-B, White T P, Weber K, Catchpole K 2017 Rubidium Multication Perovskite with Optimized Bandgap for Perovskite-Silicon Tandem with over 26% Efficiency *Adv. Energy Mater.* **7** 1700228
- [47] Yu Y, Wang C, Grice C R, Shrestha N, Zhao D, Liao W, Guan L, Awni R A, Meng W, Cimaroli A J, Zhu K, Ellingson R J, Yan Y 2017 Synergistic Effects of Lead Thiocyanate Additive and Solvent Annealing on the Performance of Wide-Bandgap Perovskite Solar Cells *ACS Energy Lett.* **2** 1177-1182
- [48] Zhou Y, Jia Y-H, Fang H-H, Loi M A, Xie F-Y, Gong L, Qin M-C, Lu X-H, Wong C-P, Zhao N 2018 Composition-Tuned Wide Bandgap Perovskites: From Grain Engineering to Stability and Performance Improvement *Adv. Funct. Mater.* **28** 1803130
- [49] Zhou Y, Wang F, Cao Y, Wang J-P, Fang H-H, Loi M A, Zhao N, Wong C-P 2017 Benzylamine-Treated Wide-Bandgap Perovskite with High Thermal-Photostability and Photovoltaic Performance *Adv. Energy Mater.* **7** 1701048
- [50] Zheng X, Chen B, Dai J, Fang Y, Bai Y, Lin Y, Wei H, Zeng Xiao C, Huang J 2017 Defect passivation in hybrid perovskite solar cells using quaternary ammonium halide anions and cations *Nat. Energy* **2** 17102
- [51] Lin Y, Chen B, Zhao F, Zheng X, Deng Y, Shao Y, Fang Y, Bai Y, Wang C, Huang J 2017 Matching Charge Extraction Contact for Wide-Bandgap Perovskite Solar Cells *Adv. Mater.* **29** 1700607
- [52] Kim J, Saidaminov M I, Tan H, Zhao Y, Kim Y, Choi J, Jo J W, Fan J, Quintero-Bermudez R, Yang Z, Quan L N, Wei M, Voznyy O, Sargent E H 2018 Amide-Catalyzed Phase-Selective Crystallization Reduces Defect Density in Wide-Bandgap Perovskites *Adv. Mater.* **30** 1706275
- [53] Tan H, Che F, Wei M, Zhao Y, Saidaminov M I, Todorović P, Broberg D, Walters G, Tan F, Zhuang T, Sun B, Liang Z, Yuan H, Fron E, Kim J, Yang Z, Voznyy O, Asta M, Sargent E H 2018 Dipolar cations confer defect tolerance in wide-bandgap metal halide perovskites *Nat. Commun.* **9** 3100
- [54] Liu Z, Krückemeier L, Krogmeier B, Klingebiel B, Márquez J A, Levchenko S, Öz S, Mathur S, Rau U, Unold T, Kirchartz T 2019 Open-Circuit Voltages Exceeding 1.26 V in Planar Methylammonium Lead Iodide Perovskite Solar Cells *ACS Energy Lett.* **4** 110-117
- [55] Bischak C G, Hetherington C L, Wu H, Aloni S, Ogletree D F, Limmer D T, Ginsberg N S 2017 Origin of Reversible Photoinduced Phase Separation in Hybrid Perovskites *Nano Lett.* **17** 1028-1033
- [56] Knight A J, Wright A D, Patel J B, McMeekin D P, Snaith H J, Johnston M B, Herz L M 2018 Electronic Traps and Phase Segregation in Lead Mixed-Halide Perovskite *ACS Energy Lett.* **4** 75-84
- [57] Braly I L, Stoddard R J, Rajagopal A, Uhl A R, Katahara J K, Jen A K Y, Hillhouse H W 2017 Current-Induced Phase Segregation in Mixed Halide Hybrid Perovskites and its Impact on Two-Terminal Tandem Solar Cell Design *ACS Energy Lett.* **2** 1841-1847

- [58] Lin Y, Chen B, Fang Y, Zhao J, Bao C, Yu Z, Deng Y, Rudd P N, Yan Y, Yuan Y, Huang J 2018 Excess charge-carrier induced instability of hybrid perovskites *Nat. Commun.* **9** 4981
- [59] Brennan M C, Draguta S, Kamat P V, Kuno M 2018 Light-Induced Anion Phase Segregation in Mixed Halide Perovskites *ACS Energy Lett.* **3** 204-213
- [60] Slotcavage D J, Karunadasa H I, McGehee M D 2016 Light-Induced Phase Segregation in Halide-Perovskite Absorbers *ACS Energy Lett.* **1** 1199-1205
- [61] Ruth A, Brennan M C, Draguta S, Morozov Y V, Zhukovskiy M, Janko B, Zapol P, Kuno M 2018 Vacancy-Mediated Anion Photosegregation Kinetics in Mixed Halide Hybrid Perovskites: Coupled Kinetic Monte Carlo and Optical Measurements *ACS Energy Lett.* **3** 2321-2328
- [62] Samu G F, Janáky C, Kamat P V 2017 A Victim of Halide Ion Segregation. How Light Soaking Affects Solar Cell Performance of Mixed Halide Lead Perovskites *ACS Energy Lett.* **2** 1860-1861
- [63] Barker A J, Sadhanala A, Deschler F, Gandini M, Senanayak S P, Pearce P M, Mosconi E, Pearson A J, Wu Y, Srimath Kandada A R, Leijtens T, De Angelis F, Dutton S E, Petrozza A, Friend R H 2017 Defect-Assisted Photoinduced Halide Segregation in Mixed-Halide Perovskite Thin Films *ACS Energy Lett.* **2** 1416-1424
- [64] Gualdrón-Reyes A F, Yoon S J, Mora-Seró I 2018 Recent insights for achieving mixed halide perovskites without halide segregation *Current Opinion in Electrochemistry* **11** 84-90
- [65] Bush K A, Frohna K, Prasanna R, Beal R E, Leijtens T, Swifter S A, McGehee M D 2018 Compositional Engineering for Efficient Wide Band Gap Perovskites with Improved Stability to Photoinduced Phase Segregation *ACS Energy Lett.* **3** 428-435
- [66] Yang Z, Rajagopal A, Jo S B, Chueh C-C, Williams S, Huang C-C, Katahara J K, Hillhouse H W, Jen A K Y 2016 Stabilized Wide Bandgap Perovskite Solar Cells by Tin Substitution *Nano Lett.* **16** 7739-7747
- [67] Abdi-Jalebi M, Andaji-Garmaroudi Z, Cacovich S, Stavrakas C, Philippe B, Richter J M, Alsari M, Booker E P, Hutter E M, Pearson A J, Lilliu S, Savenije T J, Rensmo H, Divitini G, Ducati C, Friend R H, Stranks S D 2018 Maximizing and stabilizing luminescence from halide perovskites with potassium passivation *Nature* **555** 497
- [68] Belisle R A, Bush K A, Bertoluzzi L, Gold-Parker A, Toney M F, McGehee M D 2018 Impact of Surfaces on Photoinduced Halide Segregation in Mixed-Halide Perovskites *ACS Energy Lett.* **3** 2694-2700
- [69] Gualdrón-Reyes A F, Yoon S J, Barea E M, Agouram S, Muñoz-Sanjosé V, Meléndez Á M, Niño-Gómez M E, Mora-Seró I 2018 Controlling the Phase Segregation in Mixed Halide Perovskites through Nanocrystal Size *ACS Energy Lett.* **4** 54-62
- [70] Stoddard R J, Rajagopal A, Palmer R L, Braly I L, Jen A K Y, Hillhouse H W 2018 Enhancing Defect Tolerance and Phase Stability of High-Bandgap Perovskites via Guanidinium Alloying *ACS Energy Lett.* **3** 1261-1268
- [71] Xiao Z, Zhao L, Tran N L, Lin Y L, Silver S H, Kerner R A, Yao N, Kahn A, Scholes G D, Rand B P 2017 Mixed-Halide Perovskites with Stabilized Bandgaps *Nano Lett.* **17** 6863-6869
- [72] Rajagopal A, Stoddard R J, Jo S B, Hillhouse H W, Jen A K Y 2018 Overcoming the Photovoltage Plateau in Large Bandgap Perovskite Photovoltaics *Nano Lett.* **18** 3985-3993
- [73] Howard J M, Tennyson E M, Neves B R A, Leite M S 2018 Machine Learning for Perovskites' Reap-Rest-Recovery Cycle *Joule* <https://doi.org/10.1016/j.joule.2018.11.010> DOI: 10.1016/j.joule.2018.1011.1010
- [74] Chen S, Hou Y, Chen H, Tang X, Langner S, Li N, Stubhan T, Levchuk I, Gu E, Osvet A, Brabec C J 2018 Exploring the Stability of Novel Wide Bandgap Perovskites by a Robot Based High Throughput Approach *Adv. Energy Mater.* **8** 1701543
- [75] Zhu H L, Choy W C H 2018 Crystallization, Properties, and Challenges of Low-Bandgap Sn-Pb Binary Perovskites *Solar RRL* **2** 1800146
- [76] Wang C, Song Z, Li C, Zhao D, Yan Y 2018 Low-bandgap mixed tin-lead perovskites and their applications in all-perovskite tandem solar cells *Adv. Funct. Mater.* DOI:10.1002/adfm.201808801
- [77] Xiao Z, Song Z, Yan Y From Lead Halide Perovskites to Lead-Free Metal Halide Perovskites and Perovskite Derivatives *Adv. Mater.* **0** 1803792
- [78] Hao F, Stoumpos C C, Duyen Hanh C, Chang R P H, Kanatzidis M G 2014 Lead-free solid-state organic-inorganic halide perovskite solar cells *Nat. Photon.* **8** 489-494
- [79] Noel N K, Stranks S D, Abate A, Wehrenfennig C, Guarnera S, Haghighirad A-A, Sadhanala A, Eperon G E, Pathak S K, Johnston M B, Petrozza A, Herz L M, Snaith H J 2014 Lead-free organic-inorganic tin halide perovskites for photovoltaic applications *Energy Environ. Sci.* **7** 3061-3068
- [80] Lee S J, Shin S S, Kim Y C, Kim D, Ahn T K, Noh J H, Seo J, Seok S I 2016 Fabrication of Efficient Formamidinium Tin Iodide Perovskite Solar Cells through SnF<sub>2</sub>-Pyrazine Complex *J. Am. Chem. Soc.* **138** 3974-3977
- [81] Liao W, Zhao D, Yu Y, Grice C R, Wang C, Cimaroli A J, Schulz P, Meng W, Zhu K, Xiong R-G, Yan Y 2016 Lead-Free Inverted Planar Formamidinium Tin Triiodide Perovskite Solar Cells Achieving Power Conversion Efficiencies up to 6.22% *Adv. Mater.* **28** 9333-9340
- [82] Ke W, Stoumpos C C, Spanopoulos I, Mao L, Chen M, Wasielewski M R, Kanatzidis M G 2017 Efficient Lead-Free Solar Cells Based on Hollow {en}MASnI<sub>3</sub> Perovskites *J. Am. Chem. Soc.* **139** 14800-14806
- [83] Ke W, Stoumpos C C, Zhu M, Mao L, Spanopoulos I, Liu J, Kontsevoi O Y, Chen M, Sarma D, Zhang Y, Wasielewski M R, Kanatzidis M G 2017 Enhanced photovoltaic performance and stability with a new type of hollow 3D perovskite {en}FASnI<sub>3</sub> *Sci. Adv.* **3** e1701293
- [84] Liu X, Yan K, Tan D, Liang X, Zhang H, Huang W 2018 Solvent Engineering Improves Efficiency of Lead-Free Tin-Based Hybrid Perovskite Solar Cells beyond 9% *ACS Energy Lett.* **3** 2701-2707
- [85] Shuyan S, Jian L, Giuseppe P, Hong-Hua F, R. B G, H. t B G, Anton K L J, Antonietta L M 2018 Highly Reproducible Sn-Based Hybrid Perovskite Solar Cells with 9% Efficiency *Adv. Energy Mater.* **8** 1702019

- [86] Liao Y, Liu H, Zhou W, Yang D, Shang Y, Shi Z, Li B, Jiang X, Zhang L, Quan L N, Quintero-Bermudez R, Sutherland B R, Mi Q, Sargent E H, Ning Z 2017 Highly Oriented Low-Dimensional Tin Halide Perovskites with Enhanced Stability and Photovoltaic Performance *J. Am. Chem. Soc.* **139** 6693-6699
- [87] Wang F, Jiang X, Chen H, Shang Y, Liu H, Wei J, Zhou W, He H, Liu W, Ning Z 2018 2D-Quasi-2D-3D Hierarchy Structure for Tin Perovskite Solar Cells with Enhanced Efficiency and Stability *Joule* **2** 2732-2743
- [88] Jokar E, Chien C-H, Fathi A, Rameez M, Chang Y-H, Diau E W-G 2018 Slow surface passivation and crystal relaxation with additives to improve device performance and durability for tin-based perovskite solar cells *Energy Environ. Sci.* **11** 2353-2362
- [89] Jokar E, Chien C-H, Tsai C-M, Fathi A, Diau E W-G Robust Tin-Based Perovskite Solar Cells with Hybrid Organic Cations to Attain Efficiency Approaching 10% *Adv. Mater.* **0** 1804835
- [90] Ogomi Y, Morita A, Tsukamoto S, Saitho T, Fujikawa N, Shen Q, Toyoda T, Yoshino K, Pandey S S, Ma T, Hayase S 2014 CH<sub>3</sub>NH<sub>3</sub>SnxPb(1-x)I<sub>3</sub> Perovskite Solar Cells Covering up to 1060 nm *J. Phys. Chem. Lett.* **5** 1004-1011
- [91] Zuo F, Williams S T, Liang P-W, Chueh C-C, Liao C-Y, Jen A K-Y 2014 Binary-Metal Perovskites Toward High-Performance Planar-Heterojunction Hybrid Solar Cells *Adv. Mater.* **26** 6454-6460
- [92] Li Y, Sun W, Yan W, Ye S, Rao H, Peng H, Zhao Z, Bian Z, Liu Z, Zhou H, Huang C 2016 50% Sn-Based Planar Perovskite Solar Cell with Power Conversion Efficiency up to 13.6% *Adv. Energy Mater.* **6** 1601353
- [93] Rajagopal A, Liang P-W, Chueh C-C, Yang Z, Jen A K Y 2017 Defect Passivation via a Graded Fullerene Heterojunction in Low-Bandgap Pb-Sn Binary Perovskite Photovoltaics *ACS Energy Lett.* **2** 2531-2539
- [94] Yang Z, Rajagopal A, Jen A K-Y 2017 Ideal Bandgap Organic-Inorganic Hybrid Perovskite Solar Cells *Adv. Mater.* **29** 1704418
- [95] Yang Z, Rajagopal A, Chueh C-C, Jo S B, Liu B, Zhao T, Jen A K Y 2016 Stable Low-Bandgap Pb-Sn Binary Perovskites for Tandem Solar Cells *Adv. Mater.* **28** 1602696
- [96] Liao W, Zhao D, Yu Y, Shrestha N, Ghimire K, Grice C R, Wang C, Xiao Y, Cimaroli A J, Ellingson R J, Podraza N J, Zhu K, Xiong R-G, Yan Y 2016 Fabrication of Efficient Low-Bandgap Perovskite Solar Cells by Combining Formamidinium Tin Iodide with Methylammonium Lead Iodide *J. Am. Chem. Soc.* **138** 12360-12363
- [97] Zhao D, Yu Y, Wang C, Liao W, Shrestha N, Grice C R, Cimaroli A J, Guan L, Ellingson R J, Zhu K, Zhao X, Xiong R-G, Yan Y 2017 Low-bandgap mixed tin-lead iodide perovskite absorbers with long carrier lifetimes for all-perovskite tandem solar cells *Nat. Energy* **2** 17018
- [98] Prasanna R, Gold-Parker A, Leijtens T, Conings B, Babayigit A, Boyen H-G, Toney M F, McGehee M D 2017 Band Gap Tuning via Lattice Contraction and Octahedral Tilting in Perovskite Materials for Photovoltaics *J. Am. Chem. Soc.* **139** 11117-11124
- [99] Kapil G, Ripolles T S, Hamada K, Ogomi Y, Bessho T, Kinoshita T, Chantana J, Yoshino K, Shen Q, Toyoda T, Minemoto T, Murakami T N, Segawa H, Hayase S 2018 Highly Efficient 17.6% Tin-Lead Mixed Perovskite Solar Cells Realized through Spike Structure *Nano Lett.* **18** 3600-3607
- [100] Xu G, Bi P, Wang S, Xue R, Zhang J, Chen H, Chen W, Hao X, Li Y, Li Y 2018 Integrating Ultrathin Bulk-Heterojunction Organic Semiconductor Intermediary for High-Performance Low-Bandgap Perovskite Solar Cells with Low Energy Loss *Adv. Funct. Mater.* **28** 1804427
- [101] Zhao D, Chen C, Wang C, Junda M M, Song Z, Grice C R, Yu Y, Li C, Subedi B, Podraza N J, Zhao X, Fang G, Xiong R-G, Zhu K, Yan Y 2018 Efficient two-terminal all-perovskite tandem solar cells enabled by high-quality low-bandgap absorber layers *Nat. Energy* **3** 1093-1100
- [102] Li C, Song Z, Zhao D, Xiao C, Subedi B, Shrestha N, Junda M M, Wang C, Jiang C-S, Al-Jassim M, Ellingson R J, Podraza N J, Zhu K, Yan Y 2019 Reducing Saturation-Current Density to Realize High-Efficiency Low-Bandgap Mixed Tin-Lead Halide Perovskite Solar Cells *Adv. Energy Mater.* **9** 1803135
- [103] Eperon G E, Leijtens T, Bush K A, Prasanna R, Green T, Wang J T-W, McMeekin D P, Volonakis G, Milot R L, May R, Palmstrom A, Slotcavage D J, Belisle R A, Patel J B, Parrott E S, Sutton R J, Ma W, Moghadam F, Conings B, Babayigit A, Boyen H-G, Bent S, Giustino F, Herz L M, Johnston M B, McGehee M D, Snaith H J 2016 Perovskite-perovskite tandem photovoltaics with optimized band gaps *Science* **354** 861-865
- [104] Leijtens T, Prasanna R, Bush K A, Eperon G E, Raiford J A, Gold-Parker A, Wolf E J, Swifter S A, Boyd C C, Wang H-P, Toney M F, Bent S F, McGehee M D 2018 Tin-lead halide perovskites with improved thermal and air stability for efficient all-perovskite tandem solar cells *Sustainable Energy Fuels* **2** 2450-2459
- [105] Zong Y, Wang N, Zhang L, Ju M-G, Zeng X C, Sun X W, Zhou Y, Padture N P 2017 Homogenous Alloys of Formamidinium Lead Triiodide and Cesium Tin Triiodide for Efficient Ideal-Bandgap Perovskite Solar Cells *Angew. Chem., Int. Ed.* **56** 12658-12662
- [106] Zong Y, Zhou Z, Chen M, Padture N P, Zhou Y 2018 Lewis-Adduct Mediated Grain-Boundary Functionalization for Efficient Ideal-Bandgap Perovskite Solar Cells with Superior Stability *Adv. Energy Mater.* **8** 1800997
- [107] deQuilettes D W, Koch S, Burke S, Paranj R K, Shropshire A J, Ziffer M E, Ginger D S 2016 Photoluminescence Lifetimes Exceeding 8  $\mu$ s and Quantum Yields Exceeding 30% in Hybrid Perovskite Thin Films by Ligand Passivation *ACS Energy Lett.* **1** 438-444
- [108] Turren-Cruz S-H, Saliba M, Mayer M T, Juárez-Santisteban H, Mathew X, Nienhaus L, Tress W, Erodici M P, Sher M-J, Bawendi M G, Grätzel M, Abate A, Hagfeldt A, Correa-Baena J-P 2018 Enhanced charge carrier mobility and lifetime suppress hysteresis and improve efficiency in planar perovskite solar cells *Energy Environ. Sci.* **11** 78-86

- [109] Song Z, Wang C, Phillips A B, Grice C R, Zhao D, Yu Y, Chen C, Li C, Yin X, Ellingson R, Heben M, Yan Y 2018 Probing the Origins of Photodegradation in Organic-Inorganic Metal Halide Perovskites with Time-Resolved Mass Spectrometry *Sustainable Energy Fuels* **2** 2460-2467
- [110] Lang F, Shargaieva O, Brus V V, Neitzert H C, Rappich J, Nickel N H 2018 Influence of Radiation on the Properties and the Stability of Hybrid Perovskites *Adv. Mater.* **30** 1702905
- [111] Chi D, Huang S, Zhang M, Mu S, Zhao Y, Chen Y, You J 2018 Composition and Interface Engineering for Efficient and Thermally Stable Pb-Sn Mixed Low-Bandgap Perovskite Solar Cells *Adv. Funct. Mater.* **28** 1804603
- [112] Xu X, Chueh C-C, Yang Z, Rajagopal A, Xu J, Jo S B, Jen A K Y 2017 Ascorbic acid as an effective antioxidant additive to enhance the efficiency and stability of Pb/Sn-based binary perovskite solar cells *Nano Energy* **34** 392-398
- [113] Zhu Z, Li N, Zhao D, Wang L, Jen A K-Y 2018 Improved Efficiency and Stability of Pb/Sn Binary Perovskite Solar Cells Fabricated by Galvanic Displacement Reaction *Adv. Energy Mater.* **9** 1802774
- [114] Dupré O, Niesen B, De Wolf S, Ballif C 2018 Field Performance versus Standard Test Condition Efficiency of Tandem Solar Cells and the Singular Case of Perovskites/Silicon Devices *J. Phys. Chem. Lett.* **9** 446-458
- [115] Langenhorst M, Sautter B, Schmager R, Lehr J, Ahlswede E, Powalla M, Lemmer U, Richards B S, Paetzold U W Energy yield of all thin-film perovskite/CIGS tandem solar modules *Prog. Photovoltaics* doi:10.1002/ppv.3091
- [116] Hörantner M T, Snaith H J 2017 Predicting and optimising the energy yield of perovskite-on-silicon tandem solar cells under real world conditions *Energy Environ. Sci.* **10** 1983-1993
- [117] Geisz J F, Friedman D J 2002 III-N-V semiconductors for solar photovoltaic applications *Semicond. Sci. Technol.* **17** 769
- [118] Hörantner M T, Leijtens T, Ziffer M E, Eperon G E, Christoforo M G, McGehee M D, Snaith H J 2017 The Potential of Multijunction Perovskite Solar Cells *ACS Energy Lett.* **2** 2506-2513
- [119] Yu Z J, Carpenter J V, Holman Z C 2018 Techno-economic viability of silicon-based tandem photovoltaic modules in the United States *Nat. Energy* **3** 747-753
- [120] Li Z, Zhao Y, Wang X, Sun Y, Zhao Z, Li Y, Zhou H, Chen Q 2018 Cost Analysis of Perovskite Tandem Photovoltaics *Joule* **2** 1559-1572
- [121] Loper P, Moon S-J, Martin de Nicolas S, Niesen B, Ledinsky M, Nicolay S, Bailat J, Yum J-H, De Wolf S, Ballif C 2015 Organic-inorganic halide perovskite/crystalline silicon four-terminal tandem solar cells *Phys. Chem. Chem. Phys.* **17** 1619-1629
- [122] Bailie C D, Christoforo M G, Mailoa J P, Bowring A R, Unger E L, Nguyen W H, Burschka J, Pellet N, Lee J Z, Gratzel M, Noufi R, Buonassisi T, Salleo A, McGehee M D 2015 Semi-transparent perovskite solar cells for tandems with silicon and CIGS *Energy Environ. Sci.* **8** 956-963
- [123] Chen B, Bai Y, Yu Z, Li T, Zheng X, Dong Q, Shen L, Boccard M, Gruverman A, Holman Z, Huang J 2016 Efficient Semitransparent Perovskite Solar Cells for 23.0%-Efficiency Perovskite/Silicon Four-Terminal Tandem Cells *Adv. Energy Mater.* **6** 1601128
- [124] Werner J, Barraud L, Walter A, Bräuninger M, Sahli F, Sacchetto D, Tétreault N, Paviet-Salomon B, Moon S-J, Allebé C, Despeisse M, Nicolay S, De Wolf S, Niesen B, Ballif C 2016 Efficient Near-Infrared-Transparent Perovskite Solar Cells Enabling Direct Comparison of 4-Terminal and Monolithic Perovskite/Silicon Tandem Cells *ACS Energy Lett.* **1** 474-480
- [125] Jaysankar M, Raul B A L, Bastos J, Burgess C, Weijtens C, Creatore M, Aernouts T, Kuang Y, Gehlhaar R, Hadipour A, Poortmans J 2018 Minimizing Voltage Loss in Wide-Bandgap Perovskites for Tandem Solar Cells *ACS Energy Lett.* **4** 259-264
- [126] Mailoa J P, Bailie C D, Johlin E C, Hoke E T, Akey A J, Nguyen W H, McGehee M D, Buonassisi T 2015 A 2-terminal perovskite/silicon multijunction solar cell enabled by a silicon tunnel junction *Appl. Phys. Lett.* **106** 121105
- [127] Albrecht S, Saliba M, Correa Baena J P, Lang F, Kegelmann L, Mews M, Steier L, Abate A, Rappich J, Korte L, Schlattmann R, Nazeeruddin M K, Hagfeldt A, Gratzel M, Rech B 2016 Monolithic perovskite/silicon-heterojunction tandem solar cells processed at low temperature *Energy Environ. Sci.* **9** 81-88
- [128] Werner J, Weng C-H, Walter A, Fesquet L, Seif J P, De Wolf S, Niesen B, Ballif C 2016 Efficient Monolithic Perovskite/Silicon Tandem Solar Cell with Cell Area >1 cm<sup>2</sup> *J. Phys. Chem. Lett.* **7** 161-166
- [129] Song Z, Werner J, Shrestha N, Sahli F, De Wolf S, Niesen B, Watthage S C, Phillips A B, Ballif C, Ellingson R J, Heben M J 2016 Probing Photocurrent Nonuniformities in the Subcells of Monolithic Perovskite/Silicon Tandem Solar Cells *J. Phys. Chem. Lett.* **7** 5114-5120
- [130] Sahli F, Kamino B A, Werner J, Bräuninger M, Paviet-Salomon B, Barraud L, Monnard R, Seif J P, Tomasi A, Jeangros Q, Hessler-Wyser A, De Wolf S, Despeisse M, Nicolay S, Niesen B, Ballif C 2018 Improved Optics in Monolithic Perovskite/Silicon Tandem Solar Cells with a Nanocrystalline Silicon Recombination Junction *Adv. Energy Mater.* **8** 1701609
- [131] Bush K A, Palmstrom A F, Yu Z J, Boccard M, Cheacharoen R, Mailoa J P, McMeekin D P, Hoyer R L Z, Bailie C D, Leijtens T, Peters I M, Minichetti M C, Rolston N, Prasanna R, Sofia S, Harwood D, Ma W, Moghadam F, Snaith H J, Buonassisi T, Holman Z C, Bent S F, McGehee M D 2017 23.6%-efficient monolithic perovskite/silicon tandem solar cells with improved stability *Nat. Energy* **2** 17009
- [132] Bush K A, Bailie C D, Chen Y, Bowring A R, Wang W, Ma W, Leijtens T, Moghadam F, McGehee M D 2016 Thermal and Environmental Stability of Semi-Transparent Perovskite Solar Cells for Tandems Enabled by a Solution-Processed Nanoparticle Buffer Layer and Sputtered ITO Electrode *Adv. Mater.* **28** 3937-3943
- [133] Chen B, Yu Z, Liu K, Zheng X, Liu Y, Shi J, Spronk D, Rudd P N, Holman Z, Huang J 2018 Grain Engineering for Perovskite/Silicon Monolithic Tandem Solar Cells with Efficiency of 25.4% *Joule* <https://doi.org/10.1016/j.joule.2018.10.003>
- [134] Sahli F, Werner J, Kamino B A, Bräuninger M, Monnard R, Paviet-Salomon B, Barraud L, Ding L, Diaz Leon J J, Sacchetto D, Cattaneo G, Despeisse M, Boccard M, Nicolay S, Jeangros Q, Niesen B, Ballif C 2018 Fully textured monolithic perovskite/silicon tandem solar cells with 25.2% power conversion efficiency *Nat. Mater.* **17** 820-826

- [135] Werner J, Nogay G, Sahli F, Yang T C-J, Bräuninger M, Christmann G, Walter A, Kamino B A, Fiala P, Löper P, Nicolay S, Jeangros Q, Niesen B, Ballif C 2018 Complex Refractive Indices of Cesium–Formamidinium-Based Mixed-Halide Perovskites with Optical Band Gaps from 1.5 to 1.8 eV *ACS Energy Lett.* **3** 742-747
- [136] Bush K A, Manzoor S, Frohna K, Yu Z J, Raiford J A, Palmstrom A F, Wang H-P, Prasanna R, Bent S F, Holman Z C, McGehee M D 2018 Minimizing Current and Voltage Losses to Reach 25% Efficient Monolithic Two-Terminal Perovskite–Silicon Tandem Solar Cells *ACS Energy Lett.* **3** 2173-2180
- [137] Jošt M, Köhnen E, Morales-Vilches A B, Lipovšek B, Jäger K, Macco B, Al-Ashouri A, Krč J, Korte L, Rech B, Schlattmann R, Topič M, Stannowski B, Albrecht S 2018 Textured interfaces in monolithic perovskite/silicon tandem solar cells: advanced light management for improved efficiency and energy yield *Energy Environ. Sci.* **11** 3511-3523
- [138] Wu Y, Yan D, Peng J, Duong T, Wan Y, Phang S P, Shen H, Wu N, Barugkin C, Fu X, Surve S, Grant D, Walter D, White T P, Catchpole K R, Weber K J 2017 Monolithic perovskite/silicon-homojunction tandem solar cell with over 22% efficiency *Energy Environ. Sci.* **10** 2472-2479
- [139] Zheng J, Lau C F J, Mehrvarz H, Ma F-J, Jiang Y, Deng X, Soeriyadi A, Kim J, Zhang M, Hu L, Cui X, Lee D S, Bing J, Cho Y, Chen C, Green M A, Huang S, Ho-Baillie A W Y 2018 Large area efficient interface layer free monolithic perovskite/homo-junction-silicon tandem solar cell with over 20% efficiency *Energy Environ. Sci.* **11** 2432-2443
- [140] Zheng J, Mehrvarz H, Ma F-J, Lau C F J, Green M A, Huang S, Ho-Baillie A W Y 2018 21.8% Efficient Monolithic Perovskite/Homo-Junction-Silicon Tandem Solar Cell on 16 cm<sup>2</sup> *ACS Energy Lett.* **3** 2299-2300
- [141] Imec Perovskite/CIGS tandem cell with Record Efficiency of 24.6 percent Paves the Way for Flexible Solar Cells and High-Efficiency Building-Integrated PV 2018.[Online]. Available:(<https://www.imec-int.com/en/articles/perovskite-cigs-tandem-cell-with-record-efficiency-of-24-6-percent>) [Accessed: January 15 2019]
- [142] Han Q, Hsieh Y-T, Meng L, Wu J-L, Sun P, Yao E-P, Chang S-Y, Bae S-H, Kato T, Bermudez V, Yang Y 2018 High-performance perovskite/Cu(In,Ga)Se<sub>2</sub> monolithic tandem solar cells *Science* **361** 904-908
- [143] Yang Y, Chen Q, Hsieh Y-T, Song T-B, Marco N D, Zhou H, Yang Y 2015 Multilayer Transparent Top Electrode for Solution Processed Perovskite/Cu(In,Ga)(Se,S)<sub>2</sub> Four Terminal Tandem Solar Cells *ACS Nano* **9** 7714-7721
- [144] Kranz L, Abate A, Feurer T, Fu F, Avancini E, Löckinger J, Reinhard P, Zakeeruddin S M, Grätzel M, Buecheler S, Tiwari A N 2015 High-Efficiency Polycrystalline Thin Film Tandem Solar Cells *J. Phys. Chem. Lett.* **6** 2676-2681
- [145] Fu F, Feurer T, Jager T, Avancini E, Bissig B, Yoon S, Buecheler S, Tiwari A N 2015 Low-temperature-processed efficient semi-transparent planar perovskite solar cells for bifacial and tandem applications *Nat. Commun.* **6** 8932
- [146] Fu F, Feurer T, Weiss T P, Pisoni S, Avancini E, Andres C, Buecheler S, Tiwari A N 2016 High-efficiency inverted semi-transparent planar perovskite solar cells in substrate configuration *Nat. Energy* **2** 16190
- [147] Shen H, Duong T, Peng J, Jacobs D, Wu N, Gong J, Wu Y, Karuturi S K, Fu X, Weber K, Xiao X, White T P, Catchpole K 2018 Mechanically-stacked perovskite/CIGS tandem solar cells with efficiency of 23.9% and reduced oxygen sensitivity *Energy Environ. Sci.* **11** 394-406
- [148] Todorov T, Gershon T, Gunawan O, Sturdevant C, Guha S 2014 Perovskite-kesterite monolithic tandem solar cells with high open-circuit voltage *Appl. Phys. Lett.* **105** 173902
- [149] Todorov T, Gershon T, Gunawan O, Lee Y S, Sturdevant C, Chang L-Y, Guha S 2015 Monolithic Perovskite-CIGS Tandem Solar Cells via In Situ Band Gap Engineering *Adv. Energy Mater.* **5** 1500799
- [150] Uhl A R, Rajagopal A, Clark J A, Murray A, Feurer T, Buecheler S, Jen A K-Y, Hillhouse H W 2018 Solution-Processed Low-Bandgap CuIn(S,Se)<sub>2</sub> Absorbers for High-Efficiency Single-Junction and Monolithic Chalcopyrite-Perovskite Tandem Solar Cells *Adv. Energy Mater.* **8** 1801254
- [151] Jošt M, Bertram T, Koushik D, Marquez J A, Verheijen M A, Heinemann M D, Köhnen E, Al-Ashouri A, Braunger S, Lang F, Rech B, Unold T, Creatore M, Lauermaun I, Kaufmann C A, Schlattmann R, Albrecht S 2019 21.6%-Efficient Monolithic Perovskite/Cu(In,Ga)Se<sub>2</sub> Tandem Solar Cells with Thin Conformal Hole Transport Layers for Integration on Rough Bottom Cell Surfaces *ACS Energy Lett.* **4** 583-590
- [152] Celik I, Phillips A B, Song Z, Yan Y, Ellingson R J, Heben M J, Apul D 2017 Energy Pay-Back Time of Perovskite Tandem Photovoltaic Solar Cells *IEEE J. Photovol.* **8** 305-309
- [153] Celik I, Phillips A B, Song Z, Yan Y, Ellingson R J, Heben M J, Apul D 2017 Environmental analysis of perovskites and other relevant solar cell technologies in a tandem configuration *Energy Environ. Sci.* **10** 1874-1884
- [154] Zhao D, Wang C, Song Z, Yu Y, Chen C, Zhao X, Zhu K, Yan Y 2018 Four-Terminal All-Perovskite Tandem Solar Cells Achieving Power Conversion Efficiencies Exceeding 23% *ACS Energy Lett.* **3** 305-306
- [155] Li Z, Boix P P, Xing G, Fu K, Kulkarni S A, Batabyal S K, Xu W, Cao A, Sum T C, Mathews N, Wong L H 2016 Carbon nanotubes as an efficient hole collector for high voltage methylammonium lead bromide perovskite solar cells *Nanoscale* **8** 6352-6360
- [156] Jiang F, Liu T, Luo B, Tong J, Qin F, Xiong S, Li Z, Zhou Y 2016 A two-terminal perovskite/perovskite tandem solar cell *J. Mater. Chem. A* **4** 1208-1213
- [157] Heo J H, Im S H 2016 CH<sub>3</sub>NH<sub>3</sub>PbBr<sub>3</sub>–CH<sub>3</sub>NH<sub>3</sub>PbI<sub>3</sub> Perovskite–Perovskite Tandem Solar Cells with Exceeding 2.2 V Open Circuit Voltage *Adv. Mater.* **28** 5121-5125
- [158] Rajagopal A, Yang Z, Jo S B, Braly I L, Liang P-W, Hillhouse H W, Jen A K Y 2017 Highly Efficient Perovskite–Perovskite Tandem Solar Cells Reaching 80% of the Theoretical Limit in Photovoltage *Adv. Mater.* **29** 1702140
- [159] Li C, Wang Z S, Zhu H L, Zhang D, Cheng J, Lin H, Ouyang D, Choy W C H 2018 Thermionic Emission–Based Interconnecting Layer Featuring Solvent Resistance for Monolithic Tandem Solar Cells with Solution-Processed Perovskites *Adv. Energy Mater.* **8** 1801954

- [160] Dávid F, Lidón G E, Daniel P D R, Cristina M, Jérémie W, Bjoern N, Christophe B, Michele S, J. B H 2017 Efficient Monolithic Perovskite/Perovskite Tandem Solar Cells *Adv. Energy Mater.* **7** 1602121
- [161] Ávila J, Momblona C, Boix P, Sessolo M, Anaya M, Lozano G, Vandewal K, Míguez H, Bolink H J 2018 High voltage vacuum-deposited  $\text{CH}_3\text{NH}_3\text{PbI}_3\text{-CH}_3\text{NH}_3\text{PbI}_3$  tandem solar cells *Energy Environ. Sci.* **11** 3292-3297
- [162] Chen H, Ye F, Tang W, He J, Yin M, Wang Y, Xie F, Bi E, Yang X, Grätzel M, Han L 2017 A solvent- and vacuum-free route to large-area perovskite films for efficient solar modules *Nature* **550** 92
- [163] Yan J, R. L M, Longbin Q, Shenghao W, K. O L, Zhifang W, J. J P E, Yabing Q 2018 Combination of Hybrid CVD and Cation Exchange for Upscaling Cs-Substituted Mixed Cation Perovskite Solar Cells with High Efficiency and Stability *Adv. Funct. Mater.* **28** 1703835
- [164] Yang M, Li Z, Reese M O, Reid O G, Kim D H, Siol S, Klein T R, Yan Y, Berry J J, van Hest M F A M, Zhu K 2017 Perovskite ink with wide processing window for scalable high-efficiency solar cells *Nat. Energy* **2** 17038
- [165] Yang M, Kim D H, Klein T R, Li Z, Reese M O, Tremolet de Villers B J, Berry J J, van Hest M F A M, Zhu K 2018 Highly Efficient Perovskite Solar Modules by Scalable Fabrication and Interconnection Optimization *ACS Energy Lett.* **3** 322-328
- [166] Yue H, Si S, Anyi M, Yaoguang R, Huawei L, Xiong L, Hongwei H 2017 Stable Large-Area ( $10 \times 10 \text{ cm}^2$ ) Printable Mesoscopic Perovskite Module Exceeding 10% Efficiency *Solar RRL* **1** 1600019
- [167] Jaysankar M, Qiu W, van Eerden M, Aernouts T, Gehlhaar R, Debucquoy M, Paetzold U W, Poortmans J 2017 Four-Terminal Perovskite/Silicon Multijunction Solar Modules *Adv. Energy Mater.* **7** 1602807
- [168] Jaysankar M, Filipič M, Zielinski B, Schmager R, Song W, Qiu W, Paetzold U W, Aernouts T, Debucquoy M, Gehlhaar R, Poortmans J 2018 Perovskite-silicon tandem solar modules with optimised light harvesting *Energy Environ. Sci.* **11** 1489-1498
- [169] Oxford-PV Oxford PV sets world record for perovskite solar cell 2018. [Online]. Available: (<https://www.oxfordpv.com/news/oxford-pv-sets-world-record-perovskite-solar-cell>) [Accessed: January 15 2019]
- [170] Meng L, You J, Yang Y 2018 Addressing the stability issue of perovskite solar cells for commercial applications *Nat. Commun.* **9** 5265
- [171] Song Z, Abate A, Watthage S C, Liyanage G K, Phillips A B, Steiner U, Gratzel M, Heben M J 2016 Perovskite Solar Cell Stability in Humid Air: Partially Reversible Phase Transitions in the  $\text{PbI}_2\text{-CH}_3\text{NH}_3\text{I-H}_2\text{O}$  System *Adv. Energy Mater.* **6** 1600846
- [172] Matteocci F, Cinà L, Lamanna E, Cacovich S, Divitini G, Midgley P A, Ducati C, Di Carlo A 2016 Encapsulation for long-term stability enhancement of perovskite solar cells *Nano Energy* **30** 162-172
- [173] Huang J, Tan S, Lund P D, Zhou H 2017 Impact of  $\text{H}_2\text{O}$  on organic-inorganic hybrid perovskite solar cells *Energy Environ. Sci.* **10** 2284-2311
- [174] Song Z, Werner J, Watthage S C, Sahli F, Shrestha N, Wolf S D, Niesen B, Phillips A B, Ballif C, Ellingson R J, Heben M J 2017 Imaging the Spatial Evolution of Degradation in Perovskite/Si Tandem Solar Cells After Exposure to Humid Air *IEEE J. Photovol.* **7** 1563-1568
- [175] Cheacharoen R, Rolston N, Harwood D, Bush K A, Dauskardt R H, McGehee M D 2018 Design and understanding of encapsulated perovskite solar cells to withstand temperature cycling *Energy Environ. Sci.* **11** 144-150
- [176] Babayigit A, Ethirajan A, Muller M, Conings B 2016 Toxicity of organometal halide perovskite solar cells *Nat. Mater.* **15** 247-251
- [177] Celik I, Song Z, Heben M J, Apul D 2017 Life cycle analysis of metals in emerging photovoltaic (PV) technologies: A modeling approach to estimate use phase leaching *J. Cleaner Prod.* **186** 632-639
- [178] Babayigit A, Duy Thanh D, Ethirajan A, Manca J, Muller M, Boyen H-G, Conings B 2016 Assessing the toxicity of Pb- and Sn-based perovskite solar cells in model organism *Danio rerio* *Sci. Rep.* **6** 18721
- [179] Liang J, Wang C, Wang Y, Xu Z, Lu Z, Ma Y, Zhu H, Hu Y, Xiao C, Yi X, Zhu G, Lv H, Ma L, Chen T, Tie Z, Jin Z, Liu J 2016 All-Inorganic Perovskite Solar Cells *J. Am. Chem. Soc.* **138** 15829-15832
- [180] Arora N, Dar M I, Abdi-Jalebi M, Giordano F, Pellet N, Jacopin G, Friend R H, Zakeeruddin S M, Grätzel M 2016 Intrinsic and Extrinsic Stability of Formamidinium Lead Bromide Perovskite Solar Cells Yielding High Photovoltage *Nano Lett.* **16** 7155-7162
- [181] Zhou Y, Yang M, Game O S, Wu W, Kwun J, Strauss M A, Yan Y, Huang J, Zhu K, Padture N P 2016 Manipulating Crystallization of Organolead Mixed-Halide Thin Films in Antisolvent Baths for Wide-Bandgap Perovskite Solar Cells *ACS Appl. Mater. Interfaces* **8** 2232-2237
- [182] Swarnkar A, Marshall A R, Sanhira E M, Chernomordik B D, Moore D T, Christians J A, Chakrabarti T, Luther J M 2016 Quantum dot-induced phase stabilization of  $\alpha\text{-CsPbI}_3$  perovskite for high-efficiency photovoltaics *Science* **354** 92-95
- [183] Zhu W, Bao C, Li F, Zhou X, Yang J, Yu T, Zou Z 2016 An efficient planar-heterojunction solar cell based on wide-bandgap  $\text{CH}_3\text{NH}_3\text{PbI}_2.1\text{Br}_0.9$  perovskite film for tandem cell application *Chem. Commun.* **52** 304-307
- [184] Chen S, Hou Y, Chen H, Richter M, Guo F, Kahmann S, Tang X, Stubhan T, Zhang H, Li N, Gasparini N, Quiroz C O R, Khanzada L S, Matt G J, Osvet A, Brabec C J 2016 Exploring the Limiting Open-Circuit Voltage and the Voltage Loss Mechanism in Planar  $\text{CH}_3\text{NH}_3\text{PbBr}_3$  Perovskite Solar Cells *Adv. Energy Mater.* **6** 1600132
- [185] Beal R E, Slotcavage D J, Leijtens T, Bowring A R, Belisle R A, Nguyen W H, Burkhard G F, Hoke E T, McGehee M D 2016 Cesium Lead Halide Perovskites with Improved Stability for Tandem Solar Cells *J. Phys. Chem. Lett.* **7** 746-751
- [186] Yang Z, Chueh C-C, Liang P-W, Crump M, Lin F, Zhu Z, Jen A K Y 2016 Effects of formamidinium and bromide ion substitution in methylammonium lead triiodide toward high-performance perovskite solar cells *Nano Energy* **22** 328-337

- [187] Sheng R, Hörantner M T, Wang Z, Jiang Y, Zhang W, Agosti A, Huang S, Hao X, Ho-Baillie A, Green M, Snaith H J 2017 Monolithic Wide Band Gap Perovskite/Perovskite Tandem Solar Cells with Organic Recombination Layers *J. Mater. Chem. C* **121** 27256-27262
- [188] Nam J K, Chai S U, Cha W, Choi Y J, Kim W, Jung M S, Kwon J, Kim D, Park J H 2017 Potassium Incorporation for Enhanced Performance and Stability of Fully Inorganic Cesium Lead Halide Perovskite Solar Cells *Nano Lett.* **17** 2028-2033
- [189] Liang J, Zhao P, Wang C, Wang Y, Hu Y, Zhu G, Ma L, Liu J, Jin Z 2017 CsPb<sub>0.9</sub>Sn<sub>0.1</sub>Br<sub>2</sub> Based All-Inorganic Perovskite Solar Cells with Exceptional Efficiency and Stability *J. Am. Chem. Soc.* **139** 14009-14012
- [190] Forgács D, Pérez-del-Rey D, Ávila J, Momblona C, Gil-Escrig L, Dänekamp B, Sessolo M, Bolink H J 2017 Efficient wide band gap double cation – double halide perovskite solar cells *J. Mater. Chem. A* **5** 3203-3207
- [191] Yang M, Kim D H, Yu Y, Li Z, Reid O G, Song Z, Zhao D, Wang C, Li L, Meng Y, Guo T, Yan Y, Zhu K 2018 Effect of non-stoichiometric solution chemistry on improving the performance of wide-bandgap perovskite solar cells *Mater. Today Energy* **7** 232-238
- [192] Wang Z, Lin Q, Chmiel F P, Sakai N, Herz L M, Snaith H J 2017 Efficient ambient-air-stable solar cells with 2D–3D heterostructured butylammonium-caesium-formamidinium lead halide perovskites *Nat. Energy* **2** 17135
- [193] Wang Q, Zheng X, Deng Y, Zhao J, Chen Z, Huang J 2017 Stabilizing the  $\alpha$ -Phase of CsPbI<sub>3</sub> Perovskite by Sulfobetaine Zwitterions in One-Step Spin-Coating Films *Joule* **1** 371-382
- [194] Ding J, Duan J, Guo C, Tang Q 2018 Toward charge extraction in all-inorganic perovskite solar cells by interfacial engineering *J. Mater. Chem. A* **6** 21999-22004
- [195] Noel N K, Wenger B, Habisreutinger S N, Patel J B, Crothers T, Wang Z, Nicholas R J, Johnston M B, Herz L M, Snaith H J 2018 Highly Crystalline Methylammonium Lead Tribromide Perovskite Films for Efficient Photovoltaic Devices *ACS Energy Lett.* **3** 1233-1240
- [196] Nan L, Zonglong Z, Jiangwei L, K.-Y. J A, Liduo W 2018 Inorganic CsPb<sub>1-x</sub>Sn<sub>x</sub>IBr<sub>2</sub> for Efficient Wide-Bandgap Perovskite Solar Cells *Adv. Energy Mater.* **8** 1800525
- [197] Zhang J, Bai D, Jin Z, Bian H, Wang K, Sun J, Wang Q, Liu S 2018 3D–2D–0D Interface Profiling for Record Efficiency All-Inorganic CsPbBr<sub>2</sub> Perovskite Solar Cells with Superior Stability *Adv. Energy Mater.* **8** 1703246
- [198] Bian H, Bai D, Jin Z, Wang K, Liang L, Wang H, Zhang J, Wang Q, Liu S 2018 Graded Bandgap CsPbI<sub>2+x</sub>Br<sub>1-x</sub> Perovskite Solar Cells with a Stabilized Efficiency of 14.4% *Joule* **2** 1500-1510
- [199] Liu C, Li W, Zhang C, Ma Y, Fan J, Mai Y 2018 All-Inorganic CsPbI<sub>2</sub>Br Perovskite Solar Cells with High Efficiency Exceeding 13% *J. Am. Chem. Soc.* **140** 3825-3828
- [200] Khadka D B, Shirai Y, Yanagida M, Noda T, Miyano K 2018 Tailoring the Open-Circuit Voltage Deficit of Wide-Band-Gap Perovskite Solar Cells Using Alkyl Chain-Substituted Fullerene Derivatives *ACS Appl. Mater. Interfaces* **10** 22074-22082
- [201] Tsai C-M, Wu H-P, Chang S-T, Huang C-F, Wang C-H, Narra S, Yang Y-W, Wang C-L, Hung C-H, Diao E W-G 2016 Role of Tin Chloride in Tin-Rich Mixed-Halide Perovskites Applied as Mesoscopic Solar Cells with a Carbon Counter Electrode *ACS Energy Lett.* **1** 1086-1093
- [202] Liu X, Yang Z, Chueh C-C, Rajagopal A, Williams S T, Sun Y, Jen A K Y 2016 Improved efficiency and stability of Pb–Sn binary perovskite solar cells by Cs substitution *J. Mater. Chem. A* **4** 17939-17945
- [203] Lin G, Lin Y, Huang H, Cui R, Guo X, Liu B, Dong J, Guo X, Sun B 2016 Novel exciton dissociation behavior in tin-lead organohalide perovskites *Nano Energy* **27** 638-646
- [204] Zhu L, Yuh B, Schoen S, Li X, Aldighaithir M, Richardson B J, Alamer A, Yu Q 2016 Solvent-molecule-mediated manipulation of crystalline grains for efficient planar binary lead and tin triiodide perovskite solar cells *Nanoscale* **8** 7621-7630
- [205] Liu C, Fan J, Li H, Zhang C, Mai Y 2016 Highly Efficient Perovskite Solar Cells with Substantial Reduction of Lead Content *Sci. Rep.* **6** 35705
- [206] Li L, Zhang F, Hao Y, Sun Q, Li Z, Wang H, Cui Y, Zhu F 2017 High efficiency planar Sn–Pb binary perovskite solar cells: controlled growth of large grains via a one-step solution fabrication process *J. Mater. Chem. C* **5** 2360-2367
- [207] Liu C, Li W, Li H, Zhang C, Fan J, Mai Y 2017 C60 additive-assisted crystallization in CH<sub>3</sub>NH<sub>3</sub>Pb<sub>0.75</sub>Sn<sub>0.25</sub>I<sub>3</sub> perovskite solar cells with high stability and efficiency *Nanoscale* **9** 13967-13975
- [208] Zhu H L, Xiao J, Mao J, Zhang H, Zhao Y, Choy W C H 2017 Controllable Crystallization of CH<sub>3</sub>NH<sub>3</sub>Sn<sub>0.25</sub>Pb<sub>0.75</sub>I<sub>3</sub> Perovskites for Hysteresis-Free Solar Cells with Efficiency Reaching 15.2% *Adv. Funct. Mater.* **27** 1605469
- [209] Tavakoli M M, Zakeeruddin S M, Grätzel M, Fan Z 2018 Large-Grain Tin-Rich Perovskite Films for Efficient Solar Cells via Metal Alloying Technique *Adv. Mater.* **30** 1705998
- [210] Ramirez D, Schütt K, Wang Z, Pearson A J, Ruggeri E, Snaith H J, Stranks S D, Jaramillo F 2018 Layered Mixed Tin–Lead Hybrid Perovskite Solar Cells with High Stability *ACS Energy Lett.* **3** 2246-2251
- [211] Liu M, Chen Z, Xue Q, Cheung S H, So S K, Yip H-L, Cao Y 2018 High performance low-bandgap perovskite solar cells based on a high-quality mixed Sn–Pb perovskite film prepared by vacuum-assisted thermal annealing *J. Mater. Chem. A* **6** 16347-16354
- [212] Lee S, Ha T-J, Kang D-W 2018 Mixed-halide Pb–Sn binary perovskite films with various Sn-content for Pb-reduced solar cells *Materials Letters* **227** 311-314
- [213] Wang Y, Fu W, Yan J, Chen J, Yang W, Chen H 2018 Low-bandgap mixed tin–lead iodide perovskite with large grains for high performance solar cells *J. Mater. Chem. A* **6** 13090-13095
- [214] Lian X, Chen J, Zhang Y, Qin M, Li J, Tian S, Yang W, Lu X, Wu G, Chen H 2019 Highly Efficient Sn/Pb Binary Perovskite Solar Cell via Precursor Engineering: A Two-Step Fabrication Process *Adv. Funct. Mater.* **29** 1807024



1  
2  
3  
4  
5  
6  
7  
8  
9  
10  
11  
12  
13  
14  
15  
16  
17  
18  
19  
20  
21  
22  
23  
24  
25  
26  
27  
28  
29  
30  
31  
32  
33  
34  
35  
36  
37  
38  
39  
40  
41  
42  
43  
44  
45  
46  
47  
48  
49  
50  
51  
52  
53  
54  
55  
56  
57  
58  
59  
60

Accepted Manuscript